Investigating Multi-Directional Inhomogeneous Granular Suspensions

David de Klerk

October 18, 2019
v1.1

Investigating Multi-Directional Inhomogeneous Granular Suspensions

David de Klerk

Department of Physics
University of Cape Town

Supervisors
Indresan Govender
and
Aubrey Mainza

October 18, 2019
v1.1

David de Klerk
Investigating Multi-Directional Inhomogeneous Granular Suspensions
Supervisors: Indresan Govender and Aubrey Mainza
October 18, 2019

University of Cape Town
Department of Physics
Rondebosch
Cape Town
7700

Declaration

I hereby declare that the work on which this thesis is based is my original work (except where acknowledgements indicate otherwise) and that neither the whole work nor any part of it has been, is being, or is to be submitted for another degree in this or any other university. I authorise the University to reproduce for the purpose of research either the whole or any portion of the contents in any manner whatsoever.

Signed by candidate

David de Klerk
October 18, 2019

Abstract

Granular flows in rotating drums find many applications in industry, even though the dynamics of their granular media is not fully understood. Several models of granular flow and granular suspensions (where a viscous fluid is present in the voids between the granular particles) have been proposed in the last decade and a half. These models are unified in the way that dimensional analysis is employed to describe bulk properties of the flow in terms of a number of dimensionless parameters. However, applicability to rotating drums has not been demonstrated for many of these models. Furthermore, most studies rely on numerical simulations or experiments of slowly rotating drums that are not easily identified with industrial applications that operate in higher Froude regimes.

This thesis presents a series of Positron Emission Particle Tracking (PEPT) experiments and Discrete Element Method (DEM) simulations of rotating drums with a viscous fluid. The three aims of the thesis are, to investigate the use of the Ergodic hypothesis when analysing PEPT data, to test the use of the lubrication approximation in the DEM simulations and to compare results from rotating drums to the latest models of granular rheology and granular suspensions.

Two sets of PEPT experiments were carried out with a drum (radius $R = 230\,\mathrm{mm}$ and length $L = 200\,\mathrm{mm}$) which was forced to rotate around its axis. The first series of experiments, used to investigate the use of the ergodic hypothesis, used a fixed rotation rate ($\omega = 0.6\omega_c = 0.6\sqrt{g/R}$) and three different particle sizes ($5\,\mathrm{mm}$, $8\,\mathrm{mm}$ and $10\,\mathrm{mm}$). A radio labelled tracer particle's location was recorded for $10\,\mathrm{h}$ for each of the three particle sizes. The second series of experiments, intended to test rheology models of dense suspensions and the use of the lubrication approximation in DEM, used $10\,\mathrm{mm}$ diameter glass spheres and glycerol/water mixtures in a drum.

The second configuration was simulated with DEM using the Hertz-Mindlen contact model for particle-particle interactions. The effect of a viscous force between particles in close proximity to each other was captured by a lubrication approximation. Particle level data from experiments and simulations are transformed to smooth fields by a coarsegraining method which is described in detail.

The ergodic assumption (which states that time averages of the PEPT tracer is equivalent to the ensemble average and central to analysing PEPT data) is evaluated using the first series of experiments. It was found that the average velocity can be established after $15\,\mathrm{min}$ tracking time, however the solids fraction still shows under sampled regions after tracking for $3\,\mathrm{h}$. Several techniques were used to investigate this, including as Poincaré maps and the global mixing index. A variation on the averaging technique is shown to account for under sampled regions in the solids fraction.

The rheology in the experimental rotating drums used in this study remain at high Stokes number ($S_t > 1$), even at high fluid viscosity ($\eta_f = 0.25 \pm 0.04\,\mathrm{Pa\,s}$). Further, comparisons between PEPT and DEM results showed good agreement when $S_t > 10$. DEM results were compared to the visco-plastic rheology of Da Cruz et. al., the dense suspension rheology of Trulsson et. al., the extensions to kinetic theory made by Chialvo and Sundaresan and the non-local granular fluidity of Zhang and Kamrin. Good agreement was observed for the visco plastic, dense suspension and kinetic theory model for $S_t > 10$. However, the lubrication approximation did not reproduce the models accurately for $S_t < 10$, when other viscous forces start to become dominant. Due to compounding uncertainties the non-local granular fluidity model only showed qualitative agreement with DEM results.

Acknowledgements

I would like to thank my supervisors, Professors Indresan Govender and Aubrey Mainza, their professional guidance and advice left a definitive impact on this thesis and my work in general.
The Department of Physics provided me with a quiet and stimulating place to work despite protests, loadshedding and a water crisis.
I am grateful for generous financial support from the Centre of Minerals Research and would also like to thank the following members of the Comminution Group – Dr Max Richter, Dr Sherry Bremner, Dr Olumide Ogunmodimu, Dylan Blakemore, Conrad Ndimande and Tope Oladele – for our regular meetings and discussions around various topics related to this thesis.
Experimental work was performed at the PEPT Cape Town facility at iThemba Labs. Mike van Heerden prepared the PEPT tracer particles and was always available and willing to help. Also, Dr Katy Cole and Dr Tom Leadbeater lent their expertise on various aspects of analysing and interpreting PEPT data.
I am grateful for the Institute of Infrastructure and Environment, University of Edinburgh, in particular Dr Jin Sun, Dr Chris Ness and Tim Najuch, for hosting me for a three month visit. Without their support with LIGGGHTS, discussions on granular rheology, and allowing me to use their implementation of the lubrication approximation, this work would not have been possible.
I also enjoyed a fruitful collaboration with Dr Thomas Pähtz, who discussed many points on rheology and pointed out a few mistakes in my coarsegraining code.
Computations were performed using facilities provided by the University of Cape Town's ICTS High-Performance Computing team (http://hpc.uct.ac.za).
I would also like to thank my wife Talitha, parents Christo and Miems, siblings Fransu, Monica and Willem, and in-laws Herman and Bets. Without their love, support and encouragement I would not have been able to see this through.

Contents

List of Acronyms

CD Contact Dynamics 20

CFD Computational Fluid Dynamics 2, 20–22, 25, 82, 90

CoC Center of Circulation . . . . . xviii, 19, 65–67, 69, 71–77, 94

DEM Discrete Element Method xvi, xix, xx, 2, 3, 5, 20–23, 25, 26, 30, 31, 33, 35, 38, 44, 45, 47, 49, 51, 56, 61–63, 79–83, 85, 88–90, 93, 94

KT Kinetic Theory 1, 13–15, 94

LOR Line of Response . . . . . xv, xvii, 17, 51–56, 64

MD Molecular Dynamics 20

MRI Magnetic Resonance Imaging 16

PDE Partial Differential Equation 21

PEPT Positron Emission Particle Tracking xv, xvii–xix, 2, 3, 5, 16–19, 22, 23, 35, 44–47, 49, 50, 53, 57, 60–65, 67–69, 71, 72, 74, 75, 79–83, 89, 93, 94

PET Positron Emission Tomography . . xvii, xviii, 2, 16, 17, 49, 50, 52, 53, 56, 67

PIV Particle Image Velocimetry 16

RPT Radioactive Particle Tracking 19

SPH Smooth Particle Hydrodynamics 2, 21, 22, 82, 90

SPT Single Particle Tracking 63

List of Figures

List of Tables

1 Introduction

Dry granular media exhibit different flow patterns that are comparable to gas, fluid and solid phases states (see Jaeger et al. [1] and references there in). The solid-like phase is a quasi-static regime where particle inertia is negligible. The gas-like state is characterised by binary collisions between grains. In between these two regimes exist a fluid like flow where particle inertia is important but a contact network between grains are maintained.

Models for describing the solid and gas behaviour have been available, however, advances in the understanding of dense granular flows associated with the liquid regime, have only been made more recently. In particular, GDR MiDi [2] showed that the solids fraction can be written as a one-to-one function of a dimensionless quantity, the inertial number. Further, they showed that this can be done independent of the configuration or geometry of the flow. This is accomplished by defining the inertial number, I, in terms of the shear rate and local pressure, quantities that have no dependence on long range effects. Da Cruz et al. [3] and Jop et al. [4] showed that the ratio of shear-to-compression forces, or effective friction, can also be described by a one-to-one function of the inertial number. This model is often referred to as the $\mu(I)$-rheology.

The ideas of dense granular flows were extended to dense suspensions by Boyer et al. [5] and Trulsson et al. [6]. The difference between dense suspensions and dense granular flows is that the latter ignores the effect of a fluid between the solid particles, while the former incorporates the fluid viscosity into a new dimensionless quantity called the viscous number (J). In these systems the Stokes number (S_t) distinguishes between fluid dominated flows ($S_t \ll 1$) and particle dominated flows ($S_t \gg 1$) (Courrech du Pont et al. [7]). Boyer et al. [5] showed that the effective friction can be written as a function of the viscous number for fluid dominated flows. Trulsson et al. [6] proposed a model that combines the viscous and inertial models by writing the effective friction as a function of a linear combination of I and J.

Models for the gaseous phase of granular flow have been developed in analogy to the Kinetic Theory (KT) for gasses (Lun et al. [8], Jenkins and Savage [9], Jenkins and Richman [10], and Garzó and Dufty [11]). These ideas have been extended to the fluid regime by Chialvo and Sundaresan [12] and the solid like regime by Kamrin and Koval [13], Henann and Kamrin [14], Zhang and Kamrin [15], and Bouzid et al. [16, 17].

Solid, fluid and gaseous regimes appear in the context of rotating drums where it is possible for all three phases to be present at the same time. The three phases are often separated by features described in the literature as follows: a cascading "flowing layer" exists above a "rising en mass" region between the drum and the

equilibrium surface separating the two (Powell and McBride [18], Morrison et al. [19], and Govender and Pathmathas [20]). The flowing layer is bounded by an upper S-shaped surface termed the free surface (Govender and Pathmathas [20], Rajchenbach [21], Zik et al. [22], Orpe and Khakhar [23], and Taberlet et al. [24]) or bulk free surface according to (Morrison et al. [19]). A cataracting region can be present above the free surface, depending on the drum's rate of rotation. The rising en mass region is often identified with the solid like phase, the flowing layer with the fluid like phase and cataracting material with gaseous phase.

Models of granular flow (especially the $\mu(I)$-rheology) have been studied in the context of rotating drums using experiments (GDR MiDi [2], Orpe and Khakhar [23], Chou and Lee [25], Pignatel et al. [26], and Govender et al. [27]) and simulations (Cortet et al. [28]).

Positron Emission Particle Tracking (PEPT) (Hawkesworth et al. [29], Bemrose et al. [30], and Parker et al. [31]) is a valuable experimental method for measuring flow properties of particulate systems, and has been used to verify rheological models and numerical simulations [27]. PEPT records the position of a radio labelled tracer using a Positron Emission Tomography (PET) scanner, and uses the ergodic assumption (Wildmann et al. [32]) to transform the particle's position-time data to continuum values that are representative of the ensemble. As is the case with many other experimental methods, only kinematic quantities, such as the average velocity and shear rate can be determined using PEPT. Lacking the ability to record inter-particle forces, the experimenter is restricted to testing the rheology indirectly via the scaling laws that they predict (Govender et al. [27] and Jop et al. [33]) or by focusing on slowly rotating drums (Orpe and Khakhar [23], Chou and Lee [25], and Pignatel et al. [26]).

Simulations provides a rich data set, affording the ability to record every physical quantity that is related to each particle as well as the interactions between them. It is possible to test rheological models directly against the data provided by simulations. Discrete Element Method (DEM) (Cundall and Strack [34]) has become an established method to study dry granular flows numerically. Particle interactions are simulated using a spring-dashpot model where repulsive forces are calculated as a function of the overlap between particles. Several approaches have been used to incorporate viscous effects with DEM. These methods couple simulations between DEM and other software packages that simulate the fluid explicitly using Computational Fluid Dynamics (CFD) (Sun and Xiao [35], Malahe [36], Xiao and Sun [37], Kloss et al. [38], and Hu et al. [39]) or Smooth Particle Hydrodynamics (SPH) (Cleary et al. [40, 41]). Another approach has been to include lubrication and drag forces directly in the DEM software without simulating the fluid effects explicitly (Trulsson et al. [6], Cox [42], Kim and Karrila [43], Ball and Melrose [44], Seto et al. [45], and Ness and Sun [46, 47]).

There are three open questions pertaining to granular suspensions in rotating drums that are addressed in this thesis:

- How effective is the ergodic hypothesis when analysing PEPT data?
- To what extent can the lubrication approximation be used to simulate dense suspensions in rotating drums?
- How can the developments in rheology models be applied to rotating drums?

The ergodic hypothesis is needed for coarsegraining PEPT data and states that, for a sufficiently long time interval, the time average of a single representative particle is equal to the ensemble average. Wildmann et al. [32] tested the hypothesis by dividing the flow volume into slices. Each slice was further divided into 3×3 segments and the average and standard variation of the solids fraction in the 9 segments compared. The division of spatial regions is not appropriate for rotating drums, because of large spatial variations in solids fraction. Instead, this study will perform PEPT experiments over $10\,\mathrm{h}$ periods and test the ergodic hypothesis by dividing the results in shorter time intervals and averaging over these intervals. Other techniques from the mixing literature can also be used to investigate whether the dynamics of the particles can drive the tracer away from certain regions of the mill.

The lubrication approximation has been used by Trulsson et al. [6], Seto et al. [45], and Ness and Sun [46] to study dense granular suspensions. These studies focused on the role of the viscous and inertial number on describing the solids fraction and effective friction. Trulsson et al. [6] and Seto et al. [45] used the lubrication approximation in conjunction with drag and Archimedes forces, however their effect was not noticeable for high solids fraction ($\phi > 0.45$) and consequently, Ness and Sun [46] ignored these forces in their simulations. This methodology of simulating dense suspensions has not been used, or tested against experimental data, in the context of rotating drums. It is not known which conditions prevail in rotating drums and when the lubrication approximation can be successfully used. In this work, simulations in the LIGGGHTS DEM package was performed and detailed comparisons between PEPT results made to test the use of the lubrication approximation in rotating drums.

Dense granular rheology in multi directional flows has received some attention in literature, however the latest models of dense suspensions (Boyer et al. [5] and Trulsson et al. [6]), kinetic theory (Chialvo and Sundaresan [12]) and non-local granular fluidity (Kamrin and Koval [13], Henann and Kamrin [14], and Zhang and Kamrin [15]) have not been investigated in this environment. Results from DEM simulations are compared against these models, with particular focus on the scaling relationships between dimensionless quantities.

The rest of the thesis is outlined as follows: Chapter 2 reviews the literature relevant to the following chapters. Chapter 3 discusses the numerical studies carried out, in particular the lubrication approximation used to simulate the viscous effects on granular flows in a DEM simulation. Chapter 4 discusses the coarsegraining method used to constitute the continuum fields used in the rheological models.

Chapter 5 presents the experimental PEPT work carried out to compliment and validate the computer simulations. Glass beads are used as the granular material and a water/glycerol mixture for the fluid. The ratio of water-to-glycerol was altered to provide fluids of different viscosities. Chapter 6 discusses the consequences of the experimental techniques and investigates the validity of the ergodic hypothesis that is used to coarsegrain data from experiments. Chapter 7 makes comparisons between simulations and experiments and compares the simulation results against several models of granular rheology. Chapter 8 discusses future work and presents final conclusions.

Literature Review

2

Granular media in rotating drums display complex flow phenomena that require sophisticated tools to analyse the system. Indeed, many such tools for investigating rotating drums and other configurations have been discussed in the literature, however this chapter will focus on methods from granular rheology and dense suspensions that are directly applicable to rotating drums. In addition, many experimental and numerical techniques have been used to investigate granular flows, however in this thesis Positron Emission Particle Tracking (PEPT) and Discrete Element Method (DEM) will be used as the main experimental and numerical methods, respectively. The literature review will discuss previous works that are most relevant to the use and application of rheology of dense granular flows, dense suspensions, PEPT and DEM in this thesis.

2.1 Coarsegraining

The granular flow models described here deal with quantities averaged over a spatial region that is of the same order as the particle diameter. Several methods have been proposed to transform the discrete particle level quantities to continuum fields.

Arguments have been made against a meso-scale continuum description of granular flows. Particles have the ability to transmit contact forces over distances that are much larger than the particle size – much like a Newton cradle where forces can be transmitted through particles without changing their momentum. This phenomena is know as force chains. Granular continuum descriptions in both the static and flowing phases have been criticised by Majmudar and Behringer [48] and Geng et al. [49] because of the presence of force chains that transmit contact forces over many particle diameters. However, these studies were done using two dimensional disks and Rycroft et al. [50] found that force chains are much shorter in three dimensional flows. Their interpretation of the phenomena was that spheres in 3D allow for more contacts per particle than disks in 2D and therefore decreases the chances of two contacts transmitting forces over the width of a particle. Further evidence for a continuum description of granular flows was that there seems to be a high correlation between the directions of the eigenvectors of the deformation rate tensor and the Cauchy stress tensor. Studies in 2D by Goldenberg and Goldhirsch [51] have shown that an inter-particle friction may further help to smooth the effect of force chains.

The continuum description needs to be independent of the averaging size. Glasser and Goldhirsch [52] found that fluctuations in the velocity are dependent on the averaging size when using the averaging scheme introduced by Babic [53]. Artoni and Richard [54] suggested an alternative definition of how fluctuations can be

calculated that produces a kinetic stress that is independent of the averaging size. Several studies have been performed to identify the optimal averaging size (cf. Rycroft et al. [50]). Rycroft et al. [50] found that a spatial volume between $3d$ and $5d$ (where d is the particle diameter) is sufficient to produce good agreement with the results from Da Cruz et al. [3]. Babic [53] also has a time average and as pointed out by Artoni and Richard [54] that the averaging volume is now a space time volume which allows for the spatial extent to be made smaller than the particle size, as long as the time average is carried out over a sufficiently long duration so that enough statistics can be recorded.

In this thesis the method proposed by Glasser and Goldhirsch [52], Babic [53], and Artoni and Richard [54] is used and the details of how coarsegraining is carried out is the subject of Chapter 4. For the discussion that follows it is sufficient to point out that the following fields are reconstructed. The volume fraction $\phi(\vec{r})$ is the ratio of the volume occupied by particles to the total volume in a region. The velocity $\vec{v}(\vec{r}) = \langle v_x(\vec{r}), v_y(\vec{r}), v_z(\vec{r})\rangle$ is defined so that it resembles the average velocity of particles within a distance $w \sim d$ around a point $\vec{r} = \langle x, y, z\rangle$. The deformation rate tensor, related to the average velocity, is $D_{ij} = \frac{1}{2}\left(\partial_i v_j(\vec{r}) + \partial_j v_j(\vec{r})\right)$, where indices i and j run over the spatial directions x, y and z. The stress tensor is composed of two parts $\sigma_{ij} = \sigma^c_{ij} + \sigma^k_{ij}$, the first σ^c is due to contacts between particles named the contact stress, and the second σ^k due to the vibration of particles, or variation in the particle velocity from, the mean and called the kinetic stress.

A 3×3 matrix can be written as the sum of its trace, symmetric part and anti-symmetric parts, as follows:

$$A_{ij} = -\frac{1}{3}A_{kk}\delta_{ij} + \left(A_{ij} + \frac{1}{3}A_{kk}\delta_{ij}\right) \ , \tag{2.1}$$

where Einstein notation is used, thus a summation over repeated indices is implied, or $A_{kk} = \sum_k A_{kk}$. For the rate of deformation tensor, the first term is related to the compressibility of the medium. The second term is the deviatoric part of the strain rate and denoted by $\gamma^d_{ij} = D_{ij} + D_{kk}\delta_{ij}$. The shear rate is the norm $\dot{\gamma} = |\gamma^d_{ij}|$.

For the stress tensor, the first term is identified as the pressure $P = -\frac{1}{3}\sigma_{kk}$. The norm of the second term is the shear stress $\tau_{ij} = \sigma_{ij} + P\delta_{ij}$.

2.2 Dimensional Analysis and Flow Regimes

The bulk behaviour of granular material can be identified as a solid, fluid, gas or a mixture of these states (Jaeger et al. [1]). These ideas have been further developed for flows in rotating drums that exhibit slipping, surging, rolling, cascading and centrifuging, (see Figure 2.1). Henein et al. [55] and Mellmann [56] classified rotating drum flows by their Froude number,

$$F_r = \frac{\omega^2 R}{g} \ , \tag{2.2}$$

where ω is the angular velocity of the drum, R its radius and g is gravitational acceleration.

Buckingham's Pi theorem (Barenblatt [57]) is a formal statement about the possible number of independent dimensionless parameters that can be constructed from a given set of dimensionful quantities. A dimensional matrix $\mathcal{M}$ is constructed where the columns make up the dimensions. For the case of Froude number in rotating drums the dimensions are length L, time T and mass M. The rows are made of the dimensionful parameters relevant to the problem which are the radius R, rate of rotation ω and gravitational acceleration g.

$$\mathcal{M} = \begin{array}{c} \\ L \\ T \end{array} \begin{array}{c} \begin{array}{ccc} R & \omega & g \end{array} \\ \begin{bmatrix} 1 & 0 & 1 \\ 0 & -1 & -2 \end{bmatrix} \end{array} . \tag{2.3}$$

Formally Buckingham's Pi theorem states that the number of dimensionless parameters p that can be constructed is the nullity of the dimensional matrix $\mathcal{M}$, the number of dimensions in the problem, k, is the rank of $\mathcal{M}$ and the number of dimensionful parameters is n. It follows from the rank-nullity theorem that $k = n - p$. For a system that can be described by a function f with n quantities q_i, measured in k independent units,

$$q_1 = f(q_2, \ldots, q_n) \, , \tag{2.4}$$

can be expressed by a new function F of $p = n - k$ independent dimensionless variables π_i,

$$\pi_1 = F(\pi_2, \ldots, \pi_p) \, . \tag{2.5}$$

The p dimensionless quantities, or π-groups, is of the form,

$$\pi_i = \prod_{j=1}^{n} q_j^{a_j} \, , \tag{2.6}$$

with the exponents a_j rational numbers. It should be noted that the choice of π-groups are not unique for a given problem. Different choices of π groups might reveal relationships in data that produce better models than others and therefore experimental tests are required to select the most appropriate dimensionless parameters. It is also possible that only one π-group exists, as is the case for the Froude number.

The classification of rotating drums by Froude number suffers from two drawbacks. Firstly, different flow regimes are often observed at the same Froude number. For instance, the cascading regime exhibits a fluid like flowing layer over a solid like rising region (Orpe and Khakhar [23]). Secondly, these classifications are configuration specific and do not transfer well to other systems even when they share similar flow properties (Taberlet et al. [24]).

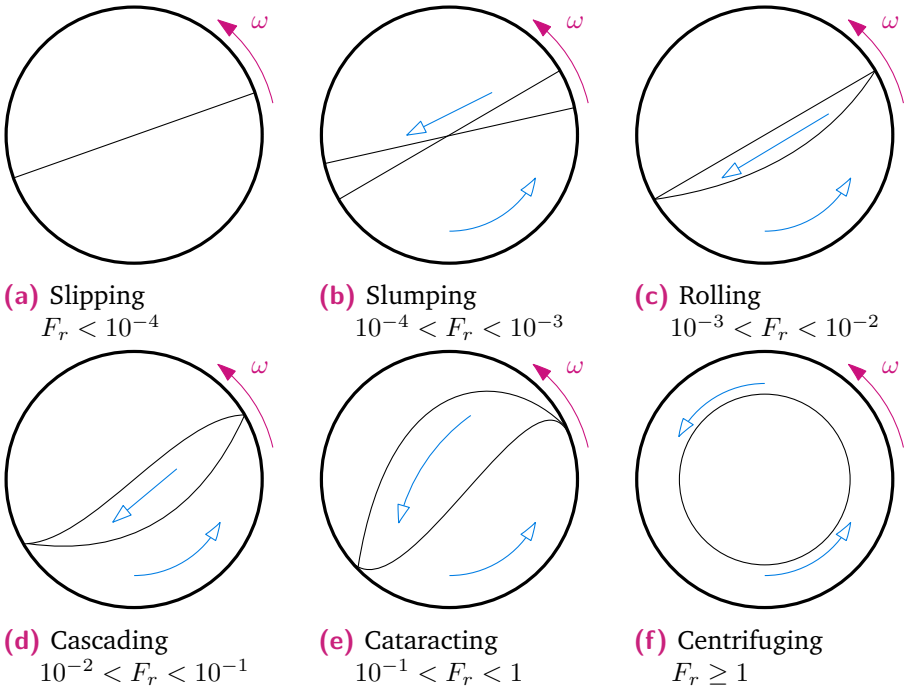

Figure 2.1 – The flow regimes, identified by Henein et al. [55] and Mellmann [56], in rotating drums classified by Froude number.

A more productive approach to understanding granular flows in general has been to investigate the possible dimensionless quantities that can be constructed from the dimensionful parameters at the meso scale. The resulting models are independent of the device or geometry that the material is confined to. Table 2.1 shows a selection of parameters and their dimensions that are relevant to granular flows in rotating drums. Each quantity's unit can be expressed in terms of the units of length, L, time, T and mass, M. There is only one additional dimension introduced (namely mass, M), as compared to the Froude number, and therefore the number of dimensionless quantities needed to describe the flow has to increase as additional dimensionful quantities are used in further models.

In the rest of this section, a subsection is dedicated to each of the models that are relevant to the description of the flow of granular suspensions.

2.2.1 Bagnold

Bagnold [58, 59] performed experiments in liquid suspensions sheared in a concentric cylinder rheometer and found that at low volume fractions the shear stress was directly proportional to the shear rate ($\tau \propto \dot{\gamma}$), but at high concentrations the stress was proportional to the square of the shear rate. The following relationship was proposed,

$$\tau = \rho_p d^2 f(\phi) \dot{\gamma}^2 \,, \tag{2.7}$$

where ρ_p is the particle density, d the particle diameter and $f(\phi)$ a dimensionless function depending on the solids fraction only. This relation can be understood from

Table 2.1 – Dimensionful variables that are used in the various meso scale models discussed in this section along with their units expressed in the basic dimensions of length L, time T, and mass M.

	Symbol	Description	Units
Rotating Drum	ω	Rotational speed	T^{-1}
	R	Radius	D
	g	Gravitational acceleration	DT^{-2}
Micro	d	Particle diameter	D
	ρ_P	Particle Density	MD^{-3}
Macro	ρ	Density	MD^{-3}
	v	Velocity	MT^{-1}
	$\dot{\gamma}$	Shear rate	T^{-1}
	P	Pressure	$D^{-1}MT^{-2}$
	τ	Shear Stress	$D^{-1}MT^{-2}$
Fluid	η_f	Fluid viscosity	$D^{-1}MT^{-1}$
	ρ_f	Fluid density	MD^{-3}

dimensional analysis because for a collision dominated shear flow, where particles only interact through instantaneous pairwise collisions and, in the absence of an interstitial fluid, the only quantities with dimensions of time are the shear rate and the shear stress. In particular the only time scale is the inertial time $t_i = 1/\dot{\gamma}$. The only relevant dimensionful micro quantities are particle properties d and ρ_p and equation (2.7) is the only way to relate these quantities [60].

A careful re-examination of Bagnold's original experiments by Hunt et al. [61] found that the nonlinear relationship could have been due to the small height of the cylinders relative to the gap between them. This relationship has also been difficult to generalise to a full tensorial formulation [62].

2.2.2 Local Viscoplastic

GDR MiDi [2] proposed the inertial number as a dimensionless parameter to classify granular flows, where the interstitial fluid's viscosity is small enough not to effect the flow. The inertial number,

$$I = \frac{\dot{\gamma} d}{\sqrt{P/\rho_p}}\,, \tag{2.8}$$

is the ratio of two microscopic time scales. The first is the inertial timescale that was present in the Bagnold model $t_i = 1/\dot{\gamma}$ and is associated to the time it takes for adjacent layers of grains to move across each other. The second $t_s = d/\sqrt{P/\rho}$ is due to the pressure, that is now considered as an additional parameter, and is related to the time it takes for a particle to move in and out of a gap.

Unlike the Froude number, the parameters that constitute the inertial number are properties of the flow and therefore it is not specific to any particular geometry or configuration. Indeed, GDR MiDi [2] showed that the solids fraction ϕ can written

as a function of I for plane shear, annular shear flow, vertical chute flow, flow on an inclined plane and surface flows of heaps and rotating drums.

For rigid spheres moving down an inclined plane, the effective friction $\mu = |\tau|/P$ (the ratio of shear stress τ to pressure P) was identified as another dimensionless parameter by Da Cruz et al. [3], who showed that it collapses onto a line when it is written as a function of the inertial number $\mu(I)$. Pouliquen [63] and Jop et al. [33] showed that the effective friction and solids fraction collapse onto a line when they are plotted as a function of the inertial number. The dimensionless system is

$$\tau = \mu(I)P \quad \text{and} \quad I = \frac{\dot{\gamma}d}{\sqrt{P/\rho_p}} , \tag{2.9}$$

where the form of the effective friction is

$$\phi(I) = \phi_c - aI , \quad \text{with} \quad \mu(I) = \mu_s + \frac{\mu_2 - \mu_s}{I_0/I + 1} . \tag{2.10}$$

The parameter μ_s is related to the friction coefficient at which a static collection of particles starts to flow, and μ_2 is the asymptotic maximum effective friction. The inertial number has shown to parametrise the fluid like phase of granular material. As $I \to 0$ the material tends to behave like a solid, while $I \sim 1$ is associated with a dense flowing regime. In the solid limit, the solids fraction approaches random close packing $\phi_c \approx 0.6$. The parameter I_0 is material specific and determines the inertial number at which the effective friction is the average of the two limits $\mu(I = I_0) = 1/2(\mu_s + \mu_2)$.

The relation from Bagnold, or the so called volume controlled picture, which is described by a set of equations

$$\tau = \rho_P d^2 f_1(\phi)\dot{\gamma}^2 \quad \text{and} \quad P = \rho_P d^2 f_2(\phi)\dot{\gamma}^2 , \tag{2.11}$$

can be consolidated with the formulation of the inertial number (2.10) when the functions f_1 and f_2 are chosen as:

$$f_1(\phi) = \mu[I(\phi)] \quad \text{and} \quad f_2(\phi) = \frac{1}{I^2(\phi)} . \tag{2.12}$$

where the function $I(\phi)$ is the inverse of $\phi(I)$ (Forterre and Pouliquen [64] and Andreotti et al. [65]). However, f_1 and f_2 diverge when the solids fraction approaches the critical volume fraction ϕ_c; the limit $\phi \to \phi_c$ and $I \to 0$ is associated with the liquid to solid transition in granular flows. Even though the two descriptions of granular flows are equivalent and the ratio $\mu = \tau/P$ remains finite near the liquid to solid transition (as $I \to 0$), the volume controlled picture presents difficulty to experimental validation, because f_1 and f_2 becomes difficult to measure.

A tensorial stress-strain relationship was proposed by Jop et al. [4]:

$$\tau_{ij} = \mu(I)\frac{P}{|\dot{\gamma}^d|}\dot{\gamma}^d_{ij} \,, \tag{2.13}$$

where $\tau_{ij} = \sigma_{ij} + P\delta_{ij}$ is the deviatoric part (or second invariant) of the stress tensor, $\dot{\gamma}_{ij} = \frac{1}{2}(\partial_i v_j + \partial_j v_i)$ the strain rate, $\dot{\gamma}^d_{ij} = \dot{\gamma}_{ij} - \frac{1}{d}\sum_{k=1}^{d}\dot{\gamma}_{kk}\delta_{ij}$ its second invariant and $d = \{2, 3\}$ the number of dimensions of the system. This rheology relates two symmetric tensors with zero trace and therefore both are fully characterised by their norm and principle directions. The relationship in (2.13) imposes two conditions on the flow: by the taking the norm on both sides the scaling relation $\mu(I) = |\tau|/P$ is recovered and, secondly, that τ_{ij} and $\dot{\gamma}^d_{ij}$ have the same principle directions.

For flows confined to one direction, such as the pure sheer or inclined plane configurations, the second condition is imposed by the geometry of the flow. However, Cortet et al. [28] found that, in rotating drums, the scalar $\mu(I)$ relation holds, but the second condition is not met. Rycroft et al. [50] and Lacaze and Kerswell [66] also found a misalignment in the principle directions of τ_{ij} and $\dot{\gamma}^d_{ij}$ for a granular collapse of a vertical cylinder onto a flat surface.

Experimental studies of rotating drums have been carried out by GDR MiDi [2], Orpe and Khakhar [23], Chou and Lee [25], Pignatel et al. [26], and Govender et al. [27]. The rotating drum does not allow the pressure to be controlled by the experimenter and it is difficult to measure the forces between particles. To make comparisons between experimental data and rheological models, a force balance is carried out on a volume element in the flowing layer. A zero resultant force is assumed on a volume element that is moving parallel to the free surface.

Two approaches have been used to ensure that these conditions are met. The angular velocity of the drum can be constrained to remain in the rolling regime, as in Chou and Lee [25] and Pignatel et al. [26], and the angle of repose, θ, can be identified with the angle between the free surface and the horizontal.

Alternatively, at higher Froude number the analysis is carried out on the center line; the line that connects the center of the drum to the point where the velocity is zero (GDR MiDi [2] and Chou and Lee [25]). The center line also corresponds to the thickest part of the flow. The angle of repose is defined as the angle between the free surface and horizontal at the point where the free surface intercepts the center line. A scaling law is derived from a force balance that results in the relation

$$\mu(I) = \tan\theta = \mu_s + \frac{\mu_2 - \mu_s}{I_0/I + 1} \,. \tag{2.14}$$

The experimental approach does not capture what happens in the rising region and assumes that the flowing layer is homogeneous. Further, the assumption that a volume element has no net force cannot be true near the shoulder and toe regions, because the flow is not linear. A centripetal force is required to turn the material.

2.2.3 Dense Suspensions

Dimensional arguments have been extended to dense granular suspensions. Courrech du Pont et al. [7] identified three flow regimes that can be classified by the particle to fluid density ratio $r = \rho_p/\rho_f$ and the Stokes number,

$$S_t = \frac{\rho_p d^2 \dot{\gamma}}{\eta_f} \,, \tag{2.15}$$

where η_f is the fluid viscosity. They describe dry granular flows when $r \gg 1$, $S_t > 1$ and the fluid has no effect. The Stokes number parametrises the relative importance of grain inertia to viscous effects. In the limit where $S_t \ll 1$ viscous effects dominate particle behaviour, but when $S_t \gg 1$ the grains have enough inertia for viscous effects to have a negligible effect. The transition between the two regimes happens at a critical Reynolds number $R_e = S_t/r \approx 2.5$.

Cassar et al. [67] argued that the presence of a fluid with viscosity η_f introduces a new quantity with units of time and therefore another microscopic time scale should be possible. They showed that the dense visco-plastic model still holds when substituting the inertial time scale for a viscous time scale for submersed granular flow down an inclined plane. Instead of the inertial number, they used a viscous number defined as

$$J = \frac{\eta_f \dot{\gamma}}{P} \,. \tag{2.16}$$

Amarsid et al. [68] re-frames the time scales in terms of the static, viscous and inertial time, $t_s = d(\rho_p/P)^{1/2}$, $t_v = d(\rho_p/\eta_f\dot{\gamma})^{1/2}$, and $t_i = \dot{\gamma}^{-1}$, respectively. Two independent parameters can be constructed from the three timescales and the inertial number, $I = t_s/t_i$, and viscous number, $J = t_s/t_v$, have received a lot of attention. The Stokes number can be written as the ratio $S_t = I^2/J$. Boyer et al. [5] showed that the solids fraction and effective friction collapse when plotted against the viscous number for $S_t \ll 10$. They proposed a model similar to the $\mu(I)$ rheology for granular flows:

$$\phi(J) = \frac{\phi_c}{1 + \sqrt{J}} \quad \text{and} \quad \mu(J) = \mu_1 + \frac{\mu_2 - \mu_1}{1 + I_0/J} + J + \frac{5}{2}\phi_m\sqrt{J} \,. \tag{2.17}$$

The first term recovers the contribution due to contact stresses while the second term recovers the Einstein viscosity for low solids fraction. They also showed that their model can be viewed in terms of the effective viscosity (Stickel and Powell [69]), which is described by

$$\tau = \eta_s(\phi)\eta_f\dot{\gamma} \quad \text{and} \quad P = \eta_n(\phi)\eta_f\dot{\gamma} \,. \tag{2.18}$$

Here, η_s and η_n are the effective shear and normal viscosities, respectively. The effective viscosity formulation is similar to the constant volume picture in granular

flows and similarly this formulation can be described in terms of $\phi(J)$ and $\mu(J)$ by choosing

$$\eta_s = \frac{\mu[J(\phi)]}{J(\phi)} \quad \text{and} \quad \eta_n = \frac{1}{J(\phi)} \,. \tag{2.19}$$

Boyer et al. [5] showed that the effective viscosity formulation has similar divergences in η_s and η_n in the dense limit, or when $\phi \to \phi_c$.

Lemaitre et al. [70] made a link between inertially dominated (or high Stokes number) dense suspensions and the visco-plastic rheology of dry granular flows from Da Cruz et al. [3]. Trulsson et al. [6] showed that a combined parameter $K = J + \alpha I^2$, with α fitted from experimental data, can interpolate between these two limiting cases. They proposed the following rheological model, using the new parameter, that is reminiscent of the $\mu(I)$ rheology:

$$\phi(K) = \phi_c - b\sqrt{K} \quad \text{and} \quad \mu(K) = \mu_c + \frac{\mu_F - \mu_c}{\sqrt{K_0/K}} \,. \tag{2.20}$$

In the inertially dominated regime the visco-plastic rheology of Da Cruz et al. [3] is recovered, but in the viscous regime this model reduces to that of Boyer et al. [5].

Amarsid et al. [68] proposed a modified inertial number

$$I_m = I\sqrt{1 + \frac{2}{S_t}} = I\sqrt{1 + 2\frac{J}{I^2}} \,, \tag{2.21}$$

which also interpolates between the viscous and inertial regime. In the viscous limit $S_t \to 0$ and $I_m \to \sqrt{\alpha_v J}$ while in the inertial limit $I_m \to I$. They further showed that the effective friction and solids fraction collapse to

$$\phi(I_m) = \frac{\phi_c}{1 + aI_m} \quad \text{and} \quad \mu(I_m) = \mu_c + \frac{\mu_2 - \mu_c}{b/I_m} \,. \tag{2.22}$$

For simulations of 2D discs and a coupled Lattice Boltzmann Method used to simulate the fluid, the following values of the constants were fitted $\mu_c = 0.280 \pm 0.002$ $\phi_c = 0.8123 \pm 0.0003$ $b = 0.246 \pm 0.008$ $\delta\mu = 0.783 \pm 0.010$ $a = 0.750 \pm 0.003$.

The ideas underpinning dense suspensions have found applications in many fields including extrusions (Ness and Sun [46, 47]), sediment transport (Houssais et al. [71], Houssais et al. [72], and Houssais and Jerolmack [73]) and turbulent bedload transport (Maurin et al. [74]).

2.2.4 Kinetic Theory

Early attempts at using the Kinetic Theory (KT) of gases to describe rapid granular flows were made by Lun et al. [8], Jenkins and Savage [9], Jenkins and Richman [10], and Garzó and Dufty [11]. In these models particles are treated like molecules of a molecular fluid. Meso-scopic conservation laws are built around the assumption that in a particular region, the velocity is described by a distribution function, where the average and variance in the velocity (δv) is associated with a granular

temperature $T = (\delta v)^2$, in analogy to the thermodynamic temperature from the kinetic theory of gases. While both thermodynamic temperature and the granular temperature are defined in terms of the fluctuation in velocity, the two quantities are not related [62]. It is assumed that pairwise interactions between particles dominate the flow. This assumption implies that these models are only valid in a range of solids fractions where the flow is relatively dilute.

KT models often describe the flow as a set of functions that relate the pressure, shear stress, shear rate and energy dissipation rate Γ to the granular temperature with a set of non-dimensional functions. For instance the model by Garzó and Dufty [11] states

$$P = \rho_p f_1(\phi, e) T \tag{2.23}$$

$$\tau = \rho_p d \dot{\gamma} f_2(\phi, e) T^{1/2} \tag{2.24}$$

$$\Gamma = \frac{1}{d} f_3(\phi, e) T^{3/2} \ , \tag{2.25}$$

where e is the coefficient of restitution and f_1, f_2 and f_3 are the dimensionless functions. This approach uses the Buckingham-Pi theorem while emphasizing that the granular temperature, or fluctuations of velocity, is another dynamically independent quantity.

While early KT models where limited to their domain of applicability, many improvements were proposed. Kumaran [75] and Lun [76] accounted for particle roughness by introducing rotational degrees of freedom and tangential restitution, while Jenkins and Zhang [77] introduced inter-particle friction. Extensions of KT with an interstitial fluid was made by Garzó et al. [78], Chamorro et al. [79], and Saha and Alam [80], however only at low solids fraction. Jenkins and Berzi [81] and Jenkins [82, 83] added a correlation length associated with the creation of force chains and showed that KT can be applied to dense flows. Berzi and Vescovi [84] showed that the model can be refined further to allow it to be used for volume fractions near the jamming transition. The model by Vescovi et al. [85] was shown to work when the requirement for nearly inelastic spheres (i.e. coefficient of restitution close to unity) is relaxed. They found good agreement with restitution as low as $e = 0.5$.

Chialvo and Sundaresan [12] evaluated two additions to kinetic theory: the length scale to account for force chains by Jenkins and Berzi [81–83] and an effective coefficient of restitution $e_{\text{eff}}(e, \mu_p) < e$, proposed by Jenkins and Zhang [77], to account for energy losses due to friction. They found that they needed to make additional changes to provide a model that predicted the correct pressure, shear stress and granular temperature for dense systems with frictional particles. In particular, they proposed a modified inertial number $I' = I/\phi$ together with a new model for the effective friction

$$\mu(I', \phi) = I_0 \frac{\beta(\phi)(I'/I_0)^{5/2} + \alpha I'/I_0 + \mu_1/I_0}{(I'/I_0)^{3/2} + 1} \ . \tag{2.26}$$

This model is significant, because it bridges Kinetic Theory (KT), which has been successful at describing dilute flows, with the visco-plastic models that describe dense flows.

2.2.5 Non-local Granular Fluidity model

Zhang and Kamrin [15] point out that while the visco-plastic rheology has been very successful to describe flows in the simple shear configuration, there are several reports where the rheology fails. For inclined plane flows, the angle at which the flowing layer stops depends on the thickness of the flowing layer (GDR MiDi [2] and Silbert et al. [86]). Flow was observed in steady but non-uniform flows when $\mu < \mu_s$ (Da Cruz et al. [87] and Koval et al. [88]). Reddy et al. [89] and Nichol et al. [90] have reported that localised agitation of granular media can affect a probe in a far away, non-flowing, region.

These phenomena have been used to motivate a non-local rheology that takes long range effects into account. Kamrin and Koval [13] and Henann and Kamrin [14] introduced a constitutive relation that is based on a granular fluidity. A similar concept, the non local fluidity, has been used to model soft glassy flows by Goyon et al. [91] and Bocquet et al. [92].

The granular fluidity is defined as

$$g = \frac{\dot{\gamma}}{\mu} = \frac{\dot{\gamma} P}{\tau} \,. \tag{2.27}$$

A local granular fluidity is obtained by substituting the viscoplastic model for the effective friction from equation (2.10) and the definition of the inertial number from equation (2.9) into equation (2.27), resulting in:

$$g_{\mathrm{loc}}(\mu, P) = \begin{cases} \frac{\mu - \mu_s}{b\mu} \sqrt{P/m}, & \text{if } \mu > \mu_s \\ 0, & \text{otherwise} \,. \end{cases} \tag{2.28}$$

The granular fluidity is governed by the partial differential equation:

$$\nabla^2 g = \frac{1}{\xi} \left(g - g_{\mathrm{loc}} \right) \,, \tag{2.29}$$

where ξ is the cooperativity length. The role of the cooperativity length is to measure the effect of long range interactions; it diverges as the flow approaches the yield point ($\xi \propto |\mu - \mu_s|^{-1}$). While the cooperativity length goes to zero in the dense flow regime ($\xi \to 0$ as $I \to 1$) so that the model reduces to a local rheology under moderate flow.

Bouzid et al. [16, 17] proposed that the definition of the fluidity be changed to

$$g = \frac{\dot{\gamma} \tau_c}{\tau} = \frac{\dot{\gamma} P}{\tau} \,, \tag{2.30}$$

with τ_c the yield stress at which flow is initiated. However, Zhang and Kamrin [15] argues that the granular fluidity has dimensions of inverse time and postulates that the other relevant time scale is $T = d/\delta v$, where δv is the fluctuation of velocity. Further, if the other independent non-dimensional quantity is taken to be the solids fraction ϕ, then the following relationship should hold:

$$g = \frac{\delta v}{d} f(\phi) \, . \tag{2.31}$$

This relationship showed good agreement for three dimensional sheared flows by Zhang and Kamrin [15]. Bhateja and Khakhar [93] found that (2.31) produces a better collapse than the inertial number for nonlinear flows of two dimensional disks.

2.3 Experimental Techniques

Granular materials have been studied experimentally with a wide variety of methods. Streak line photography where a photograph is taken through a transparent end wall of a rotating drum. The resulting images shows particles as streaks when the shutter speed is set at the correct length relative to the velocity of the particles. It then becomes possible to recover the velocity field of the particles close to the end wall. Morrell [94] has used this technique, along with coloured tracers, to produce a power draw model for industrial tumbling mills. Orpe and Khakhar [23] measured the profile of the free surface in rotating drums. As mentioned earlier Chou and Lee [25], Santomaso et al. [95], and Orpe and Khakhar [96] used similar techniques to test granular rheology models. Jain et al. [97, 98] used Particle Image Velocimetry (PIV) to study the velocity profile in the flowing layer of rotating drums with a wet granular material.

Non-invasive techniques have been developed that allow for the measurement of particle velocities inside the granular material. Nakagawa et al. [99] used Magnetic Resonance Imaging (MRI) to measure the density and velocity in the flowing layer of rotating drums.

2.3.1 Positron Emission Particle Tracking

Positron Emission Particle Tracking (PEPT), developed by Hawkesworth et al. [29], Bemrose et al. [30], and Parker et al. [31], uses a Positron Emission Tomography (PET) scanner to track a single radio labeled particle. During the course of the experiment the radioactive material undergoes β^+ decay by $p \rightarrow n + e^+ + \nu_e$. The positron ($e^+$) is annihilated by a nearby electron soon afterward, which produces two $511\,\mathrm{MeV}$ γ-rays. The positron will have a very small momentum – which must be conserved after the annihilation – causing the γ-rays to be emitted in opposite directions. When such a decay event happens inside the field of view of the PET scanner these gamma rays interact with the detector elements via the photoelectric effect and the position of these elements are recorded. When two gamma rays

interact with detector elements in a short time period of time, these events are assumed to correspond to the same annihilation event and a Line of Response (LOR) can be reconstructed between the detector elements.

Tracers are produced by absorbing a radioactive element onto an ion-exchange resin bead. The ion exchange bead is embedded in a representative particle, usually a particle with a hole drilled, and sealed with epoxy. The tracer isotope is usually selected so that its half-life is long enough to last the duration of the experiment, but short enough so that it can be safely discarded afterward and to pose a minimal contamination risk in the event that the tracer breaks apart. Radioisotopes commonly used for PEPT experiments are ^{66}Ga ($t_{1/2} = 9.45\,\mathrm{h}$), ^{68}Ga ($t_{1/2} = 68\,\mathrm{min}$), ^{18}F ($t_{1/2} = 109\,\mathrm{min}$), ^{61}Cu ($t_{1/2} = 204\,\mathrm{min}$) and ^{64}Cu ($t_{1/2} = 2.7\,\mathrm{h}$) [100].

Even though the precise location of the annihilation event (and hence tracer) is unknown, its position is constrained to be somewhere on the line of response. Using as many as 100 to 400 LORs the position of tracer can be determined. This is done by a triangulation scheme that finds the location that minimises the distance to each LOR and iteratively discards lines furthest from this point until a predetermined number remain. Spurious LORs are removed in this manner and the uncertainty of the tracer's position can be reduced to within $5\,\mathrm{mm}$ for a parallel plate camera (see Parker et al. [101]) and $1\,\mathrm{mm}$ for PET scanners with a ring geometry (see Volkwyn et al. [100]). A snapshot of several LORs is shown in Figure 2.2 before and after the spurious lines are removed.

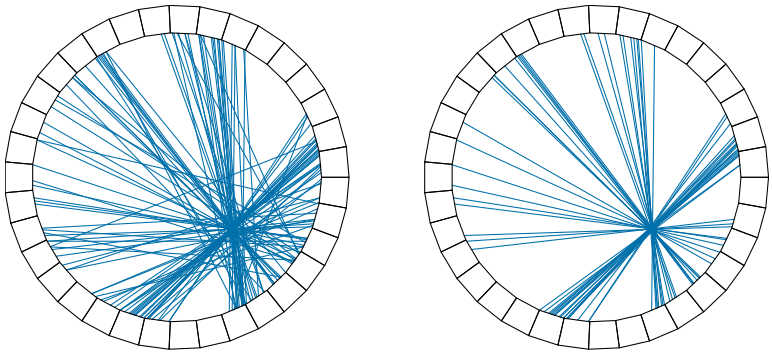

Figure 2.2 – A Line of Response (LOR) recorded by the scanner in the azimuthal plane. It is assumed that each line corresponds to two γ rays emitted from a positron-electron annihilation event in the tracer particle. Some spurious lines can be seen on the left, however the Positron Emission Particle Tracking (PEPT) triangulation algorithm uses a subset of lines that pass close to a common point (right) to resolve the tracer's position.

Multiple particle tracking schemes have been developed by Blakemore [102], Bickell et al. [103], Yang et al. [104], and Gundogdu [105], but these techniques have some draw backs that make them impractical for use in rotating drums. The latest development of multiple particle methods require that all the history of all tracers be known during the experiment. Problematic situations arise when one or more of the tracers [102]:

- come into close proximity of each other,

- leave the field of view of the scanner,
- experience high acceleration,
- γ-rays experience high scattering or attenuation.

All of these conditions can result in a loss of tracking ability and the first two cannot be prevented in a rotating drum experiment. Therefore PEPT is often used to track the position of a only single particle.

2.3.2 The Ergodic Hypothesis

Given that only one particle can be tracked during the experiment, some method is required to recover the kinematic information of the ensemble. The use of the ergodic hypothesis in PEPT was proposed by Wildmann et al. [32], which states that if a system is ergodic, the time average of a single particle should be equal to the spatial average of the ensemble. They tested the 'ergodicity' of their results by calculating variations in the solids fraction in the following way. The spatial domain of the experiment is partitioned into a set of voxels, each centered around a different location (x, y). The number density, the number of particles per unit volume, in a voxel is given by

$$n(x, y) = \frac{N}{V_s} F(x, y) \ , \tag{2.32}$$

where N is the total number of particles in the experiment and V_s the volume of a voxel. $F(x, y)$ is the residence time fraction or the ratio of the amount of time the tracer was present in a particular voxel, $t(x, y)$, to the duration of the experiment T, and is given by

$$F(x, y) = \frac{t(x, y)}{T} \ . \tag{2.33}$$

Finally, the solids fraction in a voxel is given by

$$\phi(x, y) = \frac{\pi d^3}{6} n(x, y) = \frac{\pi}{6} \frac{N d^3}{V_s} F(x, y) \ . \tag{2.34}$$

The ergodicity of the system was then tested by sub-dividing each voxel into 3×3 smaller voxels and comparing the average and standard deviation of the solids fraction in the larger voxel. They found that the relative variation in solids fraction in the 3×3 cells was smaller when the system was dilute. They interpreted this as a sign that the tracer required more time to explore the phase space of the system for dense packing fractions.

Whether a system is ergodic or not is closely related to the chaotic behaviour of the underlying dynamical system (Eckmann and Ruelle [106]). Several techniques of studying chaotic dynamical systems exist and some have been used to study mixers and experimental techniques related to PEPT. Hill et al. [107] compared several rotating mixers by contrasting the dynamical systems that dictate the motion of the charge to study their mixing performance. They used Poincaré maps to study

when segregation and mixing occurs. Doucet et al. [108, 109] used Poincaré maps, Lyapunov exponents and mixing indices to study the chaotic behaviour of a rotary v-blender. Their measurements were made using Radioactive Particle Tracking (RPT), an experimental method similar to PEPT.

2.3.3 PEPT Studies of Rotating Drums

PEPT has been used by Parker et al. [101] to study slowly rotating drums and has since been used to investigate many aspects of rotating drums.

Bbosa et al. [110, 111] studied power consumption of rotating drums. A torque sensor was fitted between the motor and shaft of the drum and the rate of rotation of the drum was measured with a tachometer. The power draw can be calculated from these two measurements. In addition, the power draw was calculated on a per voxel basis, by determining the moment of the particulate mass inside a voxel with regards to the mill center. Both power calculations gave consistent results for PEPT and numerical data.

Sichalwe et al. [112] examined porosity (the fraction of empty space in a volume) to characterise of the charge in tumbling mills. The porosity is defined as $\epsilon(x, y) = 1 - \phi(x, y)$, where the solids fraction (ϕ) is calculated using the residence time fraction method presented in equation (2.34).

PEPT has become an established method measuring charge characteristics in rotating drums. The velocity and/or solids fraction was measured using PEPT in each of the following studies. Alizadeh et al. [113] and Ding et al. [114] studied segregation and mixing properties of polydisperse mixtures of particles. In Kallon et al. [115], circulation rate around the Center of Circulation (CoC) was compared to the drum's rate of rotation.

Scaling laws in the flowing layer (Govender et al. [27]) and granular rheology (Govender and Pathmathas [20]) have also been investigated. In these studies, lines perpendicular to the free surface were identified and the velocity and solids fraction measured as a function of the distance from the free surface.

Morrison et al. [19] investigated features the charge, such as the position of the toe, shoulder and center of circulation, at steady state. The axial transport of slurry through the granular bed was described using a modified Ergun equation by Tupper et al. [116–119]. Velocity and porosity measurements where made using PEPT.

2.4 Numerical Studies

Experiments of granular material requires expensive equipment and are often labour intensive to perform. Numerical studies become standard tools to simulate their behaviour and simulation results are substituted for experimental results. In addition, detailed information about the microscopic system is available. This includes pairwise interactions between particles, which allows the internal stress of the material to be characterised.

Granular particles are modeled as rigid bodies with a coefficient of restitution (e) and a coefficient of friction μ_p (but sometimes $\mu_p = 0$) between particles. Particles have momentum and position and a time stepping scheme is used to model their dynamics. Interactions between particles are modeled in two different ways. The first approach models inter-particle forces and Newton's second law is integrated over a small time and length scale. This will be the approach used in this study (discussed later), however, the second approach bears mention here. Contact Dynamics (CD) ignores inter-particle forces, instead velocities are adjusted in discontinuous ways when collisions are detected. Velocity adjustments can be made such that the effects of restitution and friction are taken into account. Contact Dynamics (CD) can work with a large time step resulting in a potential gain in simulation time and proposals have been made so that the method can work when there are interactions between multiple particles. However, it is not easy to implement (Radjai and Richefeu [120]). In addition, Artoni and Richard [54] points out that their coarsegraining method only applies if the underlying particle properties are smooth variables. See Hedman [121] for a comparison of smooth and non-smooth methods.

2.4.1 The Discrete Element Method

The Discrete Element Method (DEM), proposed by Cundall and Strack [34], was inspired by methods used to simulate Molecular Dynamics (MD). A force is applied between overlapping particles of the general form,

$$\vec{F}_{ij} = F_n(\delta_n, v_n)\hat{n}_{ij} + F_t(\delta_t, v_t)\hat{t}_{ij} \ , \tag{2.35}$$

where F_n and F_t are the components of the force normal and tangential to the line between particle centres, respectively, and are functions of the overlap (δ_n and δ_t) and relative velocity (v_n and v_t). Once the force on a particle is resolved, the velocity and position can be calculated by numerically solving Newton's second law. Because, forces are modeled as differentiable functions, particle velocities are also smooth.

2.4.2 Simulation of Dense Suspensions

The effect of a fluid on the granular material can be modeled in several ways. A coupled approach sees the particles modeled with Discrete Element Method (DEM) and the fluid simulated using Computational Fluid Dynamics (CFD) (Sun and Xiao [35], Malahe [36], Xiao and Sun [37], Kloss et al. [38], and Hu et al. [39]). In one way coupled simulations the forces that the fluid imposes on the particles, such as drag and buoyancy, are considered as an additional force in the DEM simulations. Two way coupled methods also exist, where the momentum transfer from particles to the fluid is also accounted for. The Stokes number plays an important role to determine which coupling to apply in these methods. At very small Stokes numbers the drag forces on the particles dominate their dynamics and it becomes feasible to simulate only the fluid (Xiao and Sun [37]). At large Stokes numbers the particle momentum dominates the fluid and accounting for lubrication effects does not

affect the outcome of the simulation (Sun and Xiao [35]). There exist conditions in between these extremes where a one way coupling is sufficient or when a two way coupled simulation is required.

Smooth Particle Hydrodynamics (SPH), described in detail in Liu and Liu [122], is a mesh-free method for solving the Partial Differential Equation (PDE). Instead of defining a rigid lattice as the domain on which the PDE is solved, a series of points are defined and allowed to move. The continuum solution to the PDE is recovered by an averaging scheme that is mathematically similar to coarsegraining in a granular material. Potapov et al. [123] and Cleary et al. [124] describe how SPH can be used to simulate the fluid phase of granular suspensions while particles are simulated using DEM. DEM-SPH has been used to simulate industrial scale tumbling mills that can account for breakage (Cleary et al. [40, 41]).

2.4.3 The Lubrication Approximation

Trulsson et al. [6], Seto et al. [45], and Ness and Sun [46, 47] studied dense suspensions using DEM simulations with additional forces acting on the particle that approximate the effect of a fluid. A lubrication force, described in Cox [42], Kim and Karrila [43], and Ball and Melrose [44], acts between two particles when they are separated by a liquid film h_{ij} thick, then the force that particle i exerts on particle j is given by,

$$F_{ij}^{\text{lub}} = F_n^{\text{lub}}(\eta_f, \vec{v}_i - \vec{v}_j, h_{ij})\hat{n}_{ij} + F_t^{\text{lub}}(\eta_f, \vec{v}_i - \vec{v}_j, h_{ij})\hat{t}_{ij}. \tag{2.36}$$

Here, $d_{ij} = 2d_i d_j/(d_i + d_j)$ and $\hat{n}_{ij}$ and $\hat{t}_{ij}$ are the normal and tangential unit vectors, respectively. Trulsson et al. [6] and Seto et al. [45] also added a drag force $\vec{F}_i^{\text{drag}} = 3\pi\eta(\vec{v}_f(\vec{x}_i) - \vec{v}_i)$, with $\vec{v}_f$ the fluid velocity, and an Archimedes force, $\vec{F}_i^{\text{archi}} = \phi(1-\phi)^{-1}\vec{F}_i^{\text{drag}}$, when the fluid has a stress gradient. However, Ness and Sun [46, 47] omitted drag and Archimedes forces because they found that energy dissipation due to the lubrication force dominated other fluid effects. In addition Trulsson et al. [6] showed that particle contact forces was the dominant mechanism of energy dissipation in the high Stokes regime.

The approach outlined above has several benefits over coupled DEM-Computational Fluid Dynamics (CFD) and SPH methods. The computational complexity is greatly reduced because the fluid is not simulated explicitly. This means that only a DEM software package can be used. There is a potential speed up. However, care needs to be taken to ensure that the simulated results still resemble a real world example.

Govender et al. [125] performed a validation study comparing a rotating drum simulated with DEM and no fluid with experimental results from PEPT. The experimental and simulated system was operating in the cataracting regime. The experiments were performed with $5\,\text{mm}$ glass beads and, in one case recirculating water and another with a sand/water mixture. They found good agreement between simulation and experiments despite the fact that the simulations did not account for viscous

effects on the solids. This suggests that the Stokes number was large, and, according to regime map from Courrech du Pont et al. [7], implies that rotating drums in the rolling regime correspond to the high Stokes regime.

2.5 Summary

Dimensional analysis of dense granular flows and dense granular suspension has lead to a variety of models that describe flows at the meso scale. These models have become increasingly sophisticated by incorporating an increasing number of physical quantities, which carry units of mass, length and time. When considering additional quantities, more time scales are present in the problem which present additional possibilities to construct dimensionless numbers that describe the flow behaviour. GDR MiDi [2] introduced pressure, which lead to the inertial number I, while Boyer et al. [5] considered the fluid viscosity and identified the viscous number J as a key dimensionless quantity that describes dense suspensions when viscous forces play a dominant role in the dynamics. Further progress was made by introducing a combined quantity $K = J + \alpha I^2$, that is able to interpolate between the inertial regime and the viscous regime. The Stokes number is an important quantity that determines the behaviour of particle/fluid interactions.

To study these models, appropriate methods for measuring particle level quantities and coarsegraining the results to produce the continuum level fields are required. The coarsegraining method described by Babic [53] and refined by Goldenberg and Goldhirsch [51] and Artoni and Richard [54] presents a method for constructing the required continuum fields. The method is very general and specialisations can be made to suit specific situations by the choosing a suitable kernel function and associated averaging width. Tools for measuring particle level data include a host of experimental and numerical techniques. PEPT, an established experimental method, has advantages such as being able to take non invasive measurements and probe the interior of the flow. However it can only measure the position of a small number of particles and in many cases only one tracer particle is measured. The ergodic hypothesis is required to draw conclusions about the average behaviour of the ensemble of particles. Numerical tools include DEM to simulate particle interactions and CFD, SPH and lubrication approximation to simulate the fluid. Coupled DEM simulations with CFD and SPH require integration between different software packages and additional computational resources. On the other hand the lubrication approximation can be implemented inside existing DEM software, but ignores some fluid effects, such as drag, that may have a significant impact on the dynamics.

3 Numerical Simulations of Dense Granular Suspensions

Many industrial systems contain a mixture of fluids and granular solids. In this work the lubrication approximation is used to model the effects of a fluid on solids instead of simulating the fluid explicitly using a coupled Computational Fluid Dynamics (CFD)/ Discrete Element Method (DEM) system. This approach has been used to study dense granular suspensions in the simple shearing configuration by Trulsson et al. [6], Seto et al. [45], and Ness and Sun [46]. In addition, in the high Stokes regime the dynamics is dominated by particle interactions and only first order fluid effects needs to be taken into account.

A rotating drum configuration is used with various rotation rates in the cataracting regime; as in Mellmann [56] and depicted in Figure 2.1. The dynamics of a drum's content is very rich, spanning the solid, liquid and gas phase of granular flow. Rotating drums in the sliding and slumping regimes have been studied in the context of granular rheology by GDR MiDi [2], Orpe and Khakhar [23], Chou and Lee [25], and Pignatel et al. [26], but tests of granular rheology in rotating drums in the cataracting regime is sparse. Rotating drums have many applications and are used in industry for mixing and grinding, typically operated at higher Froude number.

3.1 The Discrete Element Method

The Discrete Element Method (DEM) [34] is a numerical model used to simulate the dynamics of a large number of particles. It is widely used to simulate discontinuous material especially granular flow, powder mechanics and rock mechanics. The LIGGGHTS [38] software package was employed to perform the simulations in this work. LIGGGHTS is distributed under an open source license which allowed for an implementation of the lubrication approximation to be added, as in Ness and Sun [46, 47].

LIGGGHTS imposes a force on each particle and uses the Verlet integration scheme to solve Newton's equation of motion and advance the simulation by an incremental time step. The force on particle i, in contact with N_C particles and nearby N_L particles, can be expressed as

$$F_i = \sum_{j=1}^{N_C} F_{ij}^C + \sum_{k=1}^{N_L} F_{ik}^L + F_i^B, \tag{3.1}$$

where F_{ij}^C is the contact force between particles i and j and F_{ik}^L is the lubrication force between particles i and k. In addition to contact forces, F_i^B represents the

sum of the body forces acting on particle i, which could be gravity or interactions between particles and external geometries.

3.1.1 Contact Forces

The contact force between two spheres is modeled as two harmonic oscillators at normal angles to each other – one for the normal force and one for the tangential force (see Figure 3.1). The force between two spheres can be written as,

$$\vec{F}_{ij} = \underbrace{(k_n \delta_n - \gamma_n v_n)}_{F_n} \hat{n}_{ij} + \underbrace{(k_t \delta_t - \gamma_t v_t)}_{F_t} \hat{t}_{ij} \ , \tag{3.2}$$

where $\delta_n = D_p - d$ is the overlap between two spheres, k_n and k_t are elastic constants for normal and tangential components respectively, and γ_n and γ_t are the visco-elastic damping constraints for normal and tangential components respectively. The tangential displacement δ_n is the displacement normal to the line of contact since the contact was initiated.

The relationship between the tangential and normal component of the force is further constrained by the coefficient of friction μ, and

$$F_t \leq \mu F_n \ . \tag{3.3}$$

Specific models make choices for k_n, k_t, γ_n and γ_t to allow the force to be proportional to the depth of overlap (known as Hookian models) or the cross-sectional area of the overlap (known as Hertzian models).

In the case of the Hookian contact model, the coefficients of (3.2) are given by

$$k_n = k_t = \frac{16}{15}\sqrt{R^*}Y^* \quad \text{and} \quad \gamma_n = \gamma_t = \sqrt{\frac{4m^* k_n}{1 + (\pi / ln(e))^2}} \ , \tag{3.4}$$

where e is the coefficient of restitution. The force is linear in the overlap δ_n and δ_t.

In the case of the Hertzian contact model the force is related to the overlap by $F \propto \delta^{3/2}$ by choosing the coefficients for the normal force

$$k_n = \frac{4}{3}Y^*\sqrt{R^* \delta_n} \quad \text{and} \quad \gamma_n = -2\sqrt{5/6}\beta\sqrt{S_n m^*} \tag{3.5}$$

Table 3.1 – Comparison of Hookean and Hertzian contact models from Di Renzo and Maio [126, 127].

	Hookian	Hertzian
k_n	$\frac{16}{15}\sqrt{R^*}Y^*$	$\frac{4}{3}Y^*\sqrt{R^*\delta_n}$
γ_n	$\sqrt{\frac{4m^*k_n}{1+(\pi/ln(e))^2}}$	$-2\sqrt{5/6}\beta\sqrt{S_n m^*}$
k_t	k_n	$8G^*\sqrt{R^*\delta_N}$
γ_t	γ_n	$-2\sqrt{5/6}\beta\sqrt{S_t m^*}$

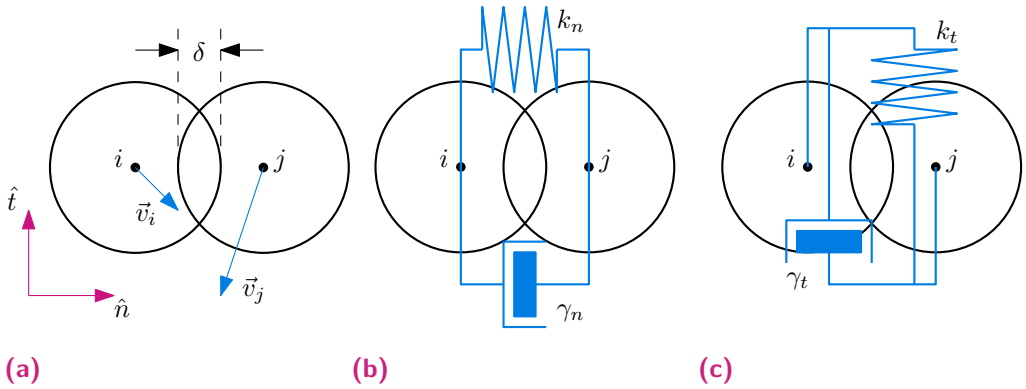

Figure 3.1 – (a) DEM model contacts between two spheres i and j (with velocity v_i and v_j, respectively) as two damped harmonic oscillators. (b) The component of the forces normal to the line that connects their centers are given by $F_n = k_n\delta - \gamma_n v_n$, (c) while the component of the forces tangential the line are given by $F_t = k_t\delta - \gamma_t v_t$.

and for the tangential force

$$k_t = 8G^*\sqrt{R^*\delta_N} \quad \text{and} \quad \gamma_t = -2\sqrt{5/6}\beta\sqrt{S_t m^*}\,, \tag{3.6}$$

with

$$S_n = 2Y^*\sqrt{R^*}\delta_n\,, \quad S_t = 8G^*\sqrt{R^*}\delta_n \quad \text{and} \quad \beta = \frac{\ln(e)}{\sqrt{\ln^2(e)+\pi^2}}\,. \tag{3.7}$$

In both contact models the equivalent Young's modulus and shear modulus of two contacting bodies of dissimilar materials are given by

$$\frac{1}{Y^*} = \frac{1-\nu_1^2}{Y_1} + \frac{1-\nu_2^2}{Y_2} \quad \text{and} \quad \frac{1}{G^*} = \frac{2(2-\nu_1)(1+\nu_1)}{Y_1} + \frac{2(2-\nu_2)(1+\nu_2)}{Y_2} \tag{3.8}$$

where ν the Poisson ratio, Y the Young's modulus and G the shear modulus of the two materials.

When the contacting particles have different sizes, the equivalent radius and mass is given by

$$\frac{1}{R^*} = \frac{1}{R_1} + \frac{1}{R_2} \quad \text{and} \quad \frac{1}{m^*} = \frac{1}{m_1} + \frac{1}{m_2}\,, \tag{3.9}$$

respectively.

The contact model only accounts for physical collisions between particles and ignores the effect of a fluid between the particles.

3.1.2 The Lubrication Approximation

To account for viscous effects of a fluid between the particles, a force is applied that approximates lubrication effects of the fluid. When two particles are near each other the effect of a viscous liquid in the gap between them is approximated with a

lubrication force. The force can be approximated by (Cox [42] and Ball and Melrose [44])

$$F_{ij}^{n}(h_{ij}) = \frac{3}{2}\pi\eta_f \frac{d_{ij}^2}{h_{ij}}(v_i - v_j)\cdot n_{ij}n_{ij}\ , \quad \text{and} \tag{3.10}$$

$$F_{ij}^{t}(h_{ij}) = \frac{4}{5}\pi\eta_f d_{ij}\left[1 + \frac{d_{ij}}{d_i + d_j} + \left(\frac{d_i - d_j}{d_i + d_j}\right)^2\right]\ln\left(\frac{d_{ij}}{2h_{ij}}\right)(v_i - v_j)\cdot(I - n_{ij}n_{ij})\ , \tag{3.11}$$

where h_{ij} is the gap between the particles, $d_{ij} = \frac{2d_i d_j}{d_i + d_j}$ is the effective grain diameter and n_{ij} and t_{ij} is the normal and tangential unit vectors, respectively. The lubrication force is only applied when two particles are close together and in this case it is required that $h_{ij} < 0.05d_{ij}$. Ness and Sun [46] found that when this cutoff was set at $0.1d_{ij}$ there was no significant difference in results. Further, a minimum separation is imposed to prevent divide-by-zero errors, so that when particles are closer together than $h_{ij} < 0.001d_{ij}$, the separation is taken as $h_{ij} = 0.001d_{ij}$.

The lubrication approximation described here applies a force that is proportional to the viscosity of the fluid and the relative velocity of the two particles. The effect of the force is that, as the viscosity increases, variation in the particle velocity is reduced. Further, the condition that determines when the force is applied implies that the force only acts on pairs of particles that are not overlapping, but still close together.

The lubrication force was only applied between nearby particles and not in particle-wall interactions. However, the lubrication approximation is not applied when particles are in contact. At the drum wall, particles usually make contact with the wall and an implementation of particle-wall lubrication interactions will have no effect in the vast majority of particle-wall interactions. Further, there are two technical reasons why lubrication forces are not applied to particle-wall interactions. Firstly, equations (3.10) and (3.11) depend on the diameter of both particles (through d_{ij}) and an extension interaction with flat walls (where $d_i \to \text{inf}$) is mathematically challenging. Secondly, LIGGGHTS applies wall-particle interactions separately from particle-particle interactions and the code implemented for the particle-particle interaction could not be simply applied to wall-particle interactions.

3.2 Simulation configuration

A LIGGGHTS simulation is carried out by invoking the LIGGGHTS executable with a text input file. The text file contains instructions to LIGGGHTS about the details of the simulation. LIGGGHTS allows the entire simulation state to be saved to hard disk and the saved state can then be loaded by other simulations. This facility was used to perform a particle generation simulation to prepare an initial state that could be loaded by later simulations in which the rotation speed and viscosity of the fluid was varied.

3.2.1 Particle Generation

Particle generation is done in a separate simulation. The drum's geometry is loaded from disk, a cylinder with radius $R = 200\,\mathrm{mm}$ and length $L = 200\,\mathrm{mm}$. To simplify the interpretation of results no lifter bars are present on the internal geometry of the cylinder. Slipping between particles and the wall was prevented by applying contact interactions with a coefficient of friction $\mu = 0.5$. The particle properties are defined with diameter $D_p = 10\,\mathrm{mm}$ and density $\rho_p = 2400\,\mathrm{kg/m^3}$. The material properties of the particles are Young's modulus $Y = 5 \times 10^6\,\mathrm{kg/m/s^2}$, Poisson ratio $\nu = 0.45$, coefficient of restitution $e = 0.5$ and coefficient of friction $\mu = 0.5$. Gravitational acceleration is set at $g = 9.8\,\mathrm{m/s^2}$ perpendicular to the axis of the drum.

The simulation is run for $1\,000\,000$ steps during which the simulation time is advanced by $\Delta t = 1 \times 10^{-6}\,\mathrm{s}$. Every $0.001\,\mathrm{s}$ (or every 1000 steps). A horizontal cylindrical region is defined that is smaller than the drum's dimensions and enclosed by the drum's geometry. LIGGGHTS is instructed to insert 500 particles at random locations in the cylindrical region. Once a particle is created it is allowed to fall under gravity and interact with other particles according to the Hertz-Mindlin model outlined in the previous section. When a newly inserted particle overlaps with an existing particle, it is deleted to prevent excessive forces that could cause instabilities in the simulation. Particles are created until a total $15\,000$ exist in the simulation, which is equivalent to a $50\,\%$ filling of the drum's volume.

3.2.2 Continued Simulations

LIGGGHTS provides the ability to save the simulation state. A simulation state can then be loaded and continued under different parameters. This feature is used to load the simulation state that existed at the end of the particle generation simulation together with same drum geometry. The desired rotation rate and fluid viscosity can be specified in the subsequent simulations. Different rotation rates and viscosities were used in separate simulations; the values of these parameters are listed in Table 3.2. LIGGGHTS only allows the period of rotation (T) to be set which is related to the angular velocity ω, Froude Number F_R and critical speed by

$$\omega = \frac{2\pi}{T}\,, \quad F_r = \frac{\omega^2 R}{g} \quad \text{and} \quad \omega_C = \sqrt{\frac{g}{R}} = 7.0\,\mathrm{s^{-1}}\,. \tag{3.12}$$

The lubrication force described in the previous section is applied in addition to the Hertz-Mindlin contact force.

Viscosity values were chosen to cover as wide a range of the Stokes number as possible. The shear rate in a rotating drum of the proportions used in this study was estimated from previous work by Govender et al. [27] at $\dot{\gamma} \approx 20\,\mathrm{s^{-1}}$. Flows over a range of Stokes number, given by

$$S_t = \frac{\rho_p d^2 \dot{\gamma}}{\eta_f}\,, \tag{3.13}$$

Table 3.2 – Simulation parameters that were varied across different simulations and the virtual time each simulation was allowed run. The rotation rate of the drum is given in RPM, angular velocity ω, as a percentage of the critical velocity ω_c and Froude Number F_r. The relationship between these quantities are shown in (3.12).

					Viscosity (η_f) [Pa s]			
Rotation Speed	RPM	ω [s^{-1}]	%ω_c	F_r	0.001	0.01	0.03	0.22
	20.1	2.1	30	0.09	5 s	5 s	5 s	5 s
	26.7	2.8	40	0.16	11 s	11 s	5 s	5 s
	33.4	3.5	50	0.25	6 s	6 s	5 s	5 s
	40.1	4.2	60	0.36	6 s	6 s	5 s	5 s

of $S_t \sim 10$ to $S_t \sim 100$ can be investigated by choosing viscosities of $\eta_f \in \{0.01, 0.03, 0.22\}$ Pa s. Fluids of these viscosities can also readily be prepared by mixing water and glycerol with ratios of 60 %, 75 % and 90 % by weight, respectively. Every 10 000 time steps (or every 0.01 s of simulation time) each particle's position and velocity is saved to disk. Additionally, for each particle that is interacting with another particle via a contact or lubrication force, the position of both particles and the force between them is saved. Figure 3.2 shows a snapshot of a simulation with the drum and particles.

The simulations where performed on Dell PowerEdge C6145 servers. Simulation time was between 27 h and 30 h to complete 1 s of simulation time. Even though LIGGGHTS supports multi core processing via the Message Passing Interface (MPI), the open source version does not perform load balancing while a simulation is running. LIGGGHTS partitions the simulation space in a 3D grid. Each partition is assigned to a processor and all particles inside a partition is assigned to the same processor. It was found that simulations were carried out faster when no multi processing was implemented and a single processor assigned per simulation, likely because when adjacent particles are assigned to different processors there is significant overhead due to inter processor communication.

Figure 3.3 (a) shows the power, calculated by

$$P = \tau\omega \,, \tag{3.14}$$

where τ is the torque exerted on the drum through contact forces with the particles averaged over the duration of the simulation. The power dissipation is increased by both the rotation rate of the drum and the viscosity of the fluid. Torque versus time for the simulations where $\omega = 0.6\omega_c$ is shown in Figure 3.3 (b). The torque follows a constant trend even after a few seconds of simulation time, indicating that the simulation has reached a steady state. The torque is also increased by increased viscosity of the fluid. The increased energy dissipation at higher viscosity is due to the viscous forces between particles applied by the lubrication approximation.

Figure 3.4 shows a two dimensional projection of particles within $5d$ of the drum's axial center for each of the simulations, with $\eta_f = \{0.001, 0.03, 0.22\}$ Pa s that

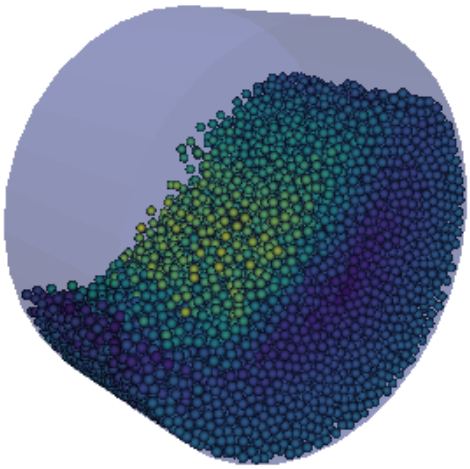

Figure 3.2 – A snapshot of the DEM simulation of a rotating drum using the LIGGGHTS software package.

were used in this study. Results for $\eta_f = 0.01\,\mathrm{Pa\,s}$ are visually very similar to $\eta_f = 0.03\,\mathrm{Pa\,s}$ and are therefore not shown. Each disk represents a particle and the color corresponds to the particle's speed, going from $0\,\mathrm{m\,s^{-1}}$ (dark green) to $2\,\mathrm{m\,s^{-1}}$ (yellow). The effect of the lubrication approximation is also evident as the viscosity is increased. The S-shaped free surface deforms when going from $\eta_f = 0.001\,\mathrm{Pa\,s}$ to $\eta_f = 0.03\,\mathrm{Pa\,s}$ and the S-shape disappears when $\eta_f = 0.22\,\mathrm{Pa\,s}$. The velocity profile perpendicular to the free surface and drum surface changes with viscosity, because the lubrication approximation, in equations (3.10) and (3.11), applies a force that resists the relative motion of particles and is proportional to η_f.

3.3 Discussion

This chapter presented DEM as the numerical scheme used to study rotating drum granular flows in this work. The inter-particle forces – the contact model and lubrication approximation – was described as well as details of running a LIGGGHTS simulation and the different parameters that were varied in the study.

The particle level information extracted from DEM simulations are used in later chapters as the inputs to the coarsegraining scheme. Coarsegrained data is then used to make comparisons between numerical simulations and experimental results (in particular to interrogate the viscous assumption) and to study the rheology of dense granular suspensions in a non-linear environment. The details of the experimental method used in this study is the subject of the next chapter.

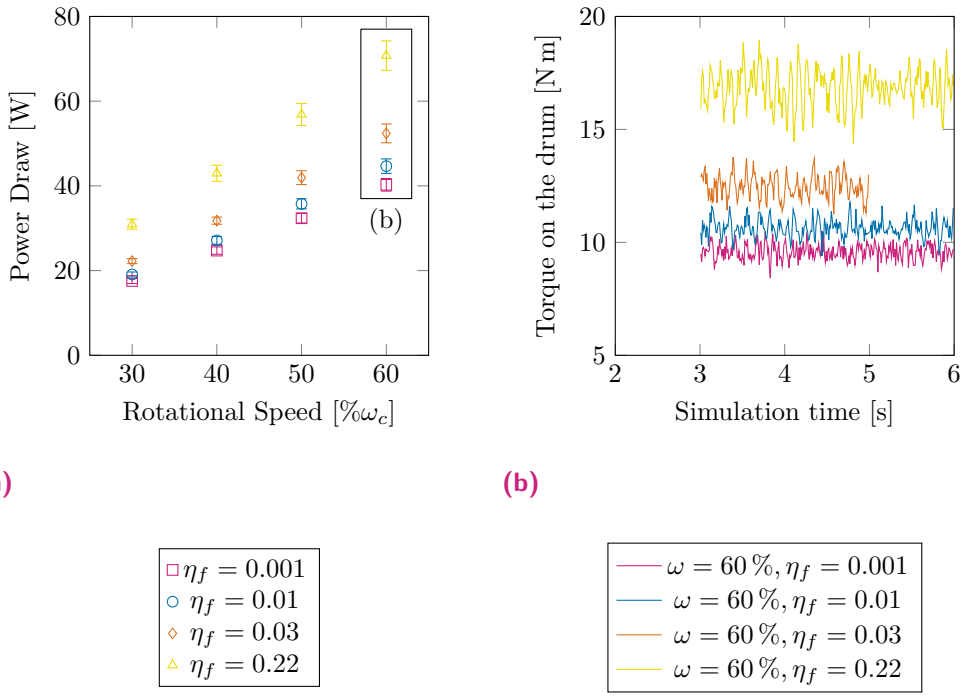

Figure 3.3 – (a) The power dissipation by the drum (b) The torque exerted on the drum by the particles for $\omega = 0.6\omega_c$. Units of viscosity (η_f) is $\mathrm{Pa\,s}$.

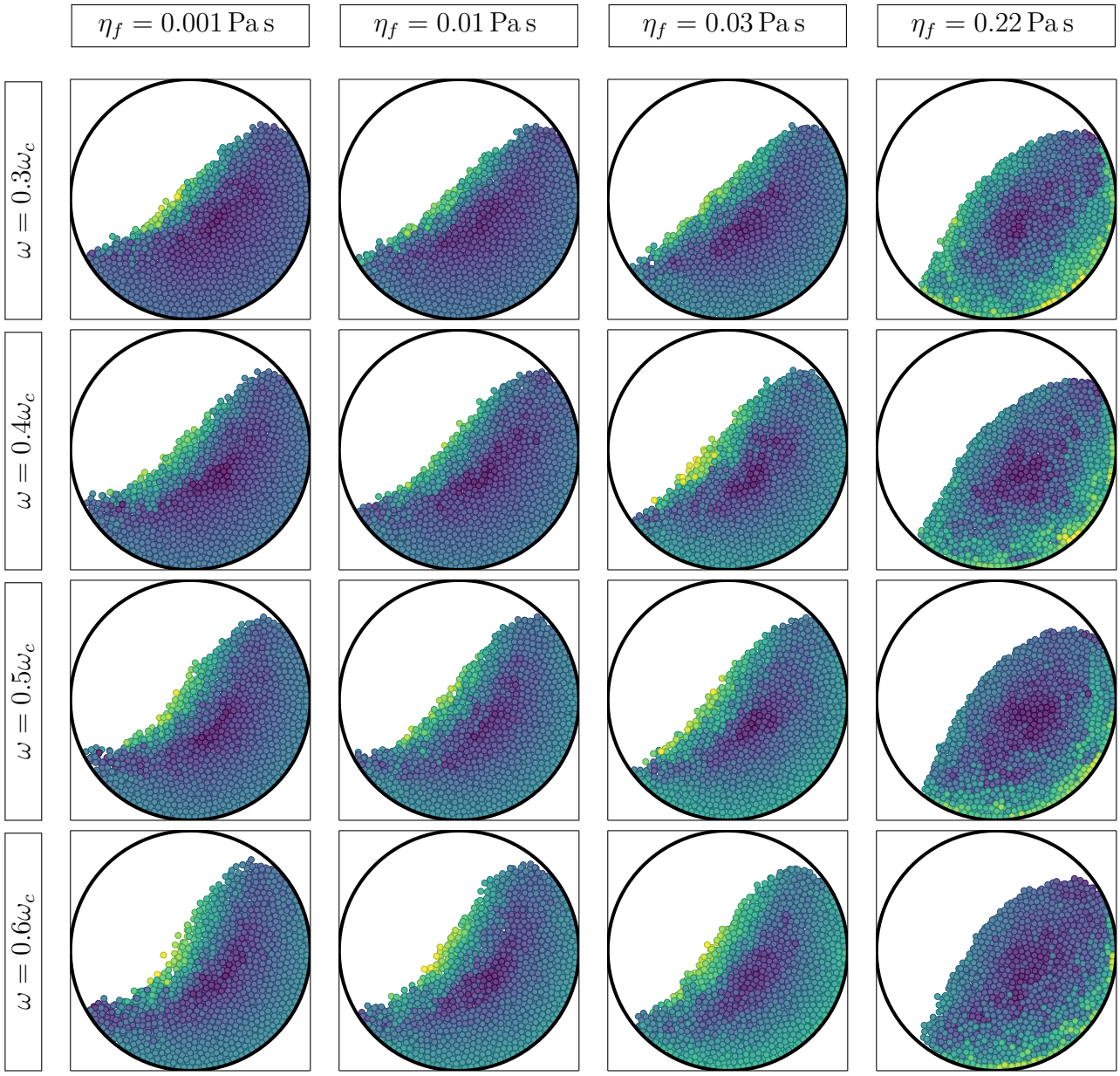

Figure 3.4 – A 2D projection of particles that are within $5d$ of the drum center at the last time step of each simulation. Each disk represents a particle and the color corresponds to the particle's speed. The drum speed is reported as a fraction of the critical speed $\omega_c = 7.0\,\mathrm{s}^{-1}$ and given in (3.12).

4 Coarsegraining in Granular systems

The previous chapter discussed Discrete Element Method (DEM) and the following chapter will discuss Positron Emission Particle Tracking (PEPT), the two methods used to record particle scale data in this work. However, the models discussed in Chapter 2 require a continuum description of the bulk material. Coarsegraining in the context of this thesis refers to the method of building the continuum description for granular systems from particle scale data (see Figure 4.1).

The mathematical formulation of the upscaling method used in this thesis is discussed in this chapter. Some of the implications of the choices of parameters used in formulating the upscaling method are presented and examples of how the method works on data from the DEM simulations reported in Chapter 3 are given. This chapter also discusses how the same method can be applied to data from the PEPT experiments in Chapter 5.

4.1 The Coarsegraining Method

4.1.1 Averaging

Data from DEM simulations provides quantities, such as position and velocity, that are attributed to each sphere. However, a continuum description of granular flow is more appropriate when trying to model macroscopic behaviour. Therefore a technique is needed that recovers the average behaviour of a quantity near a point based on the particle level quantities of the particles near that point. In this work the upscaling from the microscopic, or point-wise, description to the mesoscopic, or continuum, description is done using the coarsegraining technique developed by Glasser and Goldhirsch [52], Babic [53], and Artoni and Richard [54].

According to this procedure the average quantity of any particle property (such as a component of the velocity or kinetic energy, but denoted ψ in general), can be calculated at a particular spatial location, or probe point, $\vec{x}$ and time t using

$$\rho(\vec{x},t)\psi(\vec{x},t) = \int dt' \sum_p m_p \psi_p w_p = \int dt' \sum_p m_p \psi_p K(\vec{x}-\vec{x}_p, t-t_p, W)\ , \quad (4.1)$$

where m_p is the mass of the particle and the sum is carried out over all particles. The smoothing function K assigns a weight to each term in the sum that is dependant on the particle's distance from the averaging position $\vec{x}$ and the time duration between when the particle was at that position to the time at which the average is evaluated. Furthermore, the smoothing radius W allows us to exclude points when when they are too far from the probe point or when $|\vec{x}-\vec{x}_p| > W$ by requiring that $K \to 0$ for

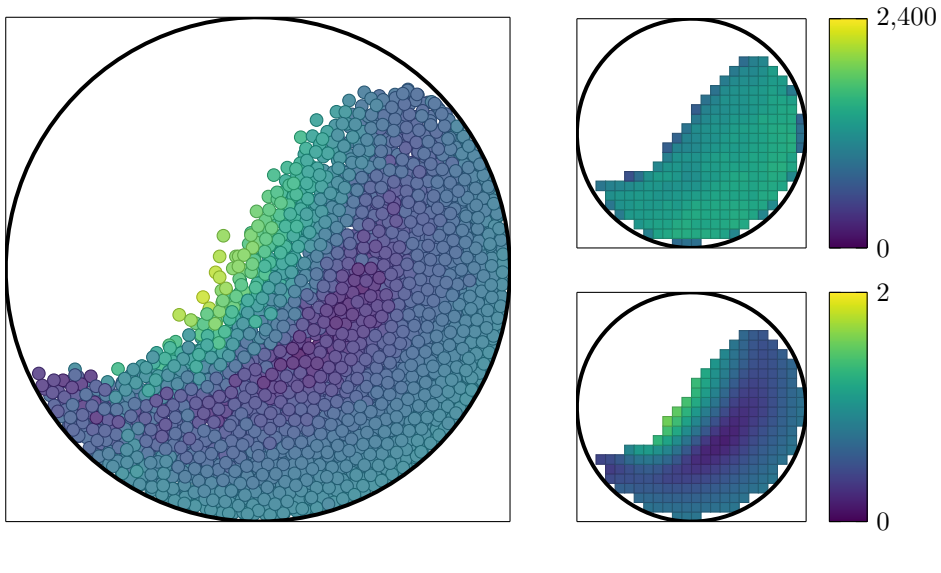

Figure 4.1 – Coarsegraining is the process that averages particle scale information in the microscopic picture (a) to a series of functions of spatial coordinates in (b) the average density (top) and magnitude of the velocity (bottom).

particles that are far away from the probe point compared to the smoothing radius. The smoothing radius introduced by the smoothing function will determine how far a particle needs to be from the probe point before it will contribute to the average. The quantity $\rho(\vec{x}, t)$ is the average density of the bulk material and is given by,

$$\rho(\vec{x}, t) = \int dt' \sum_p m_p w_p \ , \tag{4.2}$$

where m_p is the mass of the sphere and $w_p = K(\vec{x}-\vec{x}_p, t-t_p, W)$ is a weighting factor. The smoothing radius defines a volume around the probe point $\vec{x}$ and equation (4.2) calculates the average density inside the volume. The integral over time makes the effective volume four dimensional and allows significant statistical information to be captured even when the spatial dimensions of the averaging volume are small compared to the size of a particle.

We would expect that a suitable method for coarsegraining be independent of the choice of the smoothing length. The original method proposed by Babic [53] calculated the fluctuation in a particle quantity using

$$\bar{\psi}_p = \psi_p - \psi(\vec{x}), \tag{4.3}$$

in other words the difference between the particle property and the average evaluated at the probe location $\vec{x}$. Babic makes the "continuum assumption" which is that there exists a volume where affine velocity fields are locally uniform. However, the lack of scale separation (the spatial variation of variables are of the same order of magnitude as particle sizes) implies that such a volume cannot be defined for

3D flows. As a consequence, the fluctuations in kinetic energy (ϵ^T) is proportional to the averaging scale (D), $\epsilon^T \sim (\dot{\gamma}D)^2$. Artoni and Richard [54] proposed a new method to calculate fluctuations to overcome this limitation. They redefined the velocity fluctuation of a particle ($\tilde{v}_p$) with respect to the averaged velocity ($\bar{v}$) at the particle centre ($\vec{x}_p$), instead of at the centre of the averaging volume:

$$\tilde{\psi}_p = \psi_p - \psi(\vec{x}_p). \tag{4.4}$$

This scheme requires that the averaged quantity be evaluated at each of the particle locations which would require enormous computational resources. Instead, the $\psi(\vec{x}_p)$ is approximated to first order using

$$\psi(\vec{x}_p) \approx \psi(\vec{x}) + (\vec{x}_p - \vec{x}) \cdot \nabla\psi(\vec{x}) \ , \tag{4.5}$$

where the average velocity and its gradient is calculated at the probe point $\vec{x}$. Now the fluctuation of a particle property in (4.4) can be written as,

$$\tilde{\psi}_p = \psi_p - \psi(\vec{x}) - (\vec{x}_p - \vec{x}) \cdot \nabla\psi(\vec{x}) \ . \tag{4.6}$$

Three assumptions are needed for the approximation in (4.5) to hold: (1) there exists a scale where the gradient of the averaged quantity is smooth, (2) if this scale is the same as the scale introduced by the weighting function the gradient can be approximated by a constant near the averaging point, and (3) there is a homogeneous distribution of particle centres near the averaging point. Artoni and Richard [54] showed that energy and velocity fluctuations are independant of the averaging size when they are calculated using (4.6) and the above assumptions hold. Choosing a differentiable smoothing function allows one to calculate the gradient of a particle property by taking the gradient of (4.1) and applying the product rule:

$$\rho\nabla\psi = \int dt' \sum_p (\nabla w_p) m_p \psi_p - \psi \int dt' \sum_p (\nabla w_p) m_p \ . \tag{4.7}$$

Notice that we are only evaluating the gradient of the smoothing function on the right hand side of the equation and therefore we do not need to resort to a finite difference type of approach when calculating spatial derivatives.

4.1.2 Internal forces

The continuum material has inertial forces that arise from two phenomena. The first is called the contact stress and is due to the physical interactions between particles. It is given by

$$\sigma^c = \int dt' \sum_p \sum_{q>p} w_{pq} \vec{I}_{pq} \vec{f}_{pq} \ , \tag{4.8}$$

where f_{pq} is the force between particles p and q and $\vec{I}_{pq} = \vec{x}_p - \vec{x}_q$ is the branching vector. The contribution to the contact stress σ^c of each pair of particles is the

projection of the force between them onto the vector that joins their centres. The averaging weight is given by

$$w_{pq} = \int_0^1 ds\; w(\vec{x}_p + s\vec{I}_{pq} - \vec{x}, t' - t)\;. \tag{4.9}$$

The integral samples and averages the weighting function between the probe point $\vec{x}$ and every point between the particle locations $\vec{x}_p$ and $\vec{x}_q$.

The second contribution to the internal forces is due to particle vibration, or the average deviation from the mean velocity, and is called the kinetic stress, given by

$$\sigma^k = -\int dt' \sum_p w_p m_p \tilde{v}(\vec{x}_p)\tilde{v}(\vec{x}_p)\;. \tag{4.10}$$

Here the fluctuation in the velocity is defined as in (4.6):

$$\begin{aligned}\tilde{v}(\vec{x}_p) &= v_p - v(\vec{x}_p) \\ &\approx v_p - v(\vec{x}) - (\vec{x}_p - \vec{x}) \cdot \nabla v(\vec{x})\;.\end{aligned} \tag{4.11}$$

4.1.3 Boundaries

The coarsegraining scheme described above calculates an average value at a probe point based on a spacial average in the neighbourhood of the probe point. There are two consequences of this when the probe point is near a boundary and the averaging region overlaps the boundary. Firstly, averaged values will be smaller for probe points inside the boundary, and secondly, averaged values will be non-zero for probe points outside the boundary.

The situation is illustrated in Figure 4.2. The solids fraction is sampled along a line s. Three probe points (dots) are shown with their averaging regions (circles with radius w). In (b) the solids fraction starts to decrease at a distance w before the drum wall and remains non-zero at a distance w away the drum.

The gradual change in solids fraction around the free surface is expected. However, a gradual change near boundaries, such as the drum wall, seems artificial. A sharper change in solids fraction near the drum wall can be accomplished by choosing a smaller averaging region (w) and by choosing a cutoff value for the solids fraction. In this thesis a solids fraction cutoff of $\phi_c = 0.01$ was chosen and all averaged values set to zero for probe points where $\phi < \phi_c$. However, some probe points still exist with non-zero averaged values outside the wall.

4.2 Post-processing

DEM simulations outputs the position and velocity of each particles as well as the forces between particles that are in contact with each other. A set of probe locations, $\vec{x}$, are chosen. In the case of a rotating drum, these locations are chosen in the xy-plane with the z coordinate half way between the end walls. The analysis of

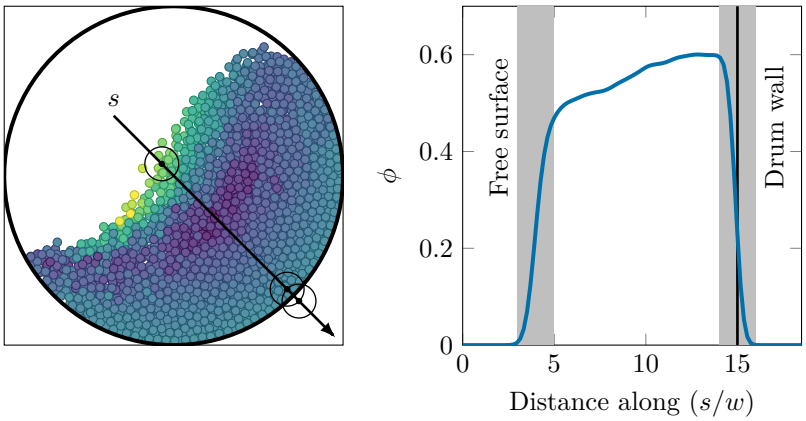

Figure 4.2 – Coarsegraining near boundaries: the averaged quantity at a probe point (represented by dots on the left) near a boundary can be under sampled when the averaging region (black circles) overlaps with the boundaries. Non-zero averaged values are possible for probe points outside the boundary for overlapping averaging regions. Right: This causes a smooth drop in averaged values in a region $\pm w$ away from the boundary instead of an expected discontinuous drop at the boundary.

particle level data is performed in three passes. The first pass evaluates the following quantities at each location:

- average density $\rho(x, y)$ using (4.2),
- using (4.1) the average momentum density $\langle \rho() v_x(x, y), \rho() v_y(x, y), \rho() v_z(x, y) \rangle$,
- contact stress $\sigma^C_{ij}(x, y)$ using (4.8),
- lubrication stress $\sigma^L_{ij}(x, y)$ also using (4.8), but substituting the lubrication force between particle for the contact force.

The average velocity can then be evaluated by dividing the average momentum density with the average density. The second pass evaluates the gradient of each velocity component using (4.7). Each particle's fluctuation velocity is calculated using (4.6), after which the third coarsegraining pass calculates the kinetic stress σ^K_{ij} using (4.10).
After coarsegraining the relevant rheological quantities can be constituted. The solids fraction is the ratio of the average density to particle density,

$$\phi = \frac{\rho}{\rho_p} \, . \tag{4.12}$$

The full stress tensor is the sum of contact, viscous and kinetic stresses:

$$\sigma_{ij}(\vec{x}, t) = \sigma^C_{ij}(\vec{x}, t) + \sigma^L_{ij}(\vec{x}, t) + \sigma^K_{ij}(\vec{x}, t) \, . \tag{4.13}$$

The pressure and tangential part of the stress tensor (or sometimes called the shear stress) are extracted from the stress as follows,

$$P = -\frac{1}{3}\sigma_{kk} \quad \text{and} \quad \tau_{ij} = \sigma_{ij} + P\delta_{ij} \ , \tag{4.14}$$

here the Einstein notation is used where the summation over repeated indices is implied. In other words σ_{kk} is short hand for $\sum_k \sigma_{kk}$, which is also the trace of σ_{ij}. The effective friction is the ratio of the norm of the shear stress to the pressure

$$\mu = \frac{|\tau_{ij}|}{P} \ . \tag{4.15}$$

The shear rate is defined as the norm of the deviatoric part of the strain rate tensor. The strain rate tensor is,

$$\dot{\gamma}_{ij}(\vec{x}, t) = \frac{1}{2}\left(\partial_i v_j + \partial_j v_i\right) \ , \tag{4.16}$$

where $\partial_i v_j(\vec{x}, t)$ is the derivative of the j-th component of the velocity vector with the i-th coordinate. These quantities are various components of the gradient of velocities. The deviatoric part is

$$\gamma^d_{ij} = \dot{\gamma}_{ij} - \frac{1}{3}\dot{\gamma}_{kk}\delta_{ij} \ , \tag{4.17}$$

and finally the shear rate is the norm of this expression,

$$\dot{\gamma} = \sqrt{\frac{1}{2}\dot{\gamma}^d_{ij}\dot{\gamma}^d_{ij}} \ . \tag{4.18}$$

The granular temperature can be calculated from the kinetic stress as,

$$T(\vec{x}, t) = \sigma^K_{kk}(\vec{x}, t)/\rho(\vec{x}, t) \ . \tag{4.19}$$

4.2.1 Angles

Cortet et al. [28] compared the angles between the eigenspaces of the shear stress τ_{ij} and the deviatoric part of the strain rate $\dot{\gamma}_{ij}$. Their simulations were carried out in 2D and therefore tensor quantities are represented by 2×2 matrices. The difference between the eigenspaces of two tensors can be described by one angle which represents a rotation in the 2D plane. In 3D the situation is not so straight forward.

The deviatoric stress and strain rate are symmetric matrices and therefore they have real eigenvalues and eigenvectors and can be diagonalised by $AU_A = U_A\Lambda_A$ (see Figure 4.3). The matrix U_A is a map from the regular coordinate system to the eigenspace of A. If the same is true for matrix B, i.e., $BU_B = U_B\Lambda_B$ and U_B is a map to the eigenspace of B. The map $R = U_B U_A^{-1}$ is a map from the eigenspace of

A to the eigenspace of B. R is unitary because both U_A and U_B are unitary, and by Euler's rotation theorem R can be diagonalised to,

$$RU = U \begin{pmatrix} e^{i\theta} & 0 & 0 \\ 0 & e^{-i\theta} & 0 \\ 0 & 0 & \pm 1 \end{pmatrix} , \tag{4.20}$$

where $\theta \in [0, \pi]$ is the angle of rotation. The eigenvector corresponding to the ± 1 eigenvalue is the axis of rotation. When the eigenvector is -1 the map R is related to an improper rotation, or a rotation followed by parity inversion of the axis of rotation. This happens when the handedness of the eigenspace of A and B are not the same. In general, numerical schemes that find the eigenvectors of matrices will list them in a random order. To find the smallest angle that corresponds to a proper rotation, U_A and U_B are constructed with all possible permutations and parity inversions of the eigenvectors of A and B respectively. The matrix R followed by θ can then be calculated and the smallest θ among the permutations is associated with the angular alignment between the eigenspaces of A and B. This procedure is used in Chapter 7 to compare the alignment between the eigenspaces of the shear stress τ_{ij} and the strain rate $\dot{\gamma}_{ij}$.

4.3 Choosing the Smoothing Function

The smoothing function K is usually written as the product of a temporal and spatial smoothing function, $K = G(\vec{x})F(t)$, and each of these are defined in terms of a normalised kernel function.

The spatial smoothing function $G(\vec{x})$ is defined as

$$G(\vec{x}) = |W|^{-1/2} K_x(W^{-1/2}\vec{x}) , \tag{4.21}$$

where K_x is the kernel function and W is a 3×3 symmetric, positive definite matrix – called the bandwidth matrix. Writing G in this general form allows us to choose different smoothing lengths for each direction which is a great advantage when studying the rotating drum in the plane perpendicular to its axis. We are usually interested in the dynamics of the xy-plane in batch rotating drums and for this system the corresponding bandwidth matrix is:

$$W = \begin{bmatrix} w & 0 & 0 \\ 0 & w & 0 \\ 0 & 0 & L/2 \end{bmatrix} \tag{4.22}$$

where w is the smoothing length in the xy-plane, usually of the order of the particle diameter, while smoothing in z-direction is over half the drum length L. The resulting averaging region is ellipsoidal with a circular cross section in the xy-plane

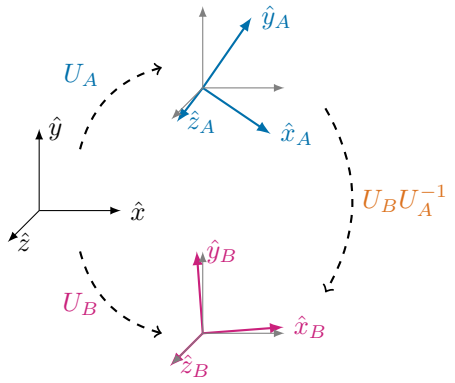

Figure 4.3 – The eigenspace of two matrices A and B are spanned by the eigenvectors $\{\hat{x}_A, \hat{y}_A, \hat{z}_A\}$ and $\{\hat{x}_B, \hat{y}_B, \hat{z}_B\}$. The unitary matrices U_A and U_B are maps from the regular coordinates $\{\hat{x}, \hat{y}, \hat{z}\}$ to the eigenspaces of A and B respectively. $U_B U_A^{-1}$ is a unitary map from the eigenspace of A to that of B and can be diagonalised (according to Euler's rotation theorm) to a rotation matrix $\mathrm{diag}(\exp(i\theta), \exp(-i\theta), \pm 1)$.

and extending the length of the drum in the z-direction. This shape allows the dynamics in a 3D volume to be effectively sampled and project it to a 2D surface.

The temporal smoothing function $F(t)$ is written as

$$F(t) = (1/w_t) K_t(t/w_t), \tag{4.23}$$

The parameter w_t is the smoothing time and defines the time scale over which temporal averages are taken.

Two popular choices for the kernel function are the step and Gaussian functions, shown in Figure 4.4.

4.3.1 The Step Function

Using the normalised step function in three dimensions for the kernel gives:

$$K(\vec{a}) = \frac{3}{4\pi} \mathbf{1}_{\{|\vec{a}| \leq 1\}} = \begin{cases} \frac{3}{4\pi}, & \text{if } |\vec{a}| \leq 1 \\ 0, & \text{otherwise} , \end{cases} \tag{4.24}$$

where $\vec{a}$ is an arbitrary point and $\mathbf{1}_{\{|\vec{a}| \leq 1\}}$ is the indicator function. A single valued version of the step function is visualised in Figure 4.4. The smoothing function becomes

$$G(\vec{x}) = \begin{cases} \frac{3}{4\pi w^2 (L/2)}, & \text{if } \left(\frac{x}{w}\right)^2 + \left(\frac{y}{w}\right)^2 + \left(\frac{z}{L/2}\right)^2 \leq 1 \\ 0, & \text{otherwise} , \end{cases} \tag{4.25}$$

or $1/V_w$ for points inside an ellipsoid with volume $V_w = 4/3\pi w^2 (L/2)$. In this case the sum in the definition for the density in (4.2) only has to be carried out over particles that are within the ellipsoid centred around the probe point and with axes lengths w in the x and y directions and $L/2$ in the z direction. If we denote the set

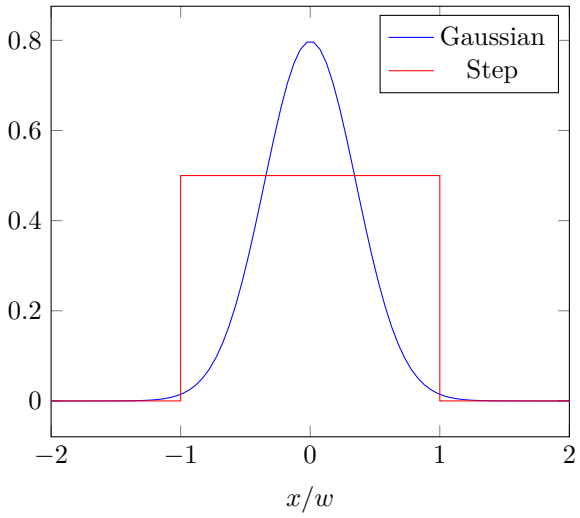

Figure 4.4 – A few kernel functions commonly used with the coarsegraining method.

of particles for which this condition is true by P' and the number of particles therein by $N_{P'}$, the average density is given by

$$\rho(\vec{x}) = \sum_{p \in P'} \frac{1}{V_w} m \mathrm{m}_p = \frac{N_{P'} m_p}{V_w} \,. \tag{4.26}$$

The spatial average of some quantity ψ is given by

$$\rho(\vec{x})\psi(\vec{x}) = \sum_{p \in P'} \frac{1}{V_w} m_p \psi_p = \frac{m_p}{V_w} \sum_{p \in P'} \psi_p \,. \tag{4.27}$$

By combining this with the expression for the average density in (4.26), we find that the average particle property is given by the mean of that property of all the particles near the probe point:

$$\psi(\vec{x}) = \frac{1}{N_{P'}} \sum_{p \in P'} \psi_p \,. \tag{4.28}$$

This approach is easy to implement, makes the most intuitive sense and has been used in some form or another in many other studies (cf. Ness and Sun [46], Rycroft et al. [50], and Lätzel et al. [128]). One disadvantage is that it is no longer possible to evaluate the gradient using the method proposed in (4.7), because the step function is not differentiable. Another complication is that the solids fraction is not easy to calculate, because particles may overlap with the boundary of the step. To calculate the solids fraction accurately, the fraction of the particle that lies outside the step needs to be excluded.

4.3.2 Gaussian smoothing

Another popular option for the kernel function is the Gaussian

$$K(\vec{a}) = \pi^{-3/2} \exp(-|\vec{a}|^2) \ . \tag{4.29}$$

The corresponding smoothing function becomes

$$G(\vec{x}) = \frac{1}{\pi^{3/2} w^2 (L/2)} \exp\left(-(x/w)^2\right) \exp\left(-(y/w)^2\right) \exp\left(-(2z/L)^2\right) \ . \tag{4.30}$$

A single valued version of the Gaussian is shown in Figure 4.4.

The Gaussian is differentiable and therefore allows us to calculate the gradient of average quantities using (4.7), with

$$\nabla G(\vec{x}) = -\left\langle \frac{2x}{w^2}, \frac{2y}{w^2}, \frac{2z}{(L/2)^2} \right\rangle G(\vec{x}) \ . \tag{4.31}$$

4.3.3 Temporal Smoothing Function

The step function is most often used as the temporal smoothing function. This allows one to make equal use of data over the entire course of the experiment. With the step function as kernel, the temporal smoothing is an unweighted average over all time steps.

In some cases it is useful to use the Gaussian for temporal smoothing. This is done to answer questions relating to how long a simulation or experiment has to be carried out in order to collect sufficient data for statistical analysis. These questions can be answered because the Gaussian introduces a smoothing time parameter w_t. A larger smoothing time will incorporate more data into the average and it is possible to determine when sufficient data is recorded by varying this parameter on a long duration simulation. This technique will be used in the next chapter.

4.3.4 Comparisons

This section compares different choices for coarsegraining parameters on data from Chapter 3. In Figure 4.6 and Figure 4.7 different choices for the spatial smoothing function and averaging interval are used to calculate the solids fraction and x-component of the velocity, respectively. The solids fraction is more sensitive to the choice of kernel function and smoothing radius than the velocity. The Gaussian produces smoother results than the step function and in general increasing the averaging width reduces noise.

Figure 4.5 shows the difference between using equation (4.7) and a finite difference scheme to calculate the gradient. A finite difference method was used to calculate the gradient of the average velocity using,

$$\partial_y v_x = \frac{\partial v_x}{\partial y} \approx \frac{v_x(\langle x, y + \Delta y \rangle, t) + v_x(\langle x, y \rangle, t)}{\Delta y} \ , \tag{4.32}$$

where Δx is the distance in the x direction between adjacent probe points. In this particular DEM simulation, particles near $y = 0$ are given a set velocity $\vec{v} = \langle -7.5, 0, 0 \rangle$ and particles near $y = 15$ have $\vec{v} = \langle 7.5, 0, 0 \rangle$. After steady state is reached, a linear velocity profile $v(x, y) = (x, 0)$ is expected and a constant gradient with only one non-zero component $\partial_y v_x = 1$. Significant correlation between the two methods is observed, but the gradient method has a the following advantages: The gradient method requires only one evaluation of equation (4.7), while the finite difference method requires two evaluations each of equations (4.1) and (4.2) at locations separated by Δy. The second and more important advantage is that numerical noise is reduced, which tends to arise in non-linear systems.

4.4 Extension to PEPT data

The above method can be used for Positron Emission Particle Tracking (PEPT) data too. Wildmann et al. [32] argues that if a single particle is tracked for a sufficiently long time the experimenter will record all the possible dynamics of the particles. In that case each term in the sum over the particles of (4.2) will make an equal contribution to the result. One can then replace the summation over particles by a factor of the number of particles and all that remains in the integral over time of the history of the tracer particle. This is the so called ergodic hypothesis which can be expressed in mathematical terms as,

$$\rho(x,t) \approx N \int dt' m_T K(x - x_T, t - t_T) \,, \tag{4.33}$$

$$\rho(x,t)\psi(x,t) \approx N \int dt' m_T \psi_T K(x - x_T, t - t_T) \,, \tag{4.34}$$

where x_T is the position of the tracer at time t_T and ψ_T is a particle property.

A key question that arises is how long the dynamics of the tracer particle needs to be recorded for so that the approximation in equation (4.34) is accurate enough. This question is the topic of the next chapter.

Figure 4.8 compares the gradient calculated using a finite difference scheme in (a) and the method proposed in equation (4.7). The noise present in (a) is reduced significantly by using a method that does not require evaluating the velocity in two different positions.

4.5 Discussion

This chapter presented the method for coarsegraining discrete particle level data from DEM simulations and PEPT experiments to continuum fields. The continuum fields provides a description of the bulk material in terms of average velocity, solids fraction, strain rate and internal forces which in turn is used as the building blocks for rheological models of dense granular flow and dense suspensions. The method presented here is used in later chapters to make comparisons between the simulations

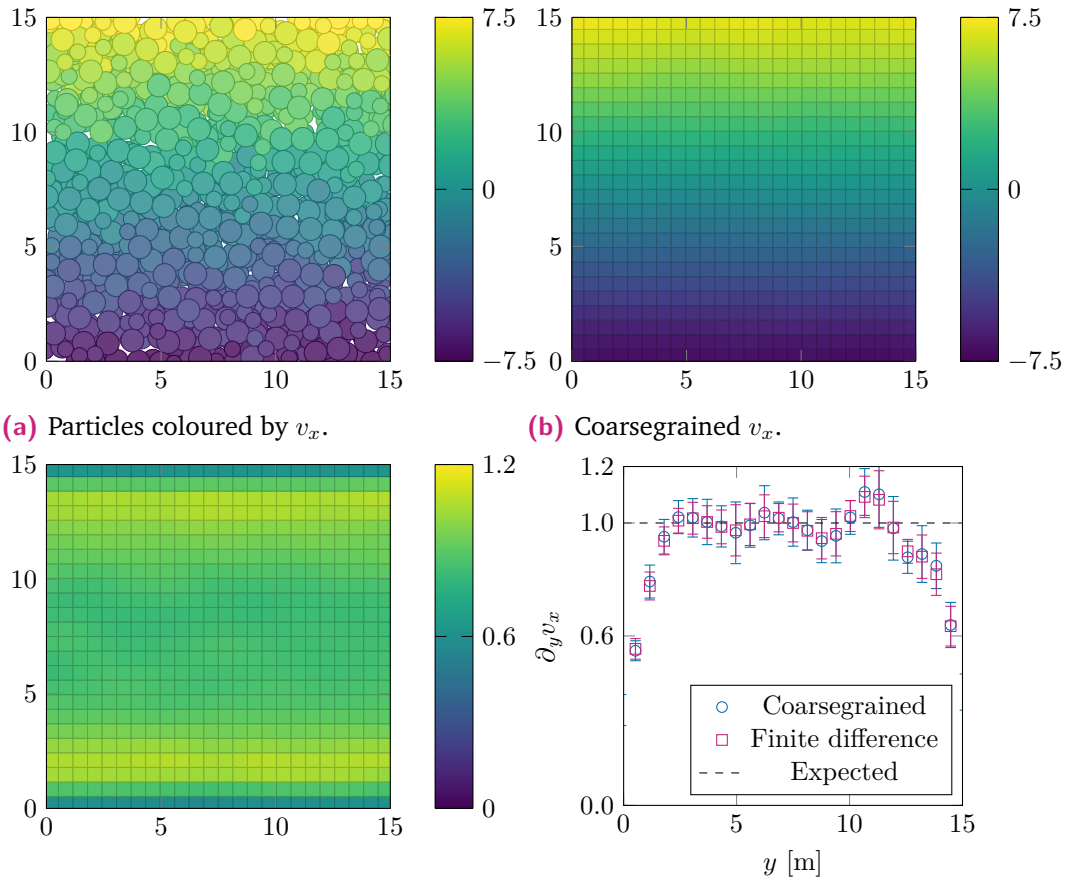

(a) Particles coloured by v_x.

(b) Coarsegrained v_x.

(c) Coarsegrained gradient ($\partial_y v_x$).

(d) Gradient ($\partial_y v_x$) profile.

Figure 4.5 – For a simple shear simulation with x component of the velocity set to $v_x(y = 0) = -7.5$ and $v_x(y = 15) = 7.5$ (a) individual particles coloured according to v_x (b) the coarsegrained velocity component v_x (c) the coarsegrained gradient $\partial_y v_x$ (d) compares the gradient calculated using (4.7) to a finite difference scheme and the expected velocity profile at steady state.

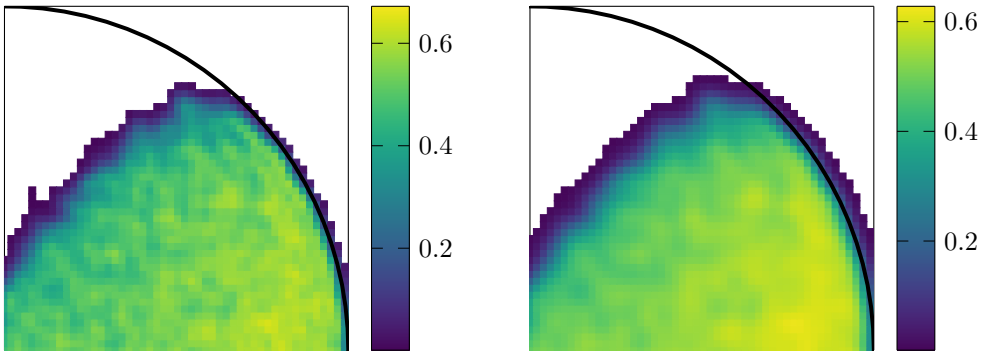

(a) Gaussian smoothing, $w = d_p$

(b) Gaussian smoothing, $w = 1.5d_p$

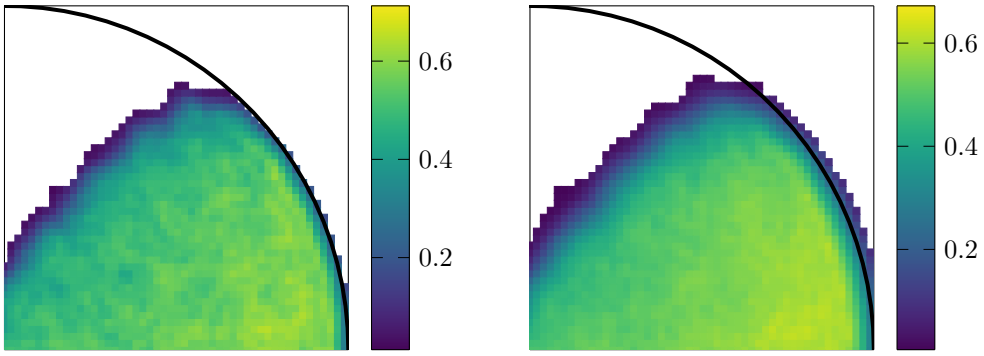

(c) Step kernel, $w = d_p$

(d) Step kernel, $w = 1.5d_p$

Figure 4.6 – Solids fraction ($\phi(x,t) = \rho(x,t)/\rho_p$) using the Gaussian and step function, and different averaging radii. A larger averaging radius yields a smoother solids fraction (comparing (a) to (b) and (c) to (d)), while the Gaussian gives a smoother solids fraction than the step function (comparing (a) to (c) and (b) to (d)).

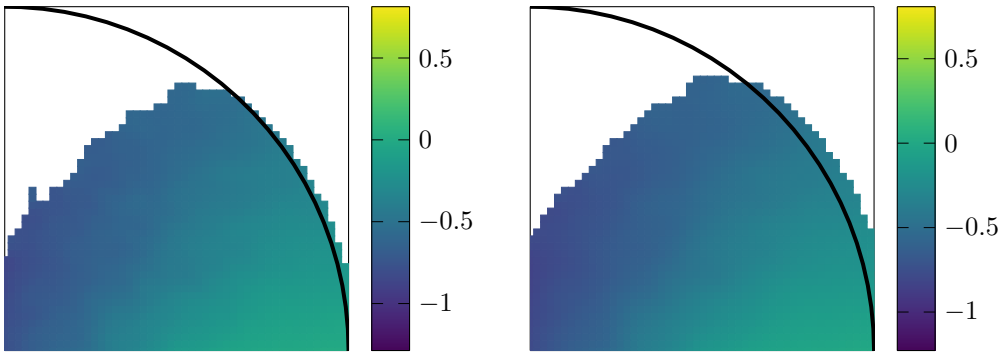

(a) Gaussian smoothing, $w = d_p$

(b) Gaussian smoothing, $w = 1.5d_p$

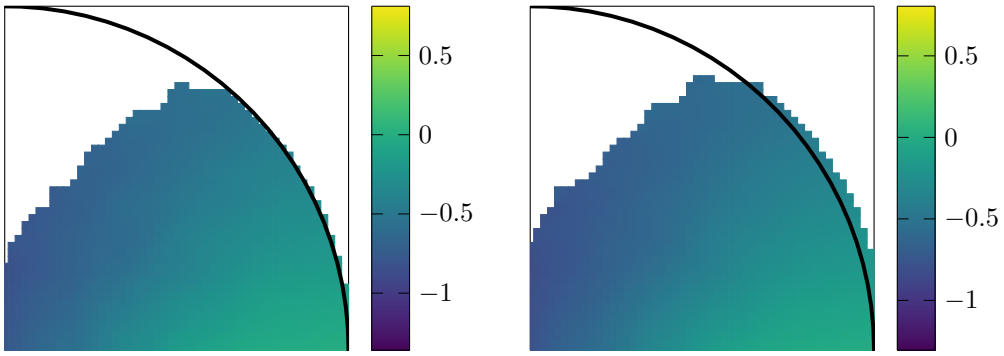

(c) Step kernel, $w = d_p$

(d) Step kernel, $w = 1.5d_p$

Figure 4.7 – Velocity component (v_x) using the Gaussian and step function, and different smoothing radii. In comparison to Figure 4.6, the velocity calculation is less sensitive to these choices than the solids fraction; giving similar results in each case.

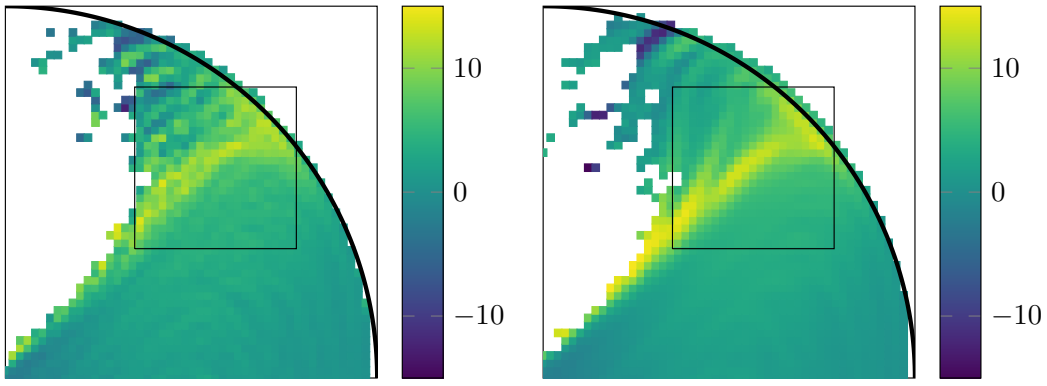

(a)

(b)

Figure 4.8 – Gradient using (a) the finite difference method, and (b) equation (4.7) for Positron Emission Particle Tracking (PEPT). The gradient is noticeably smoother using the latter method, which apparent in the indicated region.

and experiments, and between results from simulations in Chapter 3 to rheological models described in Chapter 2.

The coarsegraining method discussed is very general and can be specialised by making different choices for the kernel function. The step function is a popular choice; this turns the coarsegraining to a voxel based methods where averages are taken over all particles that fall inside a box. However, using a Gaussian kernel has several advantages over a step function, the most notable is that the solids fraction can be calculated directly from the average density without having to calculate fractions of particles that fall outside a box. Further, because the Gaussian is differentiable, gradients of quantities such as the velocity can be calculated using equation (4.7).

In non-linear flows the full tensorial quantities need to be evaluated. The method presented in this chapter allows for the stress and strain rate tensors to be calculated. Additionally, a method for calculating the angle between the principle directions of two tensors was discussed.

There are additional considerations when extending the method to PEPT data. The ergodic hypothesis is employed (as expressed in equation (4.34)) to calculate the solids fraction, average velocity and strain rate when the position and velocity for only one particle is known. The ergodic hypothesis allows for direct comparisons to be made between results from PEPT and DEM using the same mathematical framework. In particular this approach allows the Stokes number – a key parameter that characterises flow regimes in viscous granular suspensions – to can be calculated and compared between simulations and experiments.

The ergodic hypothesis is investigated in Chapter 6 and Chapter 7 compares DEM results to PEPT results and rheological models.

5 Experimental Studies

To capture the effect of a fluid acting on particles, Trulsson et al. [6] and Seto et al. [45] applied lubrication and drag forces to particles in Discrete Element Method (DEM) simulations. However, Ness and Sun [46] found that the lubrication force dominated over other fluid forces. In addition, before a drag force can be applied to particles, a model for the fluid velocity is required which is not readily available in rotating drum flows. The need to apply all of the above forces in a DEM simulation can be evaluated by making comparisons between numerical and experimental results.

Positron Emission Particle Tracking (PEPT) as an experimental technique was introduced in Section 2.3. This chapter discusses the experiments carried out for this thesis using the PEPT technique. The processing of raw line data, recorded by the acquisition system, to particle positions is discussed as well as torque and viscosity measurements taken. To test the ergodic hypothesis, a series of experiments were performed where a tracer particle was tracked over a $10\,\mathrm{h}$ period. A second set of experiments were carried out using a rotating drum filled with spherical glass beads and a mixture of water and glycerol, to test the lubrication approximation. The ratio of water to glycerol was varied to modify the viscosity of the fluid. The data recorded in these experiments allow for comparisons to be made with the DEM simulations performed using the lubrication approximation (discussed in the Chapter 3).

5.1 Positron Emission Particle Tracking (PEPT)

Positron Emission Particle Tracking (PEPT) experiments for this work were performed at the PEPT Cape Town facility, located at the South African national accelerator center, iThemba Laboratory for Accelerator Based Science (iThemba LABS). The EXACT3D (Model: CTI/Siemens 966) Positron Emission Tomography (PET) scanner, shown in Figure 5.1 was used in this work. It has $36 \times 12 \times 8 \times 8$ bismuth germinate detector elements arranged in a cylinder that gives a usable field of view with diameter of approximately $50\,\mathrm{cm}$ and depth $20\,\mathrm{cm}$. The acquisition system is able to record up to 10 events per millisecond.

In this work the PEPT tracer is prepared by adsorbing ^{68}Ga onto an ion exchange resin which is then embedded in a glass bead. ^{68}Ga was used because its half-life (of $68\,\mathrm{min}$) is long enough so that data can be captured during an experiment and short enough so that the tracer poses a minimal risk of radioactive contamination in the event that the glass bead breaks apart.

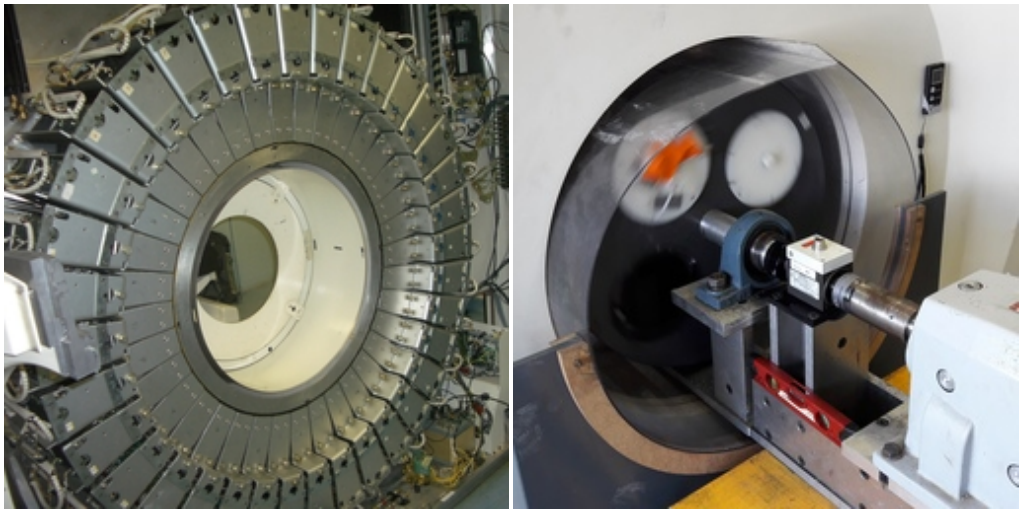

(a) (b)

Figure 5.1 – (a) The EXACT3D (Model: CTI/Siemens 966) Positron Emission Tomography (PET) scanner showing the detector buckets and (b) the lab scale rotating drum used in this study (right).

5.2 The Rotating Drum Configuration

A lab scale rotating drum was constructed from a high density polyethylene pipe with inner diameter $23\,\mathrm{cm}$ and length $20\,\mathrm{cm}$. The side walls of the drum were closed off with disks and 4 circular ports were added to one side wall to allow access to the inside of the drum for the purpose of introducing the charge particles. A small port is also available to easily insert the tracer and a thermocouple without disturbing the position of the drum. The inside of the drum was coated with a rubber lining to increase the friction between the inner drum wall and the charge. The drum was connected to an electrical motor, via a shaft, which was powered by a variable-frequency drive. A torque sensor was included in the drive system so that power draw measurements could be taken. This setup allows the experimenter to easily change the rotational speed of the drum and record the torque applied to the drum.

A typical PEPT session consists of positioning the drum in the scanner, placing a temporary tracer on the outside of the drum and recording its position for $2\,\mathrm{min}$. The resulting circular track is used to determine the orientation of the drum inside the scanner and transform the subsequent tracer's position from the scanner's reference frame to the drum's reference frame. The PEPT tracer is prepared with activity of about $1500\,\mu\mathrm{Ci}$ and placed inside the drum, while the acquisition system is allowed to record lines in $20\,\mathrm{min}$ intervals. The $20\,\mathrm{min}$ time limit on these intervals is necessitated by file size limits of the acquisition system. Typically 6 to 8 (depending on the tracer's initial activity) such intervals can be recorded per tracer after which activity levels drop too low for usable data to be recorded. The tracer's activity is gauged by the file size on the acquisition system's hard drive, which is directly related

to the number of lines recorded. When too few lines are recorded, the triangulation method used to locate the tracer fails to produce accurate positions for the tracer.

5.2.1 Ergodic Dataset

This dataset is used to investigate questions about how long a single particle needs to be tracked before one can infer information about the statistical properties of the bulk material based on that of the tracked particle. Results from these experiments are used in Chapter 6. This is important because the experiments can only track one particle at a time and needs to be carried out for long enough so that the time average of that one particle is representative of the ensemble.

The drum's rotational speed was set to $36.8\,\mathrm{RPM}$ which is equivalent to a Froude number $F_r = 0.360$ or $\omega = 60\,\%$ of the drum's critical speed. The drum's volume was filled to $40\,\%$ with mono sized glass beads and three particle diameters, $d = \{5, 8, 10\}\mathrm{mm}$, were used in different runs. A total of $20\,\mathrm{h}$ tracking time was recorded for each of the three particle sizes.

No fluid was added to the drum for this experimental data set.

5.2.2 Viscous Dataset

This data set was recorded to test the dynamics of granular suspensions against DEM simulations. These simulations were carried out with an additional lubrication force to capture the effect of a liquid between the particles. Previous work by Govender et al. [27] suggests that the shear rate in the flowing layer would be $\dot{\gamma} \approx 20\,\mathrm{s}^{-1}$. A mixture of water and glycerol were chosen as the liquid because fluids of different viscosities can be readily prepared by changing the ratio of water-to-glycerol. Ratios of water-to-glycerol was chosen to cover a wide range of Stokes numbers (S_t), starting from the inertial regime and approaching the viscous regime, $S_t \to 1$. This can be achieved by using a fluid with higher viscosities or glycerol/water mixtures with a higher ratio of glycerol-to-water.

The drum was filled to 50% of its volume with mono-sized $d = 10\,\mathrm{mm}$ glass beads. The viscosity was calculated using the parametrisation by Cheng [129] and, for confirmation, the viscosity of samples was measured using a viscometer. The viscosity measurements are discussed in Section 5.4.2. The drum speed was varied between the 7 angular velocities displayed in Table 5.1. Temperature readings were taken between each $20\,\mathrm{min}$ run. On average a $1\,^{\circ}\mathrm{C}$ increase in temperature was recorded between each $20\,\mathrm{min}$ interval of running, which gave rise to a viscosity that varied over the course of the experiment.

5.3 Data Processing

After Lines of Response (LORs) are recorded, several processing steps are performed to determine the position and velocity of the tracer at various times. A triangulation technique is used that takes as input a number of LORs and calculates the position of tracer. This time series is not yet suitable to be used in further analysis and

Table 5.1 – Left: the drum speeds for the Viscous dataset as a faction of the critical speed, angular velocity, revolutions per minute and Froude number. The critical speed for the drum used in this study is $\omega_c = 6.35\,\mathrm{rad\,s^{-1}} = 62.3\,\mathrm{RPM}$. Right: Fluid mixtures used together with each of the drum speeds in the table on the left. The viscosity of a mixture was calculated using Cheng [129]. Variation in the viscosity reflects how the temperature of the fluid changed over the course of the experiment.

ω/ω_c	$\omega[\mathrm{rad\,s^{-1}}]$	RPM	F_r
0.30	1.96	18.7	0.090
0.35	2.28	21.8	0.123
0.40	2.61	24.9	0.160
0.45	2.94	28.1	0.203
0.50	3.26	31.2	0.250
0.55	3.59	34.3	0.303
0.60	3.92	37.4	0.360

Water % w/w	Glycerol % w/w	Viscosity Pa s
40	60	0.011 ± 0.001
25	75	0.038 ± 0.005
10	90	0.25 ± 0.04

some extra processing steps are needed to account for the following facts. Firstly, because of the random nature of radioactive decay, positrons are produced at an irregular interval and, therefore, the time gap between measured LORs are not equal. Furthermore, the average time gap tends to increase on average as the tracer ages over the course of an experiment. This can be seen in Figure 5.2, where the number of events in $1\,\mathrm{min}$ intervals is erratic from one minute to the next, but follows the radioactive decay (proportional to $\exp(-t/t_{1/2})$ with the half-life of ^{68}Ga $t_{1/2} = 68\,\mathrm{min}$) over longer periods. Secondly, the scanner's geometry places limitations on how likely it is for a pair of γ-rays to be recorded and this likelihood depends on the tracer's position in the camera. If not enough LORs are recorded in a short enough time span, it is unlikely that the triangulation method will be able to resolve the tracer's position. This will result in large time steps in the tracer's position and they need to be identified before the tracer's velocity is calculated.

This section discusses the procedure used to convert the LORs recorded by the PET scanner to a suitable representation of the particle's position vs. time.

5.3.1 Triangulation

The triangulation routine by Parker et al. [31] is used to assign a three dimensional position and time stamp to a set of LORs. This position is identified as the tracer's position at the particular time stamp. The LORs are partitioned into sets of $N \sim 100$ sequential lines called $S = \{L_1, \ldots, L_N\}$. Each of these sets are assigned a 3D coordinate (m_S) that minimises the perpendicular distance between m_s and each of the lines in S.

If the distance between the i-th line and a point m is given by the function δ_i, the mean distance between a point m and each of the lines in S is given by

$$d(S) = \frac{1}{N(S)} \sum_{i}^{N} \delta_i(m) \,, \tag{5.1}$$

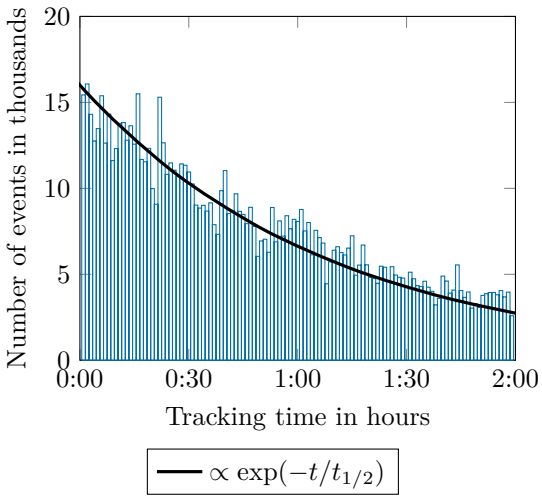

Figure 5.2 – Number of events in $1\,\mathrm{min}$ time intervals, showing exponential decay of of the ^{68}Ga tracer's activity with half-life $t_{1/2} = 68\,\mathrm{min}$. After about $2\,\mathrm{hours}$ the number of events recorded by the Positron Emission Tomography (PET) scanner is too low to resolve the tracer's position.

where $N(S)$ is the number of lines in S. In particular, there exists an analytical expression for m_S and the corresponding $\delta_i(m)$ [31].

The algorithm takes into account that some of the lines will be corrupted. This can happen when one or more of the γ-rays undergo Compton scattering with matter between the annihilation event and the detector or if the two γ-rays do not correspond to the same annihilation event. The image on the left of Figure 2.2 shows the xy projection of a sample set of LORs. Most of the lines pass through a common point, however some corrupted lines can be seen.

The triangulation algorithm creates a new set of lines that contain all the lines in S except for the one for which $\delta(m_s)$ is largest. This procedure is repeated until a specified fraction of the lines remain, $f_{\mathrm{opt}}N$ with $0 < f_{\mathrm{opt}} < 1$. After the required number of lines have been discarded, the tracer's position is identified with the minimum point of the final set m_S.

The precision of locating a stationary PEPT tracer is given by $\delta = w/\sqrt{f_{\mathrm{opt}}N}$, where w is the spatial resolution of the PET scanner, as defined by Bridgwater et al. [130] and Fan et al. [131]. One can therefore increase the precision by using more lines in the triangulation process. However, when the particle is moving, there will be an uncertainty associated with its position. Therefore there exists an optimal N. If N is too large the tracer will move very far during the time frame that the lines were recorded, and too small will give insufficient precision. In previous work where the tracer's position was known (either held in a fixed location [31] or moved in a predictable manner [100]) the triangulation parameters N and f_{opt} are chosen to minimize the uncertainty between the measured and expected position of the tracer. In this work beads with diameter $5\,\mathrm{mm}$ to $10\,\mathrm{mm}$ were used and uncertainties much smaller than that are easily achieved with the Siemens EXACT3D camera [100]. To

ensure the maximum tracking time, the triangulation parameters were chosen so that the least amount of positions were discarded.

5.3.2 Considerations due to the scanner's field of view

The geometry of the scanner places restrictions on the probability that two back to back γ-rays will be recorded to produce a LOR. When this is taken into account together with the triangulation technique outlined above, it is possible that the tracer's position cannot be calculated when it spends time in a region where γ-rays are unlikely to be recorded. This is because the time between the first and last LOR in the set of N will increase, therefore the tracer would have covered a greater distance and the uncertainty associated with the position will be larger.

For a cylindrical detector, like the one used in this study, such regions occur near the ends of the cylindrical ring of detector elements. To illustrate why this happens, consider the tracer's position at $\vec{r}_T = \langle r_T \cos\theta_T, r_T \sin\theta_T, z_T\rangle$ relative to the centre of the detector ring. A position on a potential LOR is given by (see Figure 5.3)

$$\begin{aligned}\vec{r} &= \vec{r}_T + s\langle \sin\phi\cos\theta, \sin\phi\sin\theta, \cos\phi\rangle \\ &= \langle r_T\cos\theta_T, r_T\sin\theta_T, z_T\rangle + s\langle \sin\phi\cos\theta, \sin\phi\sin\theta, \cos\phi\rangle \ , \end{aligned} \tag{5.2}$$

with s a parameter along the LOR, allowed to be negative. The distance from the tracer is $|s|$. The angles $\theta \in [0, 2\pi]$ and $\phi \in [0, \pi/2]$ are the polar and azimuthal directions of the LOR, respectively. The path of the γ-rays must intersect the cylinder while the axial distance between the intersection and the center of the camera is less than half of its axial field of view. These constraints can be expressed as $r = R$ while $z_t + s\cos\theta \leq L/2$. Using (5.2), the first condition implies that

$$(r_T\cos\theta_T + s\sin\phi\cos\theta)^2 + (r_T\sin\theta_T + s\sin\phi\sin\theta)^2 = R^2 \ , \tag{5.3}$$

which simplifies to the following quadratic equation in $s\sin\phi$:

$$s^2\sin^2\phi + 2r_T\cos(\theta - \theta_T)\, s\sin\phi + r_T^2 - R^2 = 0 \ . \tag{5.4}$$

The roots of the quadratic equation are given by,

$$s\sin\phi_\pm = -r_T\cos(\theta-\theta_T) \pm \sqrt{(r_T)^2\cos^2(\theta-\theta_T) + R^2 - r_T^2} \tag{5.5}$$

$$= -r_T\cos(\theta-\theta_T) \pm \sqrt{(r_T)^2\sin^2(\theta-\theta_T) + R^2} \ . \tag{5.6}$$

A potential LOR will hit the furthest most ring of detector elements when

$$z_T + s\cos\phi = L/2 \quad \Rightarrow \quad s = \frac{L/2 - z_T}{\cos\phi} \ , \tag{5.7}$$

and substituting this into (5.6) yields:

$$\tan\phi_{\pm} = \frac{R}{L/2}\frac{1}{1-2z_T/L}\times \left(-\frac{r_T}{R}\cos\left(\theta-\theta_T\right) \pm \sqrt{\left(\frac{r_T}{R}\right)^2 \sin^2\left(\theta-\theta_T\right)+1}\right) . \tag{5.8}$$

This expression relates the azimuthal and polar angles of two back to back γ-rays that are emitted from a tracer located at $\vec{r}_T$ and reaches the detector at the furthest ring of detector elements. There are two critical angles which classify the paths of the γ-rays into three groups:

- When $0 \leq \phi \leq \phi_-$ neither of the γ-rays pass through the detector.
- When $\phi_- \leq \phi \leq \phi_+$ only one of the γ-rays pass through the detector.
- When $\phi_+ \leq \phi \leq \pi/2$ both γ-rays pass through the detector.

Only γ-rays in the last group can be detected by the scanner and result in LORs. The fraction of γ-rays in this category is given by

$$\begin{aligned} P_r(r_t, z_t) &= \frac{1}{\pi^2}\int_0^{2\pi} d\theta \int_{\phi_+}^{\pi/2} d\phi \\ &= \frac{1}{\pi^2}\int_0^{2\pi} d\theta \left(\frac{\pi}{2} - \tan^{-1}\left[\frac{R}{L/2}\frac{1}{1-2z_T/L}\times \left(-\frac{r_T}{R}\cos\theta + \sqrt{\left(\frac{r_T}{R}\right)^2\sin^2\theta+1}\right)\right]\right) . \end{aligned} \tag{5.9}$$

The integral can be evaluated numerically. For the scanner used in this study $2R/L \approx 2.53$ and the resulting P_r is shown in Figure 5.3(b). The dependence on the axial direction (z_T/L) is more significant than the radial dependence (r_T/R). The reduced sensitivity results in less LORs recorded when the tracer is near the edge of the detector than when it is closer to the midpoint of the cylinder. This leads to larger time steps between tracer locations near the edge of the scanner's field of view. This becomes important when taking derivatives in order to avoid unrealistic velocities and accelerations.

The first step in the analysis, after the triangulation has calculated the tracer's position, is to identify when the tracer has left the scanner's field of view. This is achieved by looking for time steps between subsequent positions that are much larger than the average time step between them. This divides the data points into segments where the tracer's position is known.

5.3.3 Smoothing

The following steps are performed on each of the segments identified by the process discussed in the previous section. An interpolation routine is used to find a set of

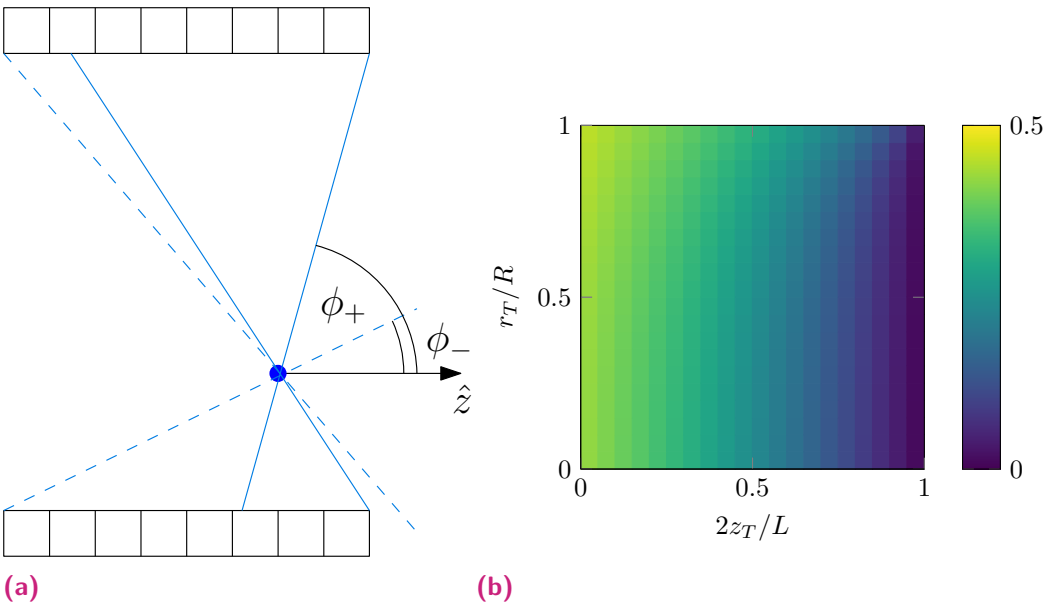

Figure 5.3 – The scanner's resolution is constrained by its geometry. (a) A possible tracer location with Lines of Response (LORs) where both γ-rays will pass through the dectector ($\phi_+ \leq \phi \leq \pi/2$), and only one γ-ray will pass through the dectector ($\phi_- < \phi \leq \phi_+$). (b) The fraction of LORs for which both γ-rays pass through the detector for the EXACT3D Positron Emission Tomography (PET) scanner as a function of the tracer's axial and radial position in the camera.

points that are representative of the measured ones, but at equal time spacing. This means that the number of points in a certain spatial area is proportional to the time it spent there (see Figure 5.4).

After interpolating, a smoothing routine is used to filter out high frequency noise from the position-time data. Noise is amplified when calculating the tracer's velocity (as discussed in Chartrand [132]), however if the smoothing method is too aggressive valuable information about turbulence may be lost. Taking these factors into consideration, a 3^{rd} order Butterworth filter with the cut off frequency 30 times more than the drum's rotation speed is used. Figure 5.5 shows the frequency response of the low pass filter as well as the tracer's position before and after filtering. The erratic motion of the tracer is removed while the general behaviour of the tracer is preserved and suggests that enough information is retained for the purposes of this thesis.

After the tracer's position is determined, a coarsegraining routine is used to calculate ensemble averages of the bulk material. Figure 5.6 shows the average speed of the charge for the viscous data set. The S-shape of the free surface becomes more exaggerated with increased drum speed while spatial variations are damped with increased fluid viscosity. The lower viscosities have a similar appearance with the corresponding DEM results in Figure 3.4, but the shape of the free surface of the highest viscosity changes significantly. This could be because no lubrication forces were applied to particle-wall interactions, or indicate that other fluid effects, such as drag, can no longer be ignored.

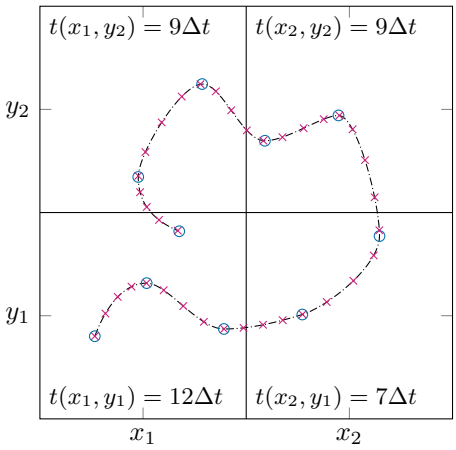

Figure 5.4 – To calculate the time fraction $t(x, y)$ from Positron Emission Particle Tracking (PEPT) data points (○), a line (- - -) is fitted and re-sampled (×) with equal time steps (Δt). The time the tracer spends in a volume element is then equal to the number of re-sampled points multiplied by the time step or $t(x, y) = N(x, y)\Delta t$.

5.4 Accompanying Measurements

Several additional measurements can be taken along with the PEPT tracer's position that are useful to compliment further analysis.

5.4.1 Torque

The torque applied to the drum is related the power draw. In order to rotate the drum from angle θ_1 to θ_2, the motor must do mechanical work, W, by applying a torque τ. At steady state, the motor will exert a constant torque on the drum, which will have a constant angular velocity ω. The power draw of the drum is the rate of change of the mechanical work exerted on the drum. These quantities are related to each other by

$$P = \frac{dW}{dt} = \frac{d}{dt}\left(\int_{\theta_1}^{\theta_2} d\theta\tau\right) = \tau\omega \ . \tag{5.10}$$

In this thesis torque measurements were taken with a torque sensor connected between the motor and drum. The sensor records a voltage that is proportional to the torque applied through its axis. The voltage signal is amplified, digitized using a digital to analog converter (DAC) and recorded on a personal computer using some software.

Since the sensor emits a voltage, a set of calibration readings needs to be taken so that the measured voltage can readily be converted to the corresponding torque value. Calibration was performed by attaching a horizontal shaft perpendicular to the axis of the sensor. The shaft had indentations at $50\,\mathrm{mm}$ intervals, with the first indentation $22.5\,\mathrm{mm}$ from the center of the shaft. Three weights with mass $m_1 = 0.570\,22\,\mathrm{kg}$, $m_2 = 5.480\,\mathrm{kg}$ and $m_3 = 1.172\,\mathrm{kg}$ were each placed at the second, third and fourth indentation, resulting in 9 torque readings. The weights were allowed to hang freely while the shaft was kept stationary in a horizontal

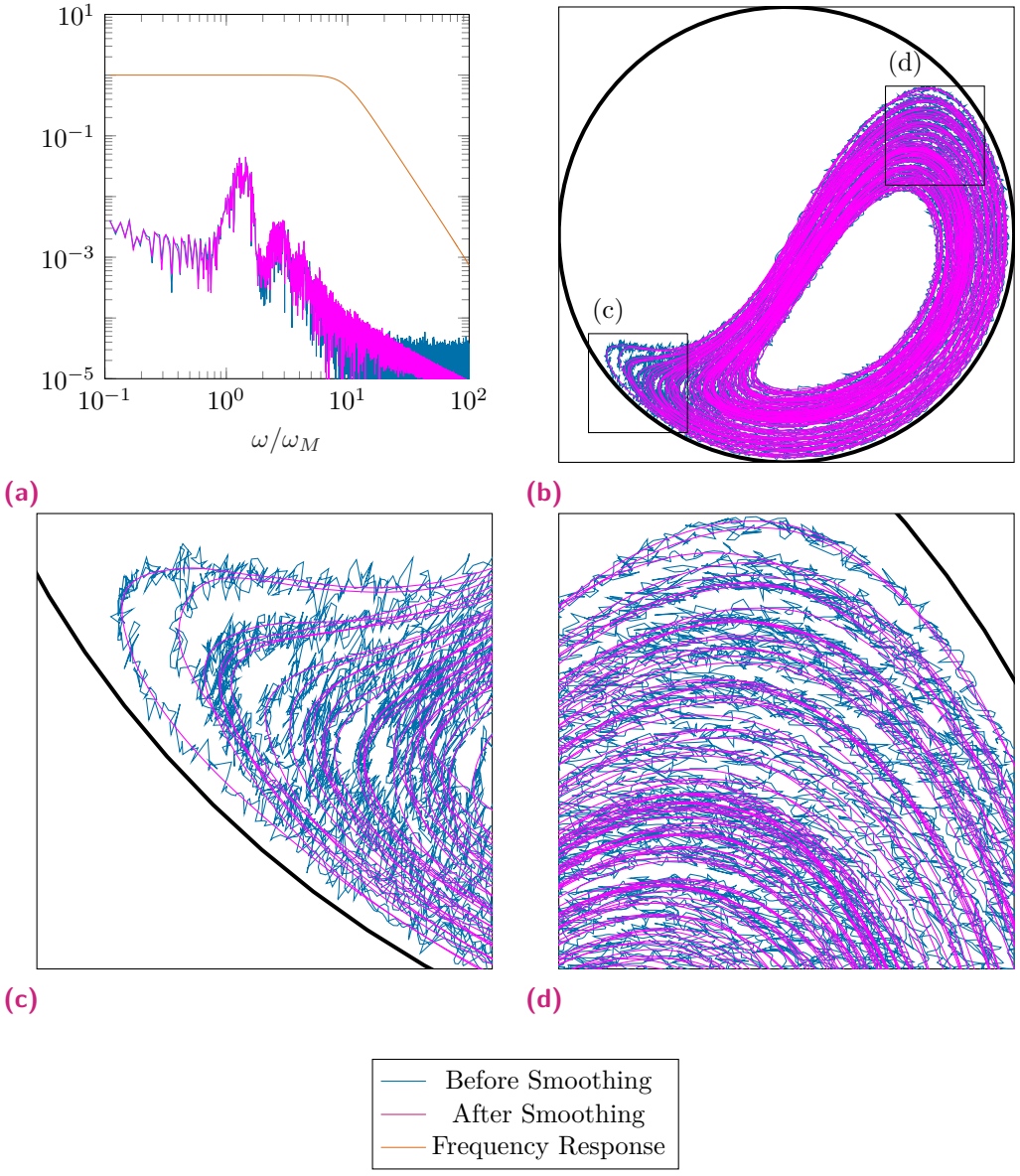

Figure 5.5 – Noise removal using a low-pass filter: (a) shows the Fourier transform of the x-component of data points before and after the low-pass filter has been applied as well as the frequency response of the filter. Frequencies are scaled by the rotational speed of the drum, ω_M. (b) shows the xy-projection of the tracer's position before and after filtering. Detail of the indicated regions are shown in (c) and (d).

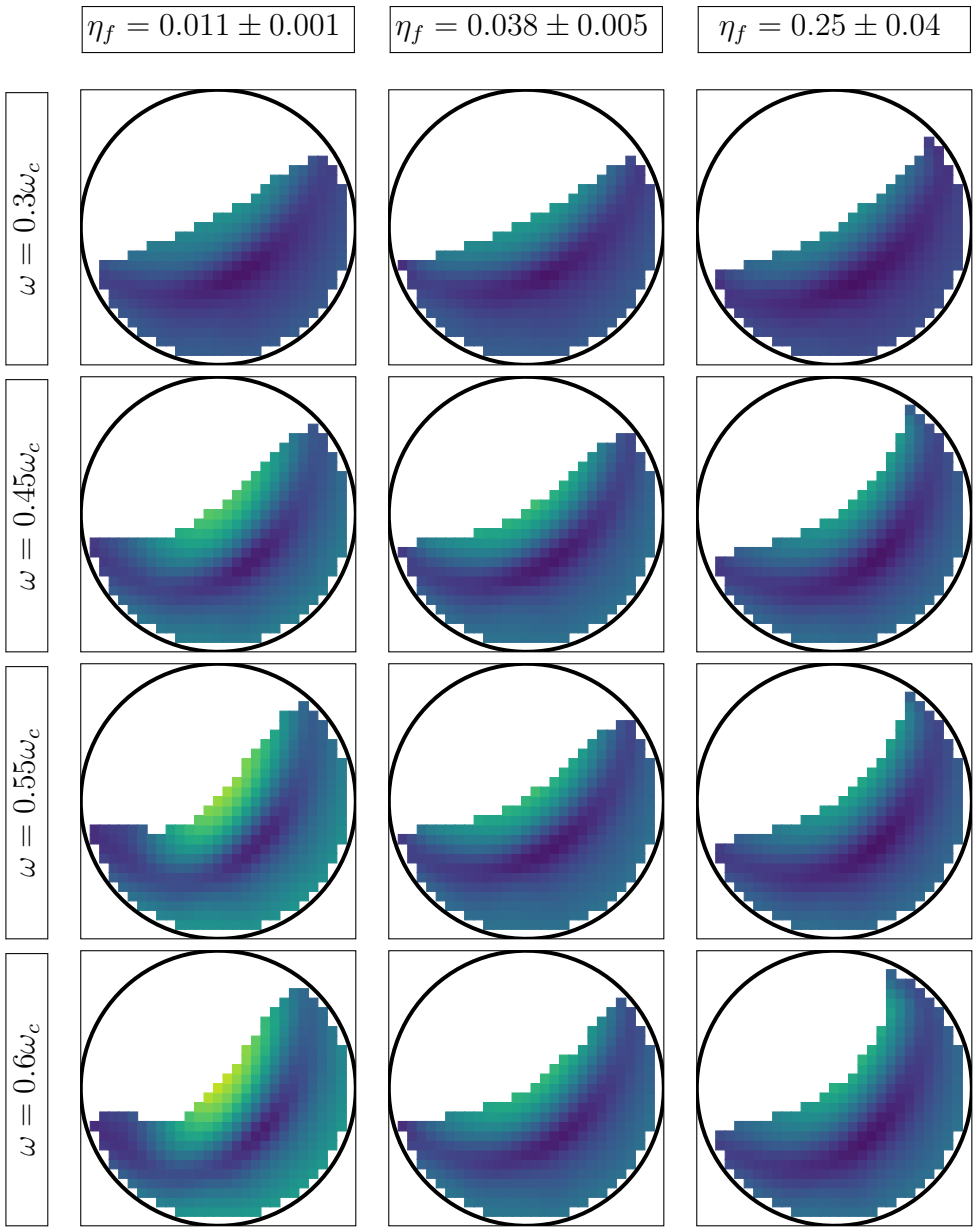

Figure 5.6 – The average speed of the charge for the viscous data set. The first, second and third column corresponds to viscosity $0.011 \pm 0.001\,\mathrm{Pa\,s}$, $0.038 \pm 0.005\,\mathrm{Pa\,s}$ and $0.25 \pm 0.04\,\mathrm{Pa\,s}$, respectively.

position. Under the force of gravity, the applied torque is $\tau = mgr$, where g is the acceleration due to the Earth's gravitational force and r the distance between an indentation and the center of the shaft. The recorded voltage and calculated torque is plotted in Figure 5.7. The calibration curve that best fits the 9 data points is $\tau = (3.36\,\mathrm{N\,m\,V^{-1}})V + (0.26\,\mathrm{V})$ with $R^2 = 0.98$.

Torque measurements were taken over a $60\,\mathrm{s}$ interval after allowing the drum to reach steady state. Steady state was achieved after running under the same conditions as in a PEPT experiment for approximately $60\,\mathrm{s}$.

5.4.2 Viscosity

The viscosity is a key parameter in the viscous number of granular suspensions. A mixture of glycerol and water was used as the suspending medium which is commonly used when fluids of different viscosities are required. The viscosity is very sensitive to changes in temperature and the ratio of water to glycerol. Therefore a series of viscosity measurements of known solutions were performed in order to make sure that solutions of known viscosity are prepared. In addition, a series of samples were taken during PEPT experiments to see whether the viscosity of the fluid changed over time. This was done because there existed a possibility that fine particles from glass beads or the rubber lining of the drum could mix with the fluid and change its viscosity.

The parametrisation by Cheng [129] was tested by measuring the viscosity of a series of sample mixtures. A glycerol/water solution was prepared by mixing $180\,\mathrm{g}$ of glycerol and $45\,\mathrm{g}$ of water in a beaker. A $50\,\mathrm{g}$ sample was taken from the mixture and the remainder diluted with $25\,\mathrm{g}$ water. This procedure was repeated 6 times after which samples of $\{30, 40, 50, 60, 70, 80\}$% w/w glycerol were prepared. Each sample's viscosity was measured at $T = 25\,^{\circ}\mathrm{C}$ and $T = 35\,^{\circ}\mathrm{C}$ using a Brookfield DV-I viscometer. Figure 5.8(a) shows the results of our measurements and compares them to the parametrisation by Cheng [129].

The effects of the milling process on the viscosity of the mixture was tested by taking samples from the drum during PEPT experiments. Figure 5.8(b) shows the viscosity of these samples at $T = 25\,^{\circ}\mathrm{C}$ against the amount of time that the sample spends in the drum. It is reasonable to conclude that after a steady state is reached the viscosity of the water/glycerol mixture was not affected by contamination of grinding products, because of the overlap of uncertainties for viscosity measurement (except the first data point).

The parametrisation by Cheng [129] was used to estimate the viscosity of glycerol/water mixtures in this work, given that it produced viscosity with good agreement with our measurements and that the viscosity remained constant during the course of a PEPT experiment.

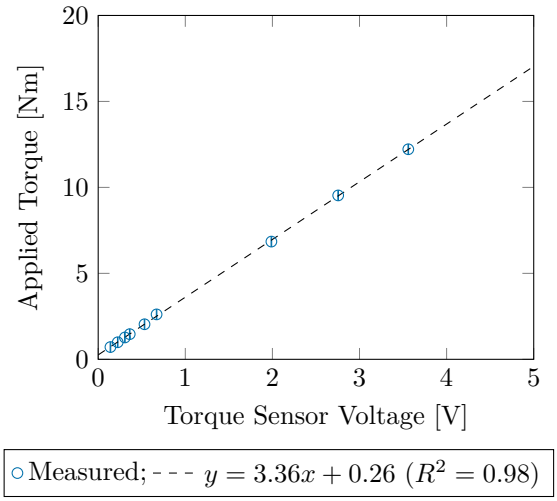

Figure 5.7 – Calibration curve for the torque sensor.

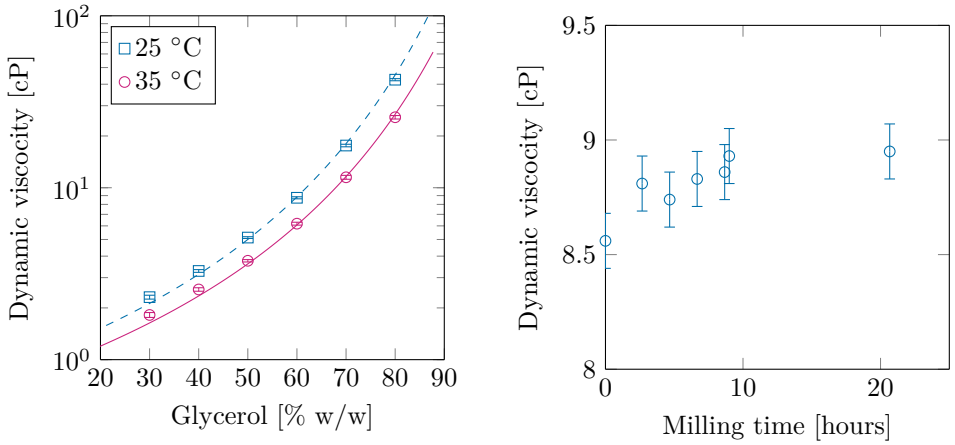

(a) **(b)**

Figure 5.8 – The viscosity of water/glycerol mixtures at (a) different ratios and temperature compared between our measurements and the parameterisation by Cheng [129] and (b) measured viscosity at $T = 25\,°\mathrm{C}$ of a $60\,\%$ w/w mixture used in a lab scale rotating drum over time.

5.5 Discussion

This chapter introduced the PEPT technique. The physical principles of how it works was discussed, as well as how measurements are taken and the results processed to constitute the tracer's position as a function of time. Noise in the velocity-time function can also be reliably reduced while retaining all the key features required to make comparisons to DEM data (Table 5.5). Chapter 4 discussed how particle level data is coarsegrained to convert this time series to a function of coordinates.

Viscosity and torque measurements were also discussed. The viscosity of water/glycerol mixtures was measured and showed that we could reliably determine the viscosity using Cheng [129] (Figure 5.8(a)). The method for calculating the viscosity of water/glycerol mixtures was confirmed to work over a wide range of water to glycerol ratios and over the temperature range expected in PEPT experiments. It was also established that the mixture's viscosity does not change over the duration of a PEPT experiment (Figure 5.8(b)). Torque measurements were taken to compare the power dissipation between simulations and experiments. The torque senor was calibrated (Figure 5.7) to facilitate comparisons between PEPT and DEM results made in Chapter 7.

The viscosity is a critical parameter for the lubrication approximation, which was discussed in Chapter 3, and a reliable way of determining the viscosity of experiments is needed to make comparisons to simulations. The lubrication approximation can be interrogated for different values of the fluid viscosity by comparing DEM results to PEPT experiments discussed in this chapter. PEPT experiments were performed with water/glycerol mixtures with viscosities of $0.011 \pm 0.001\,\mathrm{Pa\,s}$, $0.038 \pm 0.005\,\mathrm{Pa\,s}$ and $0.25 \pm 0.04\,\mathrm{Pa\,s}$.

These values were chosen to target the inertial Stokes regime ($S_t > 1$). The shear rate in a rotating drum operating in this Froude regime was estimated $\dot{\gamma} \approx 20\,\mathrm{s}^{-1}$ using Govender et al. [27]. In this Stokes regime, particle inertia dominate over fluid effects, which suggest that simulations performed with only the lubrication approximation could give reasonable agreement with experiments. Comparisons between DEM and PEPT are made in Chapter 7.

Ergodicity of PEPT experiments

6

Positron Emission Particle Tracking (PEPT) usually measures the position of a single tracer. The previous chapter described how the particle scale information can be coarsegrained to infer information about the behaviour of the bulk material. The ergodic hypothesis, which states that the temporal average of a single representative particle should be equal to the spatial average of the ensemble of particles, underpins this technique. However, this is only true provided that the time average is taken over a sufficiently long interval. In the PEPT experiments carried out as part of this study the position and velocity of one radio labeled tracer was recorded and the ergodic hypothesis is assumed in order to perform the coarsegraining from particle level data to a field that represents the average behaviour of particles near a point. The ergodic hypothesis is also used in other experimental techinques where a representative particle's dynamics is measured and statistical properties of an ensemble deduced. Examples include:

- Radioactive Particle Tracking (RPT) – a technique very similar to PEPT, but the radioactive tracer is labeled with a γ-emitter instead of a positron emitter. See Chaouki et al. [133] for comparisons between RPT and PEPT.
- Single Particle Tracking (SPT) – a technique where a molecule is labeled with a heavy element such as gold and imaged using optical means. A recent review of the method by Manzo and Garcia-Parajo [134] also mentions that the diffusive process, which the method is used to study, is often not Ergodic.

The ergodic hypothesis was proposed to analyse PEPT data by Wildmann et al. [32]. A very important question when designing a PEPT experiment is how much tracking time is needed to allow the tracer to explore the entire phase space of the dynamics being investigated. however, since the early study by Wildmann et al. [32], not much has been done to determine the tracking time needed to fulfill the requirements of the Ergodic hypothesis.

In this chapter, results from a series of the long duration PEPT experiments described in Section 5.2.1 are presented and several techinques are used to investigate the ergodicity of the system in an attempt to provide a more defined methodology for testing ergodicity of the system in experiments.

The models of granular rheology and dense suspensions discussed in Chapter 2 relate coarsegrained quantities to each other. In order to make comparisons between PEPT experiments, Discrete Element Method (DEM) simulations and these models, particle level data needs to be coarsegrained, and the ergodic hypothesis underpins the coarsegraining routine for PEPT data. These experiments where carried out with mono sized glass beads, using three different particle diameters ($d = 5\,\mathrm{mm}$, $d = 8\,\mathrm{mm}$ and $d = 10\,\mathrm{mm}$) without a fluid.

6.1 Experimental Considerations

Before investigating the dynamics of the tracer and charge some side effects of the PEPT technique which may influence the results are considered. These are related to the nature of the radioactive decay of the tracer particle and measurement of the periodic time series.

6.1.1 Scattering and absorption

Gamma rays emitted by the tracer can interact with the matter in the mill via two processes: Compton scattering and photoelectric absorption (Badawi [135] and Evans [136]).

In Compton scattering the gamma ray interacts with an electron and loses some of its energy and changes its direction. The energy of the gamma ray after scattering is given by,

$$E' = \frac{E}{1 + \left(\frac{E}{m_e c^2}\right)(1 - \cos\theta_s)} \ , \tag{6.1}$$

where, E is the initial energy, θ_s the scattering angle and $m_e c^2$ the electron's rest energy. Compton scattering can result in large deflections of the gamma rays, for instance a $511\,\mathrm{keV}$ gamma ray can undergo a $25°$ deflection after a scattering event in which $10\,\%$ of the energy is transferred to the electron (Badawi [135]).

In photoelectric absorption, a γ-ray is absorbed by an electron and the electron is knocked from the bound state of the atom. Both γ-rays need to reach a detector element for an Line of Response (LOR) to be recorded. Photoelectric absorption will prevent one of the gamma rays from reaching the detector and no LOR will be recorded.

The combination of these two effects is expressed in the relation:

$$I(x) = I_0 \exp\left(-\mu x\right) \ , \tag{6.2}$$

where I_0 is the initial intensity of a photon beam and $I(x)$ is the intensity of the beam at a depth x into the material. The absorption coefficient μ determines the degree to which the beam is attenuated by the material it travels through. The probability that a single photon will travel a distance x in the material is given by $p = I(x)/I_0 = \exp\left(-\mu x\right)$. In a PEPT experiment two back to back gamma rays need to travel through the charge, which acts as the attenuating medium, to reach the detectors. If the tracer is at a position x_t the probability that a LOR will be recorded is given by

$$p_{\mathrm{LOR}} = p_1 p_2 = \exp(-\mu|x_1 - x_T|)\exp(-\mu|x_2 - x_T|) = \exp(\mu|x_1 - x_2|), \tag{6.3}$$

where x_1 and x_2 are the two positions at which the LOR intersects the free surface or the shell of the drum.

A typical PEPT tracer is made from ^{68}Ga, which has a half-life of $68\,\mathrm{min}$, so over the course of a $2\,\mathrm{h}$ run the tracer's activity will drop to about $25\,\%$ of its initial activity. The triangulation routine uses a fixed number of lines to triangulate a point, so the time step between the first and last line will increase as events towards the end of the run are triangulated. If, after discarding the required number of lines, the mean distance between the triangulated point and the remaining lines is not small enough the triangulated point will be discarded.

For experiments involving moving charge such as rotating drums, regions near the center of the charge, or the Center of Circulation (CoC) for rotating drums, might be shielded by charge, resulting in a lower density near the CoC. This effect is noticeable as the tracer ages and becomes less radioactive. Figure 6.1 shows the solids fraction calculated using runs 1 to N, with N set to 3, 4, 5 and 6 in Figures 6.1(a), 6.1(b), 6.1(c) and 6.1(d), respectively. Notice the 'hollow' spot developing near the center of circulation as the tracer ages, indicating that data recorded with a less active tracer contributes disproportionately to the solids fraction near the edge of the bed.

Figure 6.2 compares the variation in the solids fraction with the particle speed. There is a clear inverse correlation between the two quantities, suggesting that the solids fraction is poorly sampled when the speed of the material is relatively low. It is also significant that the variation in the solids fraction tends to increase with an older tracer.

6.1.2 The Nyquist Frequency

The position-time curve which is reconstructed by the triangulation algorithm is a discrete signal and as such is only able to reproduce oscillations of the tracer when the frequency of oscillation is smaller than a certain cutoff frequency. This limit is the Nyquist frequency and for discrete time systems is half the time step between position recordings. If the tracer's angular velocity is larger than the Nyquist frequency, the scanner and subsequently post processing won't have enough resolution to resolve the tracer's trajectory.

The Nyquist frequency for a time step δt (sample rate $1/\delta t$) between PEPT data points is $f_N = 2/\delta t$. The associated upper limit on the angular frequency is $\omega > \omega_N = 2\pi f_N = 4\pi/\delta t$. For a time step of $\delta t = 0.01\,\mathrm{s}$, $\omega_N = 1256$ Hz or 75000 RPM.

A useful plot to consider is that of the average distance from the CoC vs the angular velocity of the tracer. The tracer's trajectory is divided into 6 s slices and for each slice the average distance to the CoC and its dominant Fourier mode of its rotation around the CoC is computed. This relationship is shown in Figure 6.3. The same linear trend is followed for all particle sizes and we note that near the CoC ($r = 0$) the angular velocity is $\omega \approx 170$ RPM, about two orders of magnitude below the Nyquist frequency.

This means that the PEPT sampling rate is able to record the tracer's position ~ 100 times per rotation near the CoC. It therefore seems like we don't have data near

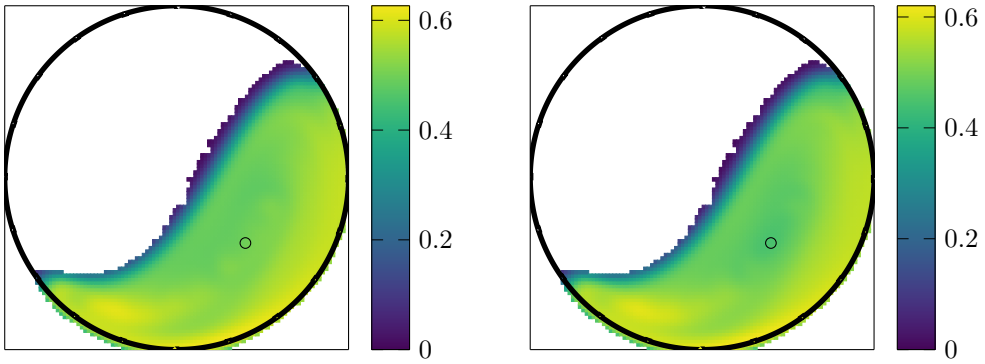

(a) 3 runs per tracer **(b)** 4 runs per tracer

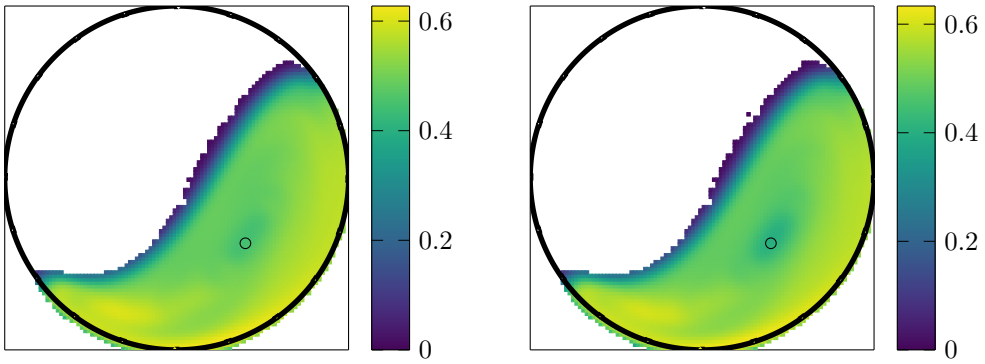

(c) 5 runs per tracer **(d)** 6 runs per tracer

Figure 6.1 – The solids fraction for $d = 5\,\mathrm{mm}$ calculated using the first few runs. Notice the 'hollow' spot developing near the Center of Circulation (CoC), denoted by $\circ$, as the tracer ages, indicating that data recorded with a less active tracer contributes disproportionately to the solids fraction near the edge of the bed.

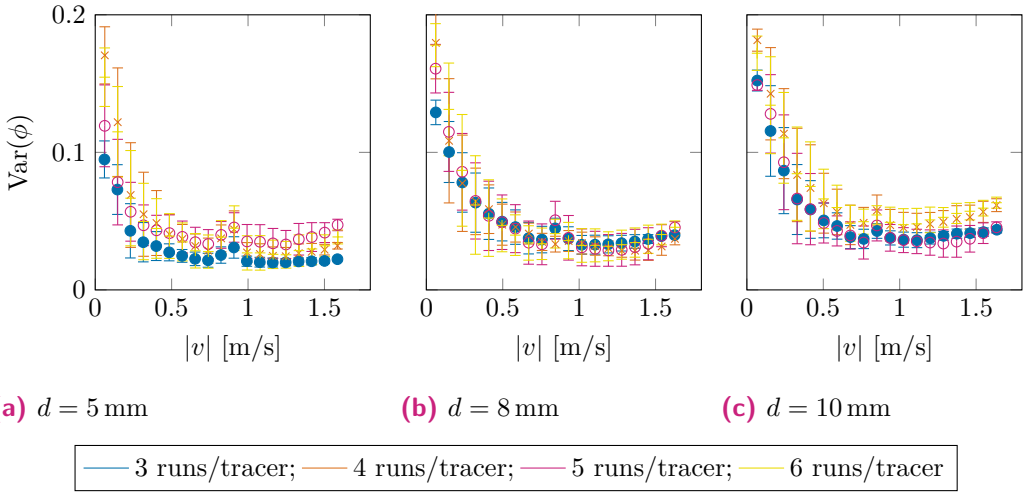

(a) $d = 5\,\mathrm{mm}$ **(b)** $d = 8\,\mathrm{mm}$ **(c)** $d = 10\,\mathrm{mm}$

Figure 6.2 – Variance of the solids fraction vs. speed for different particle sizes and number of runs per tracer. The inverse correlation between the speed and variation in solids fraction indicates that regions where the speed is small relates to an under sampled solids fraction. A low velocity often occurs near the Center of Circulation (CoC).

the CoC because the tracer does not spend any time there, not because of a lack of resolution.

6.2 Signatures of Ergodicity

This section investigates whether the dynamics of the charge in a rotating drum is ergodic. The rate of convergence of the solids fraction and velocity is investigated, similar to Wildmann et al. [32]. Ergodicity is closely related to how well a system is mixed. It might be strange to consider the mixing properties of a system with mono sized beads, but in this study our requirement is that the system be properly mixed if the PEPT tracer is to reach every point in the system's phase space. Hill et al. [107] compared several rotating mixers by contrasting the dynamical systems that dictate the motion of the charge to study their mixing performance. Doucet et al. [108, 109] developed several techniques for investigating mixing in granular systems. Two of these tools, namely Poincaré maps and the global mixing index, are employed to investigate the ergodicity for the data obtained in this study.

6.2.1 Converging Solids Fraction

Wildmann et al. [32] compared spatial averages to test the ergodicity of the system in their experiment. Each voxel was subdivided into a 3×3 grid. The solids fraction in the voxel was compared to the average and standard deviation in the 9 sub-voxels. They found that in the dilute regions the variation of the solids fraction was less than $5\,\%$, while in denser regions the variation was as high as $10\,\%$.

In this study, time averages will be compared instead of averages between spatially separated voxels. For rotating drums and experiments that were carried out over a long period of time, time averages are more appropriate, because rotating drums exhibit flows that have a complicated spatial dependence and even comparing averages at nearby locations might skew the results. For example, Figure 6.1 shows the solids fraction in the plane transverse to the axis of the mill and the solids fraction varies from zero to random close packing in distances much shorter than the mill radius. Further, the data recorded was taken over a long time period and by dividing the data set in the time domain, T, into intervals of duration $w_t < T$, conclusions about the average behaviour of potential experiments that are carried out for a total time when $T = w_t$ can be drawn.

Averages are calculated using the results reported in the previous chapter, but with a Gaussian temporal smoothing function:

$$\rho(x,t) = N \int dt' m_T \ \exp(x - x_T) \exp(t - t_T) \ , \tag{6.4}$$

$$v(x,t) = N \int dt' m_T v_T \ \exp(x - x_T) \exp(t - t_T) \ . \tag{6.5}$$

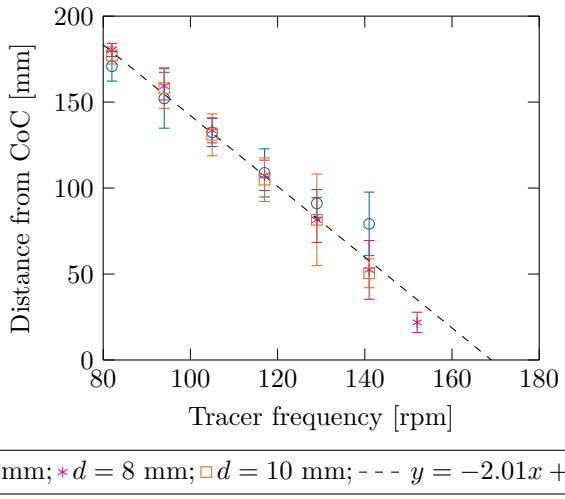

Figure 6.3 – The average distance from the Center of Circulation (CoC) against the angular frequency for each 6 s slice of the tracer's trajectory. The intercept on the ω-axis of $\omega \approx 170$ RPM indicates that the temporal resolution of the Positron Emission Tomography (PET) scanner is sufficient to record the rotation of the tracer.

Here $\rho(x,t)$ is the average density of the bulk material and is related to the solids fraction by $\phi(x,t) = \rho(x,t)/\rho_p$, with ρ_p the particle density. A new parameter, the smoothing time w_t, is introduced to the coarsegraining scheme by using a Gaussian smoothing kernel for the temporal average. When ensemble averages are evaluated at time t from the start of the experiment, data points with time stamps outside the interval $[t - w_t, t + w_t]$ will have a negligible influence on the coarsegrained result. The PEPT tracer's position and velocity was recorded in 20 min batches and has to be concatenated to constitute the tracer's position $\vec{r}(t^\beta) = \left\langle x(t^\beta), y(t^\beta), z(t^\beta) \right\rangle$ and velocity $\vec{v}(t^\beta) = \left\langle v_x(t^\beta), v_y(t^\beta), v_z(t^\beta) \right\rangle$. A single tracer can be used to record 8 to 10 such batches before the activity of the tracer drops to below a usable level. Each of these batches were recorded under the same conditions and therefore it should not make a difference in which order they are used when constructing the functions $\vec{r}(t^\beta)$ and $\vec{v}(t^\beta)$. In order to eliminate any systematic bias that may have occurred during the experiment, the batches are permuted randomly when doing this reconstruction. Each permutation will yield slightly different volume fractions and velocity fields and we investigate the fluctuations in these quantities to find a suitable averaging time. One would expect to see very small fluctuations when the ergodic hypothesis holds, but the fluctuations should increase when smaller w_t is used. A smoothing time that gives 'small enough' fluctuations will give an indication of a minimum tracking time required for a PEPT experiment to yield reliable volume fraction and velocity data.

A set of time values are chosen $\{t_j\}$ that are w_t apart or $w_t = t_{j+1} - t_j$. The solids fraction and velocity is evaluated for each permutation at each t_j. The solids fraction and average speed of the tracer, calculated with different w_t, are shown in Figure 6.4. The error bars represent the standard deviation associated with averages

over different permutations of the tracks. Judging by the error bars, the speed (Figure 6.4(b)) converges much quicker than the solids fraction, indicated by very small variations in the velocity when using an averaging interval of just $w_t = 15\,\mathrm{min}$. However, large variations were still noticed in the solids fraction when averaging over $3\,\mathrm{h}$ time intervals (Figures 6.4 (a), (c) and (e)).

This suggests that PEPT is much better suited to be measuring the bulk velocity of the charge than measuring the solids fraction. However, the solids fraction can be determined as long as the tracer is tracked for a sufficiently long enough time. In the case presented, the tracer's position-time curve has to measured for more than $3\,\mathrm{h}$ before the solids fraction can be established within $10\,\%$ near the CoC, although $5\,\%$ is achieved in the flowing and rising region, away from the CoC (Figure 6.4(f)).

The tracer moves at a consistent speed every time it is near a particular point, resulting in an average velocity with a small variance. However, the tracer does not spend the same amount of time everywhere in the mill. The dilute region near the CoC can result when the tracer does not spend much time in that region.

6.2.2 Poincaré Maps

First recurrence maps or Poincaré maps are regularly used to study the stability of fixed points of dynamical systems. As will be discussed shortly, a Poincaré map is a $(n-1)$-dimensional discrete dynamical system derived from a n-dimensional continuous dynamical system. Because a Poincaré map has one less spatial dimension, it is often easier to visualize and explore long term properties of the system by looking at the Poincaré map than by looking at the original system. This is possible because it can be shown that a Poincaré map will have the same fixed points as the original system and, in particular, that the stability of the corresponding points will be the same.

For a continuous dynamical system of the form

$$\frac{d\vec{X}}{dt} = f(\vec{X})\ , \tag{6.6}$$

a solution or trajectory $\vec{X}(t)$ is a mapping from the time domain to an n dimensional space or $\vec{X} : R \to R^n$. If a point $\vec{p}$ satisfies the condition $f(\vec{p}) = 0$, a solution with the initial condition $\vec{X}(0) = \vec{p}$ will have the solution $\vec{X}(t) = \vec{p}$ for all time. In other words once a trajectory reaches such a point it will stay there forever. Points that satisfy this condition are called fixed points and a lot of information about the solutions of dynamical systems can be gained by studying the behaviour of trajectories near fixed points.

Uniqueness of solutions implies that trajectories cannot intersect, so trajectories near fixed points will often orbit the fixed point while asymptotically moving towards or away from it. Fixed points are classified by this behaviour as stable, if trajectories tend to stay within a neighbourhood around the fixed point, or unstable otherwise.

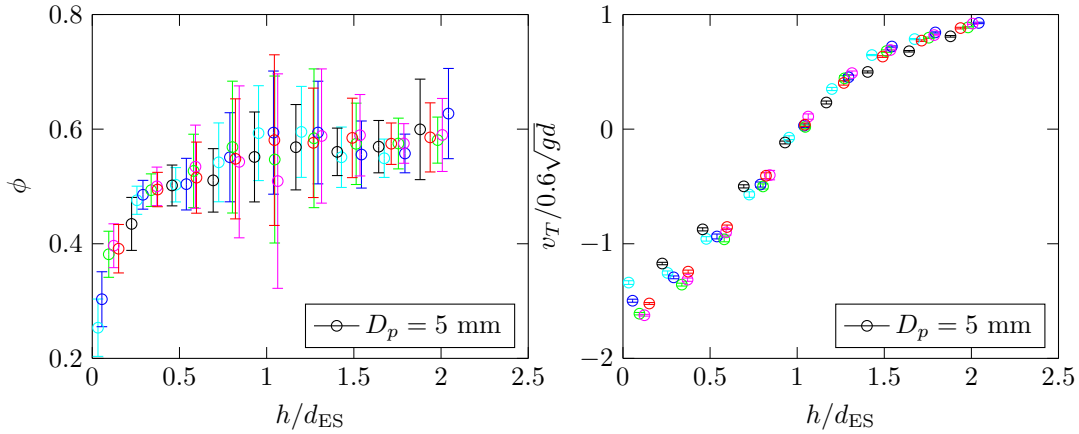

(a) Solids fraction with $w_t = 15\,\mathrm{min}$.

(b) Speed with $w_t = 15\,\mathrm{min}$.

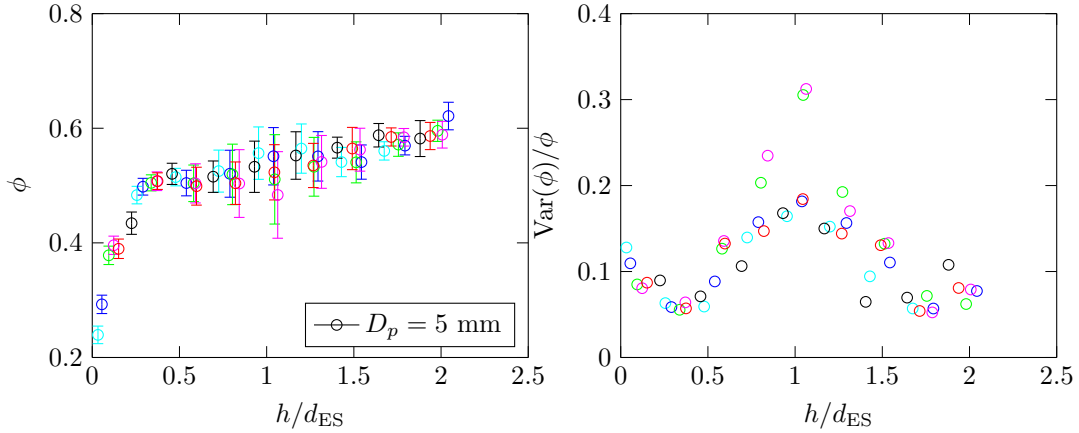

(c) Solids fraction with $w_t = 60\,\mathrm{min}$.

(d) Coefficient of variance of ϕ with $w_t = 60\,\mathrm{min}$.

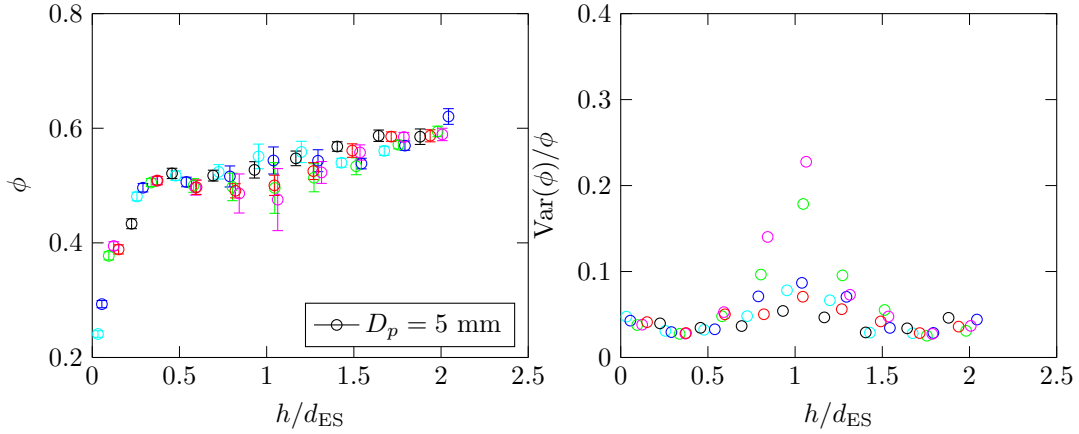

(e) Solids fraction with $w_t = 180\,\mathrm{min}$.

(f) Coefficient of variance of ϕ with $w_t = 180\,\mathrm{min}$.

Figure 6.4 – The solids fraction profiles for different averaging times w_t are shown in (a), (c) and (e). The speed profile, and very small variance, with $w_t = 15\,\mathrm{min}$ is shown in (b). The relative standard deviation of the solids fraction is shown in (d) and (f) showing a substantial reduction in variance between $w_t = 60\,\mathrm{min}$ and $w_t = 180\,\mathrm{min}$. Error bars indicate the standard deviation of averages taken at different times during the experiment.

A Poincaré section is created by placing a $(n-1)$-dimensional surface in the path of the trajectory and recording the points $\{\vec{X}_i\}$ at which the trajectory and the surface intersect. A Poincaré map $\Delta\vec{X} = \vec{X}_{i+1} - \vec{X}_i$ is the function that projects one intersection point to the next between subsequent periods of the orbit. This procedure is presented in Figure 6.5 for visualisation.

Poincaré maps have been used in the context of mixing in granular flow by Hill et al. [107] and Doucet et al. [108]. The tracer's position can be thought of as the trajectory of a dynamical system such as in equation (6.6) with $n = 3$ and $\vec{X}(t) = (x(t), y(t), z(t))$. These trajectories are periodic orbits and in the case of rotating drums the CoC is the fixed point $\vec{p}$. Furthermore we can place an imaginary plane extending from the axis at the center of circulation at a fixed angle of $\theta = 45°$ below the x-axis (see Figure 6.5) and then calculate the Poincaré map on this two dimensional surface. We can find all the data points for which the angular position around the CoC is $\theta(t_i) = \theta_i < 45°$ and at the next time step $\theta(t_i + \Delta t) > 45°$. The related axial ($z_i$) and radial ($r_i$, centered at the CoC) position of the tracer is recorded and the Poincaré map is calculated as the difference between these positions from one orbit to the next, $(\Delta z, \Delta r) = (z_{i+1} - z_i, r_{i+1} - r_i)$. The resulting Poincaré map is then coarsegrained with a simple binning scheme to better capture the average behaviour of the tracer.

Figure 6.6 shows the Poincaré map for the three configurations in this experimental study. The Poincaré map reveals dynamics that occur on the zr-plane after subsequent orbits about the CoC. Of particular interest are the vortices that appear on the left and the right side of the cylinder and the behaviour near the CoC. The vortices seems to be stable fixed points of the dynamical system that describes the tracer's trajectory. As a consequence, once the tracer finds itself near one of these vortices it will tend to stay there and the residence time calculation will tend to over sample in that region. On the other hand the CoC is an unstable fixed point, the tracer will tend to be pushed away from it and the residence time in the region near the CoC will tend to be under-sampled.

Another feature of interest is that the vertical plane where $z = 0$ seems to be an unstable 'fixed point' too. This means that once the tracer is in the left or the right side of the drum it will tend to be stuck in that half of the mill.

The implications of these Poincaré maps for PEPT are:

- The tracer can be stuck in one half of the drum or near a vortex, and therefore cannot capture axial motion with a single tracer and cannot get good sampling of the axial field of view.

- This could be a good motivation for multiple particle tracking, which will allow larger amounts of data to be captured in the same amount of time.

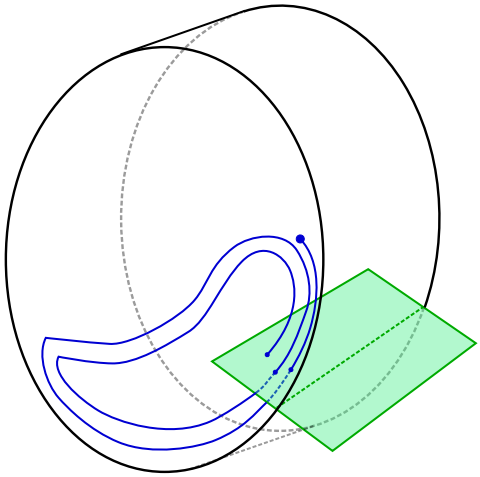

Figure 6.5 – The Poincaré map records the points of intersection between the trajectory of the PEPT tracer and a plane. The trajectory is a continuous dynamical 3D system, while the Poincaré map is a discrete 2D dynamical system. However, it can be shown that both systems share the same fixed points and that the stability of these fixed points is the same in 2D and 3D.

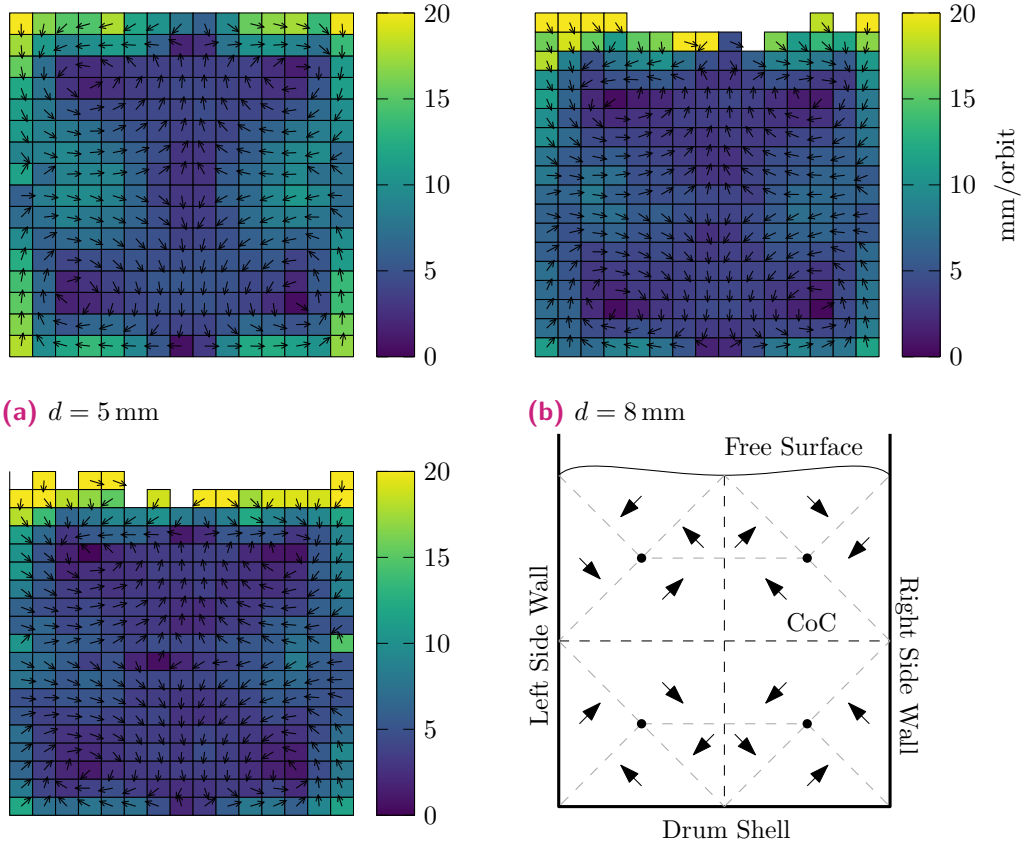

(a) $d = 5\,\mathrm{mm}$ **(b)** $d = 8\,\mathrm{mm}$

(c) $d = 10\,\mathrm{mm}$ **(d)** Key

Figure 6.6 – Poincaré maps of different particle diameters (a) $d = 5\,\mathrm{mm}$, (b) $d = 8\,\mathrm{mm}$ and (c) $d = 10\,\mathrm{mm}$. The Poincaré maps reveals that the Center of Circulation is an unstable fixed point and that the charge rarely crosses $z = 0$ plane. The result is a region at the intersection of these planes that does not readily exchange particles. The presence of vortices indicates regions where the tracer could spend proportionally more time and explains why the region near the Center of Circulation (CoC) is under sampled.

- Questions around what factors could influence the vortices are outside the scope of this study. It is possible that their existence is an artifact of mono sized particles, the drum speed or fill level.

6.2.3 Global Mixing Index

The global mixing index was used by Doucet et al. [108] as a measure of how well a granular system is mixed. The global mixing index was constructed by dividing the tracer's position into N trajectories, each of duration T^*. Each of the N trajectories can be thought of as an independent particle and the spatial distribution, in cylindrical coordinates, around the CoC of these particles at time t is denoted by $\vec{R}_N(t) = (r_N(t), \theta_N(t), z_N(t))$. The coordinates of the particles can be non-dimensionalised by defining

$$\tilde{r}_N(t) = \frac{r_N(t) - \langle r_N(t) \rangle}{\sigma(r_N(t))} \,, \tag{6.7}$$

$$\tilde{\theta}_N(t) = \frac{\theta_N(t) - \langle \theta_N(t) \rangle}{\sigma(\theta_N(t))} \quad \text{and} \tag{6.8}$$

$$\tilde{z}_N(t) = \frac{z_N(t) - \langle z_N(t) \rangle}{\sigma(z_N(t))} \,, \tag{6.9}$$

where $\langle \cdot \rangle$ and $\sigma(\cdot)$ are the average over the N particles and the associated standard deviation, respectively.

The global mixing index is defined as the three dimensional vector

$$\vec{C}(t) = \left(\langle \tilde{r}(t)\tilde{r}(0) \rangle \,, \left\langle \tilde{\theta}(t)\tilde{\theta}(0) \right\rangle, \langle \tilde{z}(t)\tilde{z}(0) \rangle \right) \,. \tag{6.10}$$

Each of the three components of C lies between -1 and 1 and is interpreted as a measure of the correlation between the configuration of the N particles at time $t < T^*$ in relation to the initial configuration at $t = 0$. A value of one 1 means each of the particles are in their initial position and a value of 0 corresponds to a purely random configuration.

The global mixing index for the three different particle sizes is shown in Figures 6.7(a), 6.7(b) and 6.7(c). The C_θ component goes to zero very quickly because of the rotation of the drum. Thereafter, the C_r component goes to zero, which corresponds to mixing between layers of particles concentric to the CoC. The C_z component measures mixing in the axial direction.

It was noted that the rate at which C_z tends to zero depends on the particle size d. This could be because more particles are needed to fill the drum to the same level when the particle diameter is smaller and the charge permits more random configurations of particles. If the drum is rotating at the same speed, more time will be required to sample the required number of configurations for the ergodic hypothesis to hold.

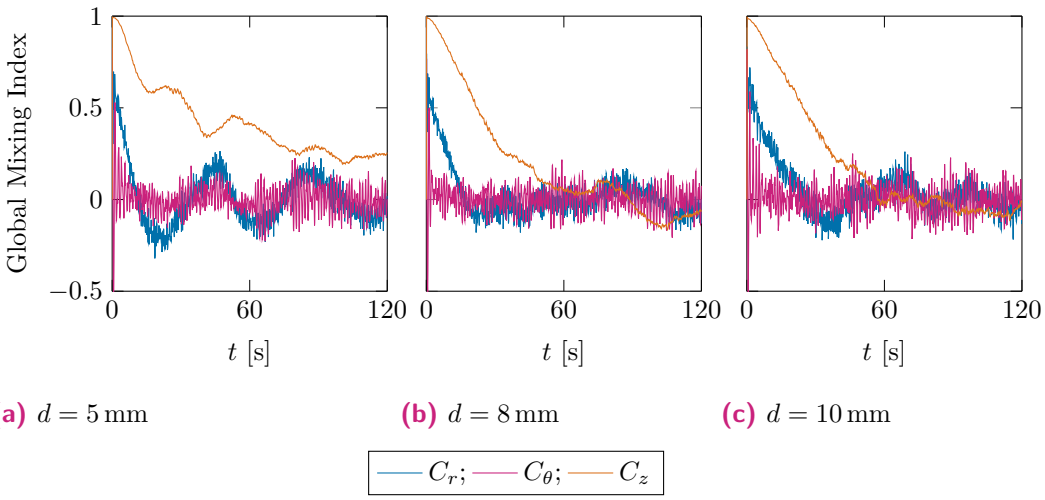

Figure 6.7 – Radial, angular and axial components of the global mixing index vs. time for (a) $d = 5\,\mathrm{mm}$, (b) $d = 8\,\mathrm{mm}$ and (c) $d = 10\,\mathrm{mm}$.

6.3 Speed Dependent Averaging

The consequence of the dynamics evident in the Poincaré map (Figure 6.6) is that the solids fraction tends to be under sampled near the CoC. Furthermore, Figure 6.2 suggests that the solids fraction is under sampled when the tracer's speed is low. This under sampling can be compensated for by using a larger averaging size w, which has the effect of using more samples of the tracer's position to calculate the solids fraction. The averaging window can be interpolated between the previous constant averaging size $1.5d_{10}$ (with $d_{10} = 10\,\mathrm{mm}$ the diameter of the largest particle size) and $5d_{10}$ by using the following averaging width,

$$w(v(\vec{x})) = 5d_{10} + (1.5d_{10} - 5d_{10})\frac{v(\vec{x})}{v_{\max}} \,. \tag{6.11}$$

Figure 6.8 shows the solids fraction when calculated using the averaging region $w = 3d_{10}$. Figure 6.9 shows the solids fraction when calculated using the averaging region related to the average speed calculated using $w = 3d_{10}$. An averaging time of $w_t = 3\,\mathrm{h}$ was used throughout with the same shuffling strategy employed as in Section 6.2.1. There is a substantial dip in the solids fraction near the CoC for $d = 5\,\mathrm{mm}$ when using a fixed averaging length (Figure 6.8 (a) and (b)). The dip is less pronounced for d=8 mm and d=10 mm, however the standard deviation of the average solids fraction indicates that the tracer did not sample the region near the CoC well. When calculating the solids fraction while using equation (6.11), the solids fraction becomes more uniform near the CoC and with smaller standard deviations (Figure 6.9).

Using the interpolated averaging volume from (6.11) makes it possible to calculate the average density and solids fraction in regions of the drum where the PEPT tracer is not able to penetrate.

6.4 Discussion

PEPT can only measure a few, and often only one, tracer particle at a time. The ergodic hypothesis is required to obtain coarsegrained results about the average behaviour of the ensemble. It states that the time average of a representative particle is equal to the spatial average of the ensemble as long as the time average is taken over a sufficiently long time interval. However, it is not known how much tracking time is needed for the hypothesis to hold.

This chapter investigated the dynamics of the charge in a rotating drum and the physics of the PEPT measurement technique to interrogate the ergodicity of the system. Two aspects of the measurement technique were discussed, namely the temporal resolution of the tracer's position and the radioactive decay of the tracer and shielding effect of the charge. Furthermore, convergence of the speed and solids fraction, Poincaré maps and the global mixing index were used to determine whether the dynamics of the charge is ergodic. The following conclusions can be drawn from the study of the dynamics. Figure 6.2 shows that the average speed of the bulk material and the variation in solids fraction is correlated, which means that the solids fraction is under sampled in regions where the charge moves slowly. Figure 6.4 compares the convergence of the speed and solids fraction and shows that the average speed converges on shorter time scales than the solids fraction.

The Poincaré map in the radial and axial plane, in Figure 6.6, shows that the dynamics prevents the tracer from visiting the region near the CoC and the plane perpendicular to the axis at $z = 0$. Possible interpretations for this phenomena are that there might be a region that does not exchange particles with the rest of the charge or that there seems to be vortices that could trap the tracer. The above mentioned effects could cause regions where the solids fraction appear more dense or dilute than what it actually is. The mixing index could be used to provide an upper bound to the required time to achieve a series of random configurations in the mill that depends on the number of particles and thereby the particle diameter. The required tracking time appears to depend on the particle size (Figure 6.4 and Figure 6.7).

The use of mono-sized beads in this experiment may result in regular packing or crystallisation (Andreotti et al. [65]). A reasonable question is whether a regular packing can occur in rotating drums in the Froude regime explored in this thesis. Poincaré maps can provide a concrete way to study this phenomena by comparing Poincaré maps of mono-sized and polydisperse systems. However, mono-sized systems pose on limitation no the models of granular rheology and granular suspensions considered in the next chapter.

The results above suggest that the under sampling of the solids fraction is compensated for by choosing an averaging width that is related to the speed near a particular point. Equation (6.11) makes a linear interpolation between two averaging radii that is equal to the smaller radius at the probe point, where the speed is maximum,

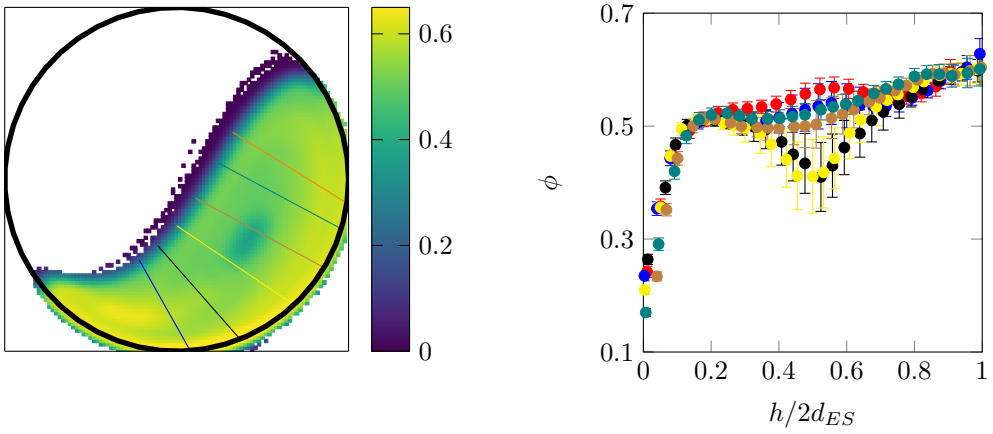

(a) $d = 5\,\mathrm{mm}$ **(b)** $d = 5\,\mathrm{mm}$

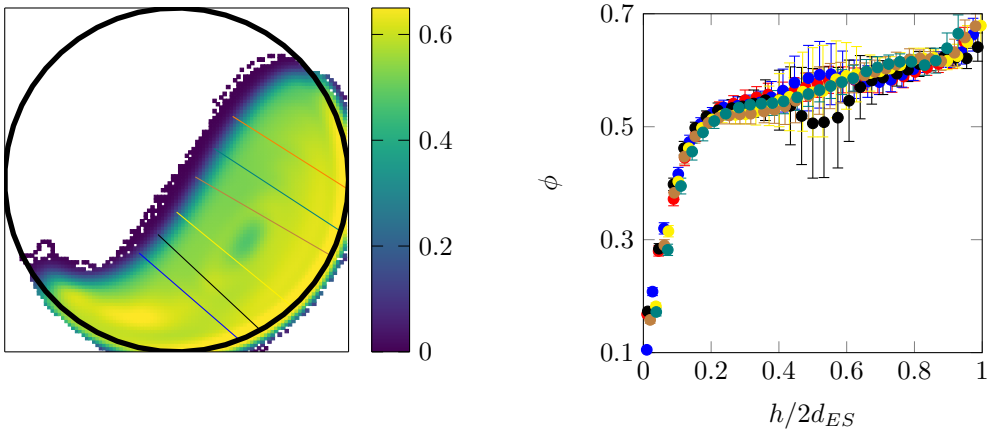

(c) $d = 8\,\mathrm{mm}$ **(d)** $d = 8\,\mathrm{mm}$

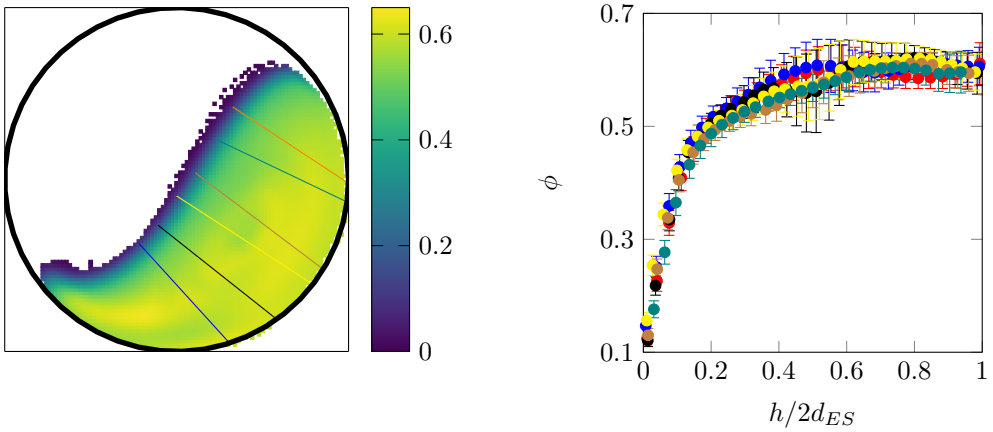

(e) $d = 10\,\mathrm{mm}$ **(f)** $d = 10\,\mathrm{mm}$

Figure 6.8 – The solids fraction calculated using a fixed averaging radius of $w = 3d_{10}$ and $w_t = 180\,\mathrm{min}$ for each of the particle sizes. Figures on the left show the solids fraction along lines perpendicular to the free surface, and error bars indicate the standard deviation when taking averages over $180\,\mathrm{min}$ segments. Large variations in the solids fraction is observed near the Center of Circulation (CoC) in the profiles perpendicular to the free surface.

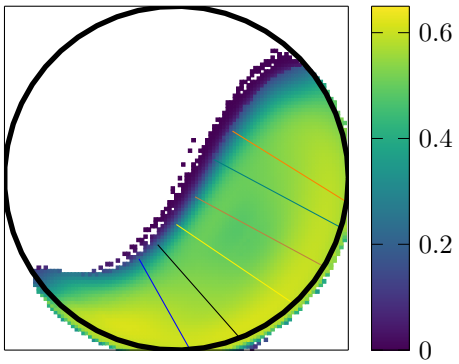

(a) $d = 5\,\mathrm{mm}$

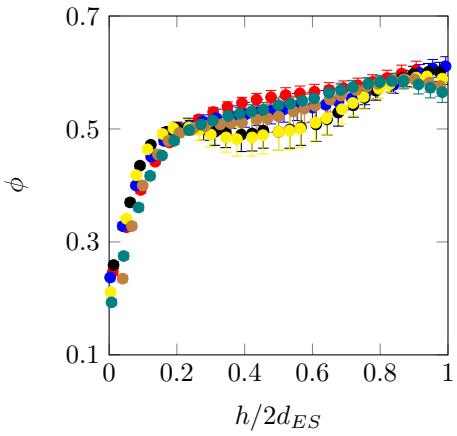

(b) $d = 5\,\mathrm{mm}$

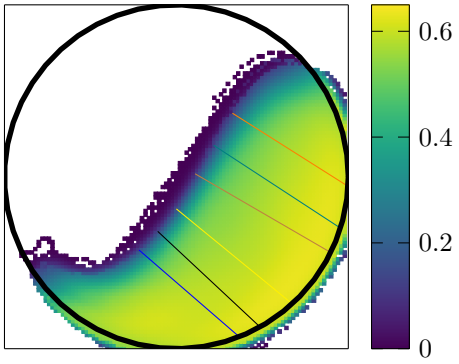

(c) $d = 8\,\mathrm{mm}$

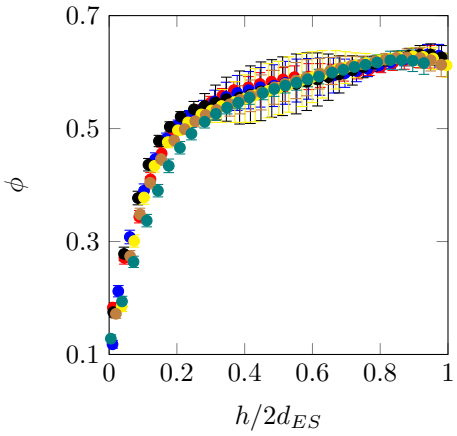

(d) $d = 8\,\mathrm{mm}$

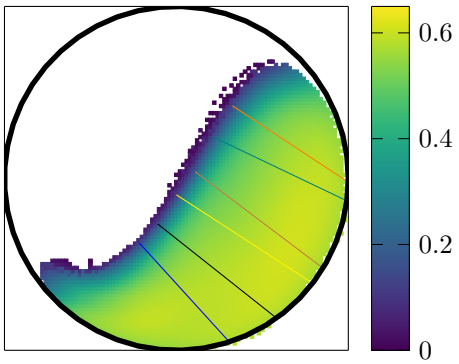

(e) $d = 10\,\mathrm{mm}$

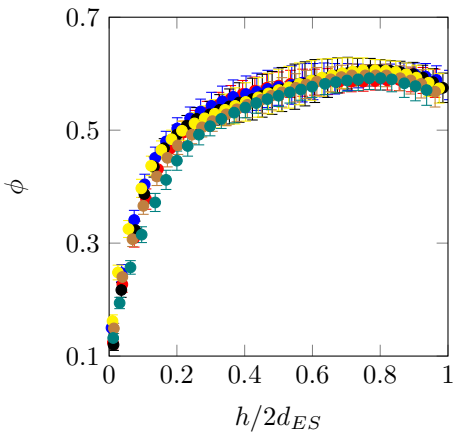

(f) $d = 10\,\mathrm{mm}$

Figure 6.9 – Same as in Figure 6.8, but with the solids fraction calculated using an averaging region that depends on the speed using equation (6.11). The variation in the solids fraction near the Center of Circulation (CoC) is greatly reduced.

and equal to the large radius when the speed is zero. The results are compared to a constant averaging radius in Figures 6.8 and 6.9, showing a significant decrease in the variance of the solids fraction near the CoC.

Rheology of granular suspensions

7

This chapter brings together the Discrete Element Method (DEM) simulations, Positron Emission Particle Tracking (PEPT) experiments and the rheology models from earlier chapters. PEPT experiments were carried out in a rotating drum with inner radius and length, $R = 230\,\mathrm{mm}$ and $L = 200\,\mathrm{mm}$, respectively, were performed. The drum's volume was filled to $50\,\%$ with $d = 10\,\mathrm{mm}$ glass beads and the gaps between the beads filled with a water/glycerol mixture. Three different ratios of water to glycerol and 7 different drum speeds was used. DEM simulations with a similar drum ($R = 200\,\mathrm{mm}$ and $L = 200\,\mathrm{mm}$) with spherical particles of radius and density $R = 10\,\mathrm{mm}$ and $\rho_P = 2400\,\mathrm{kg/m^3}$, respectively. An inter-particle force approximating a fluid lubrication effect between particles was applied between nearby particles. The viscosity in simulations were varied to mimic that of the experiments, and four representative angular velocities were used.

This chapter will focus on testing of the lubrication approximation – in the context of rotating drums – against experimental data and models proposed for the rheology of dense granular suspensions. This chapter will present results with the following aims:

- to compare the experimental and simulation data to evaluate the lubrication approximation
- to test the rheological models (visco-plastic, kinetic theory and non-local granular fluidity) against simulation data in rotating drums.

There are a number of data sets used for comparison in this chapter; the legend for figures in this chapter is shown in Table 7.1.

Table 7.1 – Legend for figures in this chapter. Colours represent different fluid viscosity η_f and shapes different drum speeds denoted by Froude number $F_r = \omega^2 R/g$ and percentage of $\omega_c = \sqrt{g/R}$.

	F_r	$\rightarrow$	0.090	0.123	0.160	0.202	0.250	0.3025	0.360
	$\%\omega_c$		30	35	40	45	50	55	60
DEM	η_f [Pa s]	0.001	□		○		◇		△
	↓	0.01	□		○		◇		△
		0.03	□		○		◇		△
		0.22	□		○		◇		△
PEPT	0.011 ± 0.001		■	⅄	●	+	◆	✶	▲
	0.038 ± 0.005		■	⅄	●	+	◆	✶	▲
	0.25 ± 0.04		■	⅄	●	+	◆	✶	▲

7.1 Comparison between Simulations and Experiments

7.1.1 Velocity Profiles

Scaling relations for velocity profiles can be derived from their constitutive equation (Jop et al. [33]). Their method involves performing a force balance on a volume element in the flowing layer. The $\tau/P = \mu(I)$ relationship is used to obtain a model for the shear rate as a function of the depth (y) of the flowing layer, which is then integrated to solve for the scaled velocity as a function of the scaled depth ($v_t/\sqrt{gd}$). The same procedure for deriving their scaling relation can be applied to other constitutive equations and it is therefore reasonable to expect that the same constitutive equation holds in both cases, if the same scaling relation is observed in simulations and experiments.

Figure 7.1 shows the scaled tangential velocity, $v_t/\sqrt{dg}$, against the distance from the equilibrium surface, along lines perpendicular to the free surface. The scaling between PEPT and DEM data is the same for all but the $\eta_f = 0.22\,\mathrm{Pa\,s}$ data set. Lines of best fit for the data are:

$$v_t/\sqrt{gd} = 0.282(y/d) + 0.161 \quad (R^2 = 0.949) \quad \text{all PEPT}, \tag{7.1}$$

$$v_t/\sqrt{gd} = 0.382(y/d) + 0.241 \quad (R^2 = 0.861) \quad \text{DEM } (\eta_\mathrm{f} \leq 0.03\,\mathrm{Pa\,s}), \tag{7.2}$$

$$v_t/\sqrt{gd} = 0.065(y/d) + 0.074 \quad (R^2 = 0.960) \quad \text{DEM } (\eta_\mathrm{f} = 0.22\,\mathrm{Pa\,s}). \tag{7.3}$$

This can be interpreted to prove that the same constitutive relation can be used to model simulations and experiments and that the simulations represent the dynamics in experiments accurately when $\eta_f \leq 0.03\,\mathrm{Pa\,s}$. However, for $\eta_f = 0.22\,\mathrm{Pa\,s}$ the lubrication approximation fails to reproduce the same rheology as in experiments. It is also surprising that the value of the fluid viscosity does not seem to change the scaling law in the experimental study significantly.

7.1.2 Stokes Number

The Stokes number, given by

$$S_t = \frac{\rho_p d_p^2 \dot{\gamma}}{\eta_f}\,, \tag{7.4}$$

where ρ_p is the particle density, d_p the particle diameter, $\dot{\gamma}$ the shear rate and η_f the fluid viscosity, can be calculated for both DEM simulations and PEPT experiments. As mentioned in Chapter 2, the Stokes number is a combination of three different time scales associated with granular particles moving relative to a fluid.

Figure 7.2 compares the Stokes number to the Froude number in simulations and experiments. The Stokes number is calculated at each coarsegraining location and the average value, with error bars representing the standard deviation, is plotted against the Froude number for that configuration. Separate plots are shown for

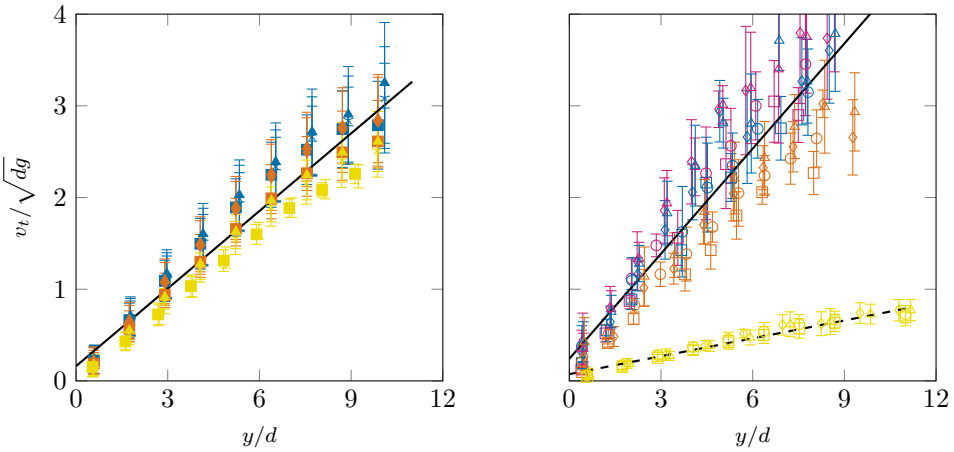

(a) PEPT **(b)** DEM

Figure 7.1 – The scaled tangential velocity vs the height above the equilibrium surface for various slices through the flowing layer for (a) Positron Emission Particle Tracking (PEPT) (b) Discrete Element Method (DEM). Five slices perpendicular to the free surface are chosen for each experiment or simulation and the average velocity is plotted with error bars representing the standard deviation.

the rising and flowing regions. Figure 7.2(b) shows the Stokes number averaged over probe locations in the rising region, which are identified when $v_x(\vec{x}) > 0$ and $v_y(\vec{x}) > 0$. Figure 7.2(c) shows data from the flowing layer, which is represented when $v_x(\vec{x}) < 0$ or $v_y(\vec{x}) < 0$.

The Stokes number in the flowing layer stays in the inertial or free-fall regime, which is when $S_t \gg 1$ according to Courrech du Pont et al. [7], even for high viscosities. Good agreement is observed between simulation and experiment for $\eta_f = 0.01\,\mathrm{Pa\,s}$ and $\eta_f = 0.03\,\mathrm{Pa\,s}$. However, not so much for $\eta_f = 0.22\,\mathrm{Pa\,s}$, which could be because drag and buoyancy forces are not taken into account. The Stokes number is lower for simulation data, indicating that the simulation results might be overestimating the effect of lubrication effects for high viscosities. It might be possible to get good agreement between simulation and experiment by using a smaller value for the viscosity in the simulations than what is measured for experiments.

7.1.3 Discussion

Simulations have two important advantages over experiments. They are cheaper to perform and provide direct access to all particle properties including forces between interacting particles. Despite these advantages, simulations cannot be performed in isolation. To have confidence that simulation results represent what happens in a physical system, validation of the simulation is required.

It is reasonable to conclude that the lubrication approximation is sufficient to model the effect of a granular material and interstitial fluid in a rotating drum configuration. Both velocity profiles of Figure 7.1 and the range of Stokes number of Figure 7.2 shows good agreement between PEPT experiments and DEM simulations.

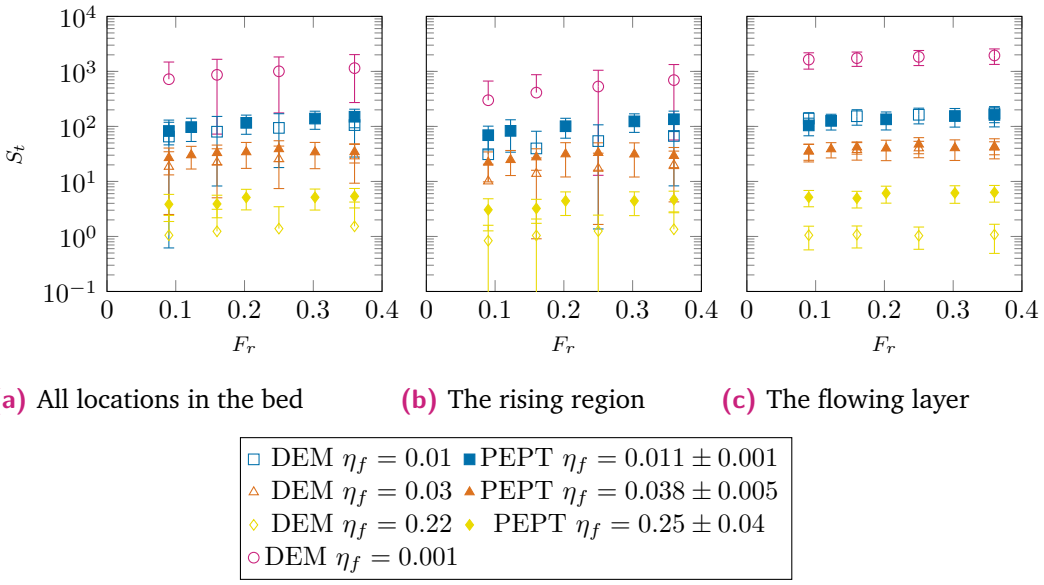

(a) All locations in the bed **(b)** The rising region **(c)** The flowing layer

Figure 7.2 – Stokes number (S_t) coverage in Positron Emission Particle Tracking (PEPT) experiments and Discrete Element Method (DEM) simulations as a function of the Froude number (F_r) for (a) all coarsegraining locations (b) locations in the rising region and (c) in the flowing layer. The Stokes number was calculated for each coarsegraining location; markers represent the average of all locations in a region and error bars the standard deviation.

There are several advantages to using the DEM lubrication approximation over experimental methods or coupled simulations. It is much cheaper (in terms of equipment cost, time, lab space and human resources) to run simulations than experiments. Simulations also provide opportunities to study more configurations and design ideas than with experiments. It is easier to run DEM simulations with the lubrication approximation, than coupled simulations. Other approaches to simulate dense suspensions include coupling DEM with Computational Fluid Dynamics (CFD) or Smooth Particle Hydrodynamics (SPH). However, both these solutions require substantially more computing resources: SPH require additional particles that represent the fluid to be simulated and CFD coupled simulations requires the fluid to be simulated in a separate software package. In addition DEM-CFD coupled simulations needs a software layer to communicate between the solid and fluid simulation. The lubrication approximation can be incorporated into open source DEM software packages and the simulations can be executed in a single step.

7.2 Comparisons to Rheology Models

This section compares DEM results from simulations described in Chapter 3 to the models that were discussed in Chapter 2. These models require that the internal stresses of the granular material be evaluated, however PEPT is only able to measure the kinematic properties of the flow. For this reason, and because of the good

agreement between the DEM simulations (using the lubrication approximation) and PEPT experiments was established, only simulation results are considered in this section. The particle level data was coarsegrained using the method presented in Chapter 4, where the probe positions ere located on a 27×27 grid in the xy-plane that spans $x, y \in [-R, R]$, where the drum radius is $R = 0.2\,\mathrm{m}$. The Gaussian smoothing function was used with a smoothing length 1.5 times the distance between probe points.

The solids fraction ϕ, effective friction μ, inertial number and viscous number,

$$I = \frac{\dot{\gamma} d}{\sqrt{P/\rho_p}} \quad \text{and} \quad J = \frac{\eta_f \dot{\gamma}}{P}\,, \tag{7.5}$$

respectively, were calculated at each probe point. This results in ~ 100 data points per simulation. Data for all figures are binned on the x-axis, with markers representing the average value in a bin and error bars represent the standard deviation.

Results can be compared to model predictions in specific regions in the drum. Probe points in the rising region can be identified as locations where the x and y component of the average velocity is positive, or $\vec{x}$ for which $v_x > 0$ and $v_y > 0$. The flowing layer is the descending region, or where either x or y component is negative, or $\vec{x}$ that satisfy $v_y < 0$ or $v_y < 0$.

7.2.1 Local Viscoplastic

The following model was proposed by Da Cruz et al. [3] and Jop et al. [33]

$$\phi(I) = \phi_c - bI \quad \text{and} \quad \mu(I) = \mu_s + \frac{\mu_2 - \mu_s}{1 + I_0/I}\,, \tag{7.6}$$

where ϕ_c is the maximum volume fraction, μ_s is the friction coefficient at which flow is initiated, μ_2 is the maximum effective friction and b and I_0 are material dependent constants.

Figure 7.3 shows the solids fraction (ϕ) and effective friction (μ) against the inertial number for DEM data. Figure 7.3(a) contains all the points in the mill, Figure 7.3(b) contains all the points in the rising region, Figure 7.3(c) contains all the points in the flowing layer. Using data points in the entire bed, the following values were fitted to the model in equation (7.6) $\phi_c = 0.6009 \pm 0.0006$, $b = 0.429 \pm 0.003$, $\mu_s = 0.366 \pm 0.002$, $\mu_2 = 1.10 \pm 0.01$ and $I_0 = 0.27 \pm 0.01$.

7.2.2 Dense Suspensions

Boyer et al. [5] proposed a model that uses the viscous number as the only dimensionless parameter. Figure 7.4 shows that neither the solids fraction nor effective friction from different viscosities can be described by a single function when plotted against the viscous number. However, in the proposed model it is assumed that the flow is in the viscous regime where $S_t \ll 1$, while the results from this study, discussed in the previous section, shows that $S_t \gg 1$. However, it is observed that

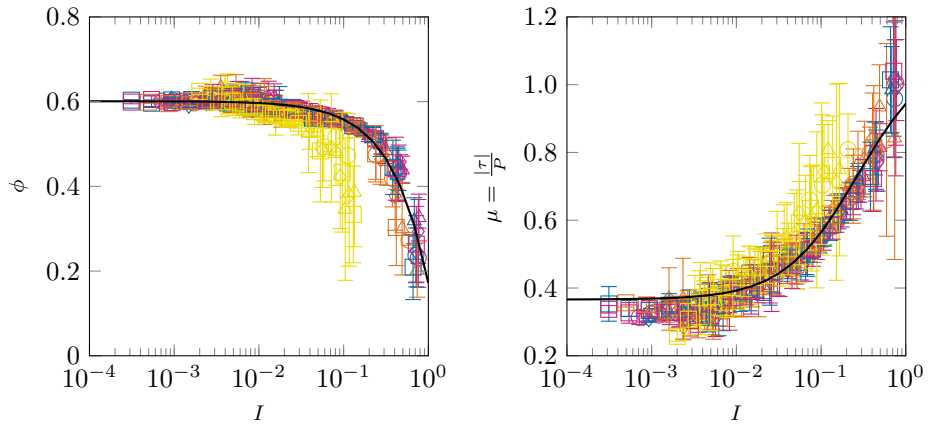

(a)

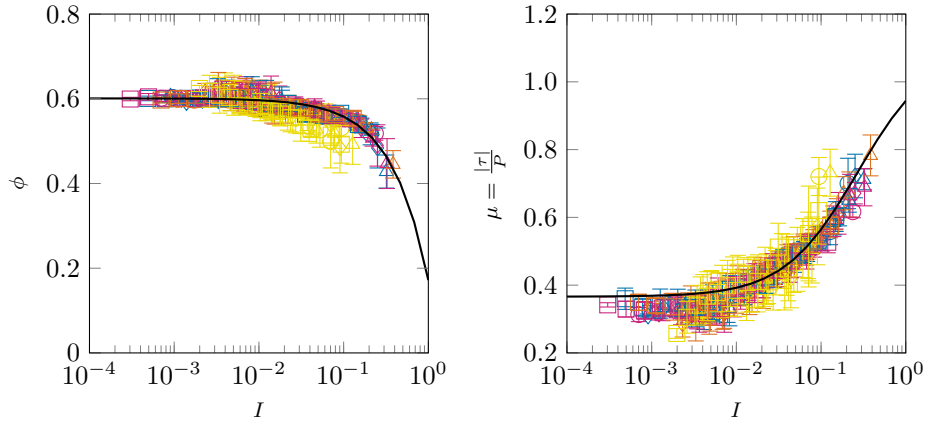

(b)

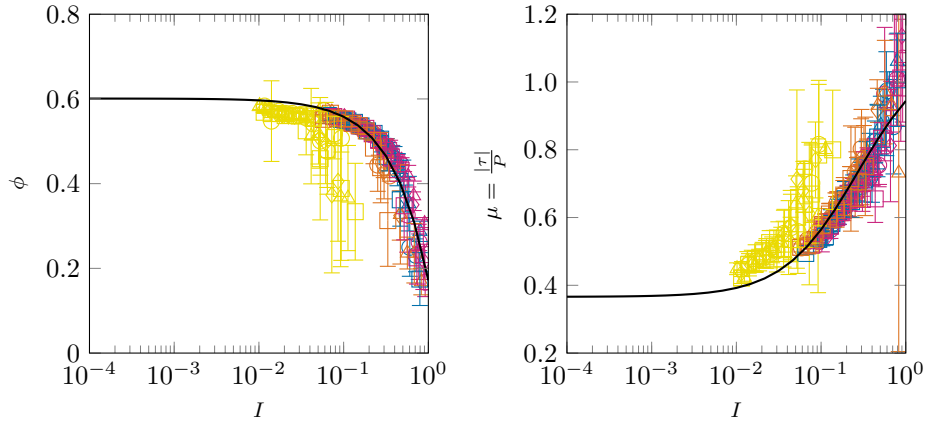

(c)

Figure 7.3 – The solids fraction (ϕ) and effective friction (μ) plotted against the inertial number (I) for (a) the entire drum, (b) the rising region and (c) the flowing layer. The value of ϕ, μ and I was calculated for each coarsegraining location and binned according to I. The markers show the average and standard deviation for each of ϕ and μ, in each bin. The $\mu(I)$ rheology [3, 4], shown in equation (7.6)), was fitted with the data with the following values of each parameter: $\phi_c = 0.6009 \pm 0.0006$, $b = 0.429 \pm 0.003$, $\mu_s = 0.366 \pm 0.002$, $\mu_2 = 1.10 \pm 0.01$ and $I_0 = 0.27 \pm 0.01$.

the behaviour is influenced by the viscosity, since data obtained from simulations performed with different viscosities band together.

The model from Trulsson et al. [6] uses the combined dimensionless parameter $K = I_v + \alpha I^2$ (with $\alpha = 0.635$) which is intended to describe flows in both the inertial and viscous regime. They proposed the following model

$$\phi(K) = \phi_c - b\sqrt{K} \quad \text{and} \quad \mu(K) = \mu_c + \frac{\mu_F - \mu_c}{1 + \sqrt{K_0/K}} \,. \tag{7.7}$$

Figure 7.5 shows the solids fraction (ϕ) and effective friction (μ) against K for DEM data of the entire bed, rising region and flowing layer in Figure 7.5(a), 7.5(b) and 7.5(c), respectively. The model in equation (7.7) was fitted to the data in the bed with the following values to the parameters, $\phi_c = 0.5919 \pm 0.0009$, $b = 0.505 \pm 0.009$, $\mu_c = 0.330 \pm 0.002$, $\mu_F = 0.840 \pm 0.009$ and $\sqrt{K_0} = 0.085 \pm 0.004$.

The model by Boyer et al. [5] takes only the viscous number as a parameter and collapses the data from different speeds, but with the same viscosity. This model could be used to describe the dynamics of tumbling mills, but the viscosity would have to be a second parameter. The description by Trulsson et al. [6], which combines the inertial number and viscous number, produces a much better collapse than the models based on only one of the two parameters. The solids fraction and effective friction is plotted against the dimensionless number proposed by Amarsid et al. [68] in Figure 7.6. The collapse is good, but not noticeably better than in Figure 7.5.

7.2.3 Kinetic Theory

Chialvo and Sundaresan [12] proposed a model that interpolates between the viscoplastic model [3], which has been successful in the dense flow regime, and kinetic theory Garzó and Dufty [11], which works well at the dilute gaseous flows. Their model can be written in terms of a modified inertial number $I' = I/\phi$ and the solids fraction as

$$\mu(I', \phi) = \frac{\beta(\phi)(I')^{5/2} + \alpha I_0^{3/2} I' + I_0^{3/2}\eta_s}{(I')^{3/2} + (I_0)^{3/2}} \,, \tag{7.8}$$

where $\beta(\phi)$ comes from kinetic theory Garzó and Dufty [11] and I', I_0 and α is inspired by Da Cruz et al. [3].

Figure 7.7 shows the effective friction against the modified inertial number. The collapse is surprising given that equation (7.8) has an explicit dependence on ϕ. Figure 7.8 shows the effective friction against the solids fraction for DEM data and model predictions from Jop et al. [4], Trulsson et al. [6], and Chialvo and Sundaresan [12]. While all three models fit the data well at high solids fraction (for instance in the rising region (c)), modified kinetic theory gives better agreement at lower solids fraction in the very dilute part of the flowing layer (b). It should be noted that there are very few probe points in the drum where $\phi < 0.4$. Dilute

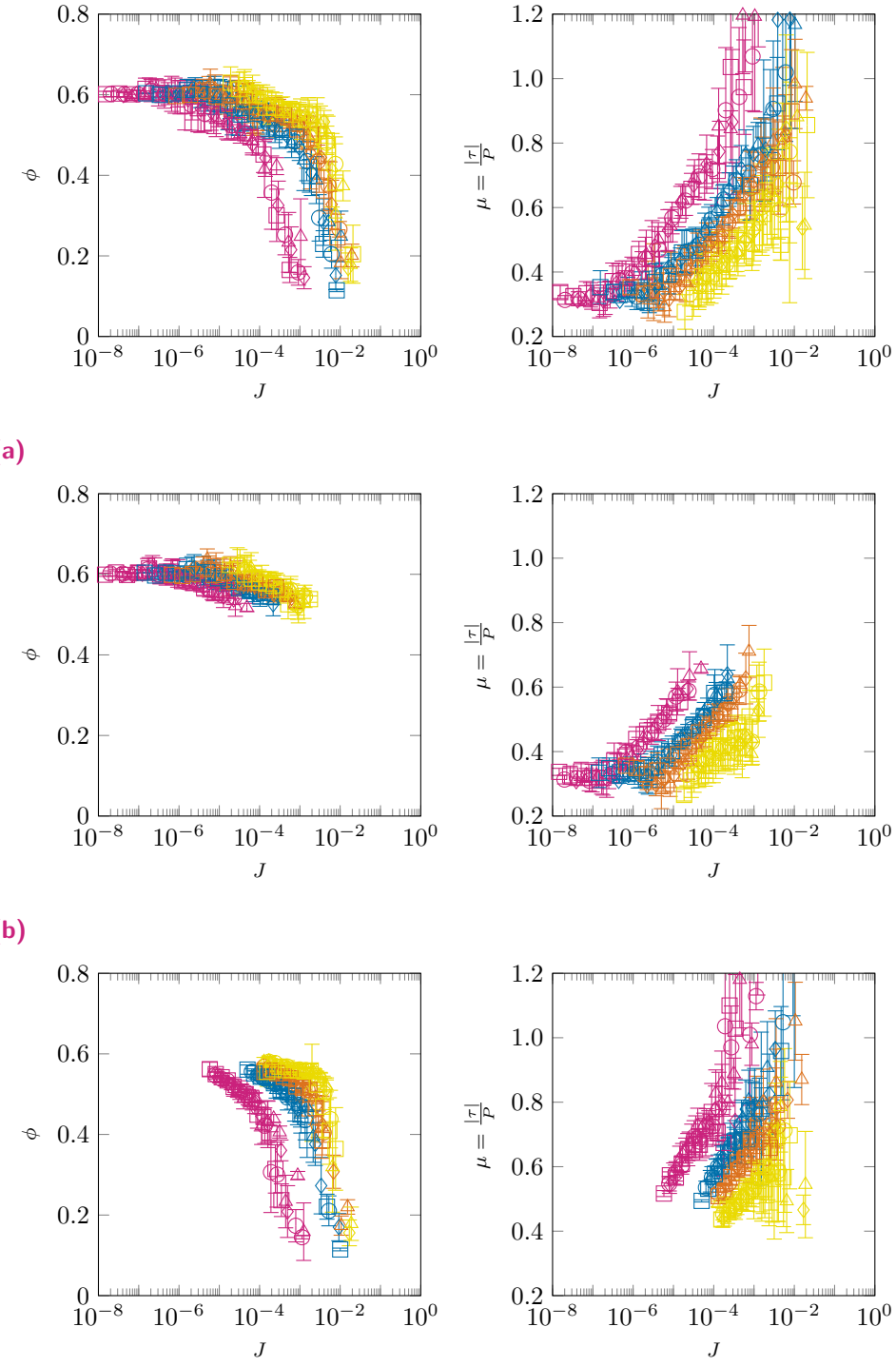

Figure 7.4 – The solids fraction (ϕ) and effective friction (μ) plotted against the viscous number (J) for (a) the entire drum, (b) the rising region and (c) the flowing layer. The rheology by Boyer et al. [5] uses the viscous number as an independent parameter, but a fit was not attempted because the curves for different viscosities do not collapse together. The model was proposed for the viscous Stokes regime ($S_t \ll 1$), and a good fit with the data from this study (where $S_t > 1$) is not expected.

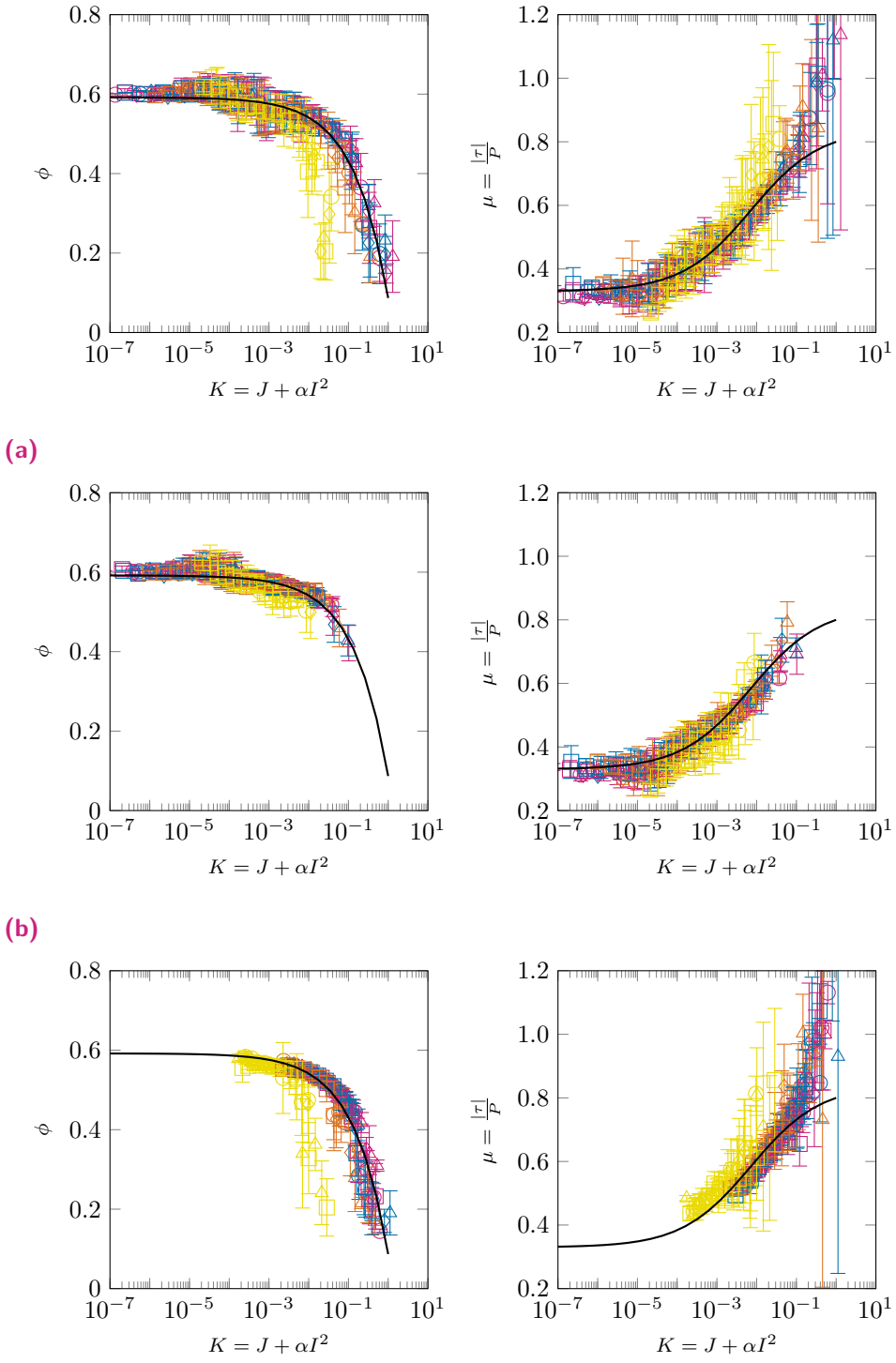

Figure 7.5 – The solids fraction (ϕ) and effective friction (μ) plotted against the combined dimensionless parameter $K = J + \alpha I^2$ (with $\alpha = 0.635$) for (a) the entire drum, (b) the rising region and (c) the flowing layer. The model by Trulsson et al. [6] (equation 7.7) was fitted to the data with $\phi_c = 0.5919 \pm 0.0009$, $b = 0.505 \pm 0.009$, $\mu_c = 0.330 \pm 0.002$, $\mu_F = 0.840 \pm 0.009$ and $\sqrt{K_0} = 0.085 \pm 0.004$.

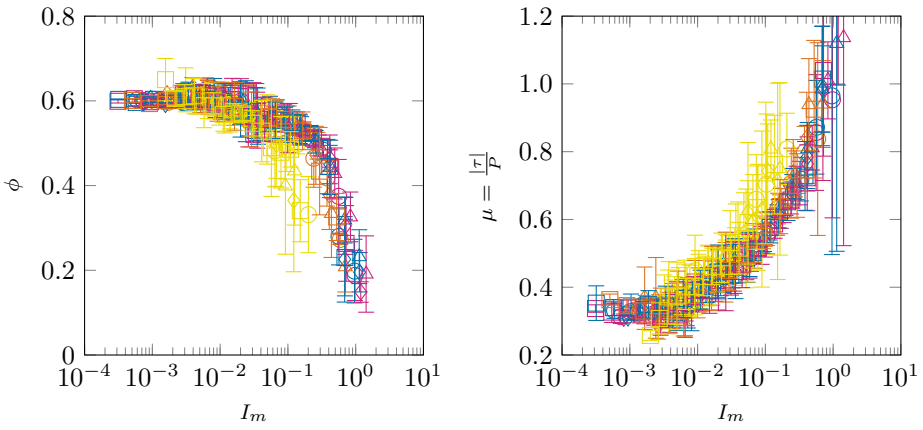

Figure 7.6 – The solids fraction (ϕ) and effective friction (μ) plotted against the modified inertial number $I_m = I\sqrt{1 + 2J/I^2}$ for the entire drum. The collapse is similar to Figure 7.5.

flows, to compare against this model, can be achieved in the flowing layer of rotating drums by increasing the rotation speed.

7.2.4 Non-local Granular Fluidity

Non-local granular fluidity has been discussed in terms of dimensional analysis by Zhang and Kamrin [15], which suggested that

$$g = \frac{\dot{\gamma} P}{\tau} = \frac{\delta v}{d} f(\phi), \tag{7.9}$$

where δv is the fluctuation of the velocity. In this case it is calculated as

$$\delta v = \sqrt{\frac{\sigma^K_{kk}}{3\rho}}\,, \tag{7.10}$$

with σ^K_{kk} the trace of the kinetic stress.

Figure 7.9 (a) shows $gd/\delta v$ against the solids fraction as presented in Zhang and Kamrin [15] and Figure 7.9 (b) shows the same, but as calculated from DEM data for $\omega = 0.4\omega_c$ and $\eta_f = 0.001\,\mathrm{Pa\,s}$ and $\eta_f = 0.01\,\mathrm{Pa\,s}$. Figure 7.9 (c) and Figure 7.9 (d) shows the rising region and flowing layer, respectively. As noted in Zhang and Kamrin [15], the specific value of the asymptote when $\phi \to 0$ may be dependent on particle properties. However, the trend is not as clear as in the results from [15]. The rising region (c), which represents a denser flow, follows the hyperbolic trend closer than the flowing layer (d). While their study used data from uniform shear flow, where the pressure and shear rate was controlled during the course of the simulation, these quantities have to be calculated as emergent properties by coarsegraining particle level information. Variations in shear rate, shear stress, pressure and fluctuations in the velocity propagate to produce substantial fluctuations in $g/\delta v$. It is possible that averaging data over longer simulation times could improve the scatter in the

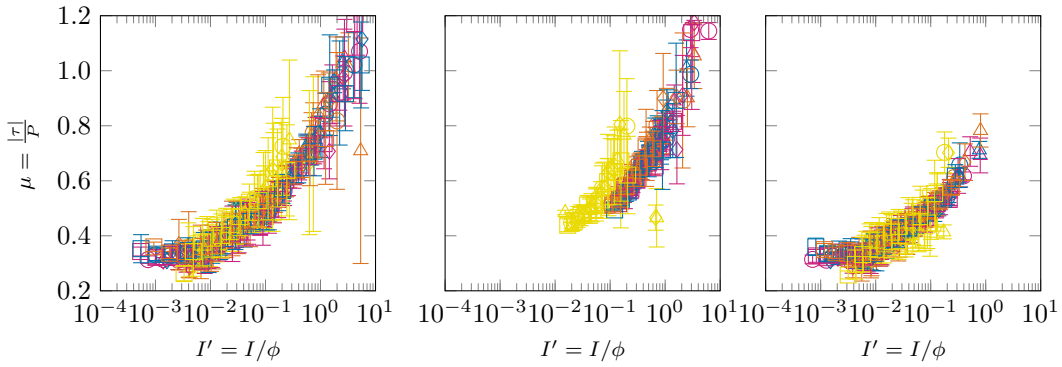

Figure 7.7 – The effective friction vs modified inertial number from Chialvo and Sundaresan [12] for DEM data: (a) the entire bed, (b) the flowing layer, and (c) the rising region. The model for the effective friction (equation (7.8)) is a function of I' and ϕ, but a good collapse is still observed when plotted against I' only.

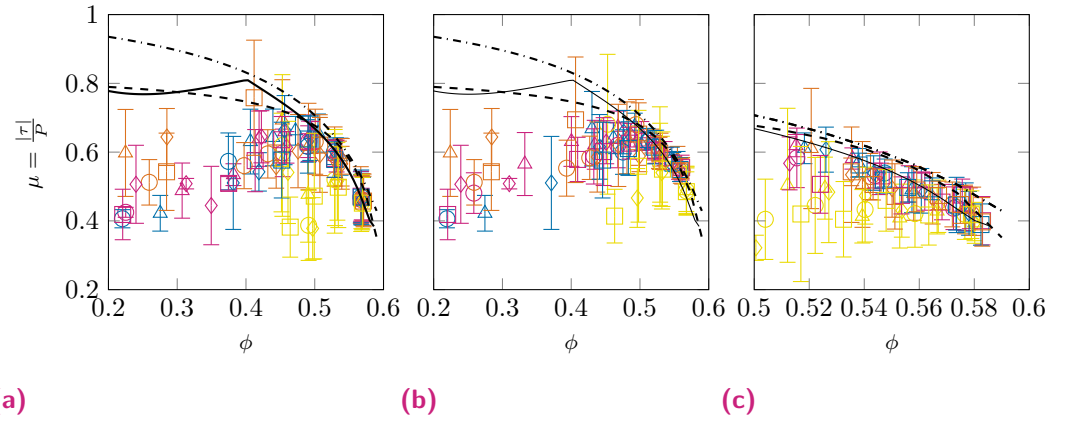

Figure 7.8 – The effective friction vs solids fraction for DEM data with the kinetic theory prediction from Chialvo and Sundaresan [12] (solid), the $\mu(I)$ rheology (dash-dotted) and Trulsson et al. [6] (dashed): (a) the entire bed, (b) the flowing layer, and (c) the rising region.

data, but further investigations of the non-local granular fluidity model as applied to rotating drums will be left as further work.

7.2.5 Discussion

This chapter presented results of dense suspensions in rotating drums simulations (using DEM) and PEPT experiments.

Comparisons of the velocity profiles (Figure 7.1) between simulations and experiments indicate that the lubrication approximation is reproducing the same rheology as in simulation for $\eta_f = 0.011 \pm 0.001$ and $\eta_f = 0.038 \pm 0.005$. However, a large discrepancy is observed for $\eta_f = 0.25 \pm 0.04$.

Figure 7.2 compared the Stokes number between simulations and experiments, and shows that the flow regime is confined to inertial Stokes regime ($S_t > 1$). In this regime the viscous forces between particles are dominated by inter particle collisions. As for the scaled velocity profile, good agreement is observed for $\eta_f = 0.011 \pm 0.001$ and $\eta_f = 0.038 \pm 0.005$ (which corresponds to $S_t > 10$) and a significant difference for $\eta_f = 0.25 \pm 0.04$ ($1 < S_t < 10$).

In this flow regime ($S_t > 10$), numerical simulations of the fluid can be simplified by using the lubrication approximation instead of relying on more direct methods such as SPH-DEM or CFD-DEM coupled simulations. This simplification means:

- time saving in terms of implementing and testing software that communicates between the solids (DEM) and fluid (CFD or SPH) software,
- results that are easier to validate, because the lubrication approximation only adds one additional parameter (the fluid viscosity) that needs to be adjusted, and
- simulations that require less computing resources.

Good agreement was found when comparing DEM results to several of the leading rheology models. The visco-plastic model of dense granular flow (GDR MiDi [2], Da Cruz et al. [3], and Jop et al. [33]) reproduced the same relationships for $\phi(I)$ and $\mu(I)$ that were reported in the literature. Dense granular suspensions models that incorporate both inertial number and viscous number (Trulsson et al. [6] and Amarsid et al. [68]) also produced good results. The viscous number, when used as a single dimensionless parameter as in Boyer et al. [5], does not produce a collapse of the data across different viscosities, however the model was proposed for flows in the viscous Stokes regime and a failure to parameterise flows with $S_t \gg 1$ is not surprising.

The model by Chialvo and Sundaresan [12], which combines ideas from kinetic theory and the visco-plastic $\mu(I)$ rheology shows promise to describe the dilute flow in the flowing layer. It appears that the model can be applied to rotating drums, even though the rheology model does not take fluid effects into account, because the flow regime stays in the inertial Stokes range ($S_t > 10$).

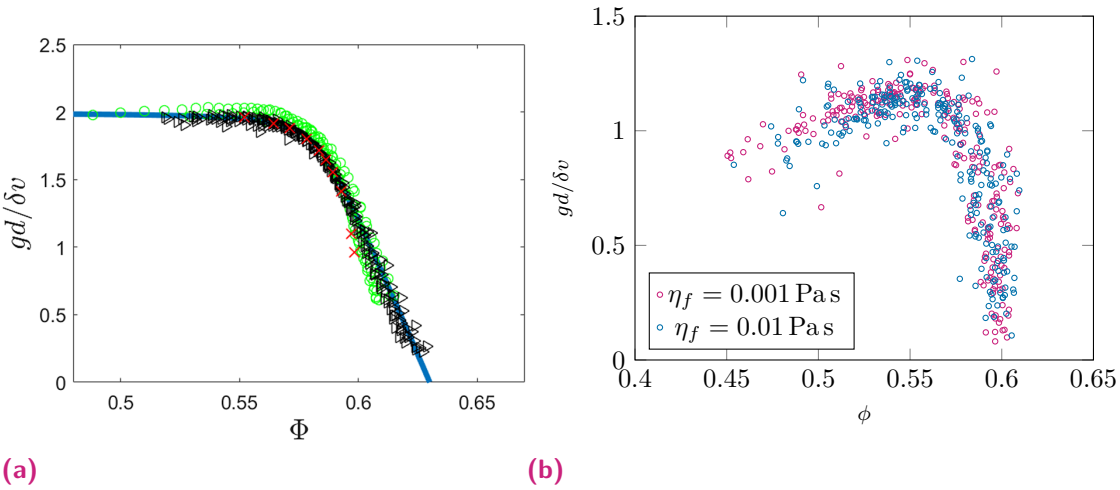

Figure 7.9 – (a) Shows(from Zhang and Kamrin [15]) (b) shows the same plot for Discrete Element Method (DEM) data with $\omega = 0.4\omega_c$ and $\eta_f = \{0.001, 0.01\}$ Pa s. These two configurations were run for 11 s of simulation time and therefore the coarsegraining time average was carried out over the longest interval. Variations in averaged quantities compound when calculating the granular fluidity (equation (7.9)), and only qualitative similarities are seen with results from literature.

Further work is required to make comparisons to non-local granular fluidity (Zhang and Kamrin [15]). The granular fluidity (calculated using equation (7.9)) failed to collapse, because of the compounding of fluctuations in its constituent quantities. However, initial results (Figure 7.9) shows qualitative agreement with the results from Zhang and Kamrin [15]. This model will hopefully give a good description in the dense rising region with more simulation data.

Summary and Conclusion

8

This chapter provides a brief summary of the thesis, presents the main conclusions and possible directions for future investigation.

The three aims of this study were to interrogate the use of the ergodicity when analysing Positron Emission Particle Tracking (PEPT) data, to investigate whether the lubrication approximation can be used effectively to simulate dense suspensions in rotating drums, and to compare the simulation results against the leading rheology models. Two established techniques where employed to study granular suspensions in rotating drums; numerical simulations using the Discrete Element Method (DEM) with the lubrication approximation and experiments using PEPT.

8.1 Summary

DEM simulations of dense granular suspensions in a rotating drum were carried out using the open source LIGGGHTS package. The lubrication approximation was used to simulate the effect of a fluid between particles. The drum was kept in the cascading Froude regime by using rates of rotation between $0.3\omega_c$ to $0.6\omega_c$ (with $\omega_c = \sqrt{g/R}$) in increments of $0.05\omega_c$. DEM results give access to dynamic quantities, in particular inter-particle forces, that are unattainable for PEPT and most other experimental techniques.

DEM results were coarsegrained using the method from Glasser and Goldhirsch [52], Babic [53], and Artoni and Richard [54]. The continuum quantities are calculated from an average over all particles and time steps, and this produces the continuum quantities used in further analysis. The internal forces of the bulk material, the kinetic and contact stress, can be calculated from dynamic particle level quantities such as the fluctuation of the bulk velocity and inter-particle forces. By choosing the Gaussian kernel function, gradients of the velocity, or the deformation rate, can also be calculated.

PEPT experiments of dense granular suspensions and dense granular flows were carried out. Two configurations were used: Three separate particle sizes of $5\,\mathrm{mm}$, $8\,\mathrm{mm}$ and $10\,\mathrm{mm}$ mono-disperse glass beads with no fluid This series of experiments was performed with the aim of testing the ergodic hypothesis. Particle tracking was carried out over $10\,\mathrm{h}$ for each of the particle sizes at $0.6\omega_c = 0.6\sqrt{g/R}$. The second configuration used $10\,\mathrm{mm}$ glass beads. A glycerol/water mixture was added in addition to the beads, and 3 viscosities ($\eta_f = \{0.011 \pm 0.001, 0.038 \pm 0.005, 0.25 \pm 0.04\}\mathrm{Pa\,s}$) were achieved by varying the ratio of water-to-glycerol. The fluid viscosity was quantified using the parametrisation of water/glycerol viscosity by Cheng [129], and independent measurements were made with a viscometer.

The ergodic hypothesis, which assumes that the average behaviour of a single particle is equal to the average behaviour of the ensemble over long time intervals, is required to coarsegrain data from the PEPT tracer. Effects of the experimental setup that could interfere with the triangulation scheme – such as the Nyquist frequency and γ-scattering and absorption – were considered. Methods used when analysing dynamical systems such as Poincaré maps and the global mixing index (Doucet et al. [108, 109]) were used to investigate the motion of the tracer particle.
Comparisons between DEM and PEPT experiments were made by examining the scaling of velocity profiles in the flowing layer and the Stokes number in various regions of the drum. In addition, quantitative comparisons were made between some of the latest rheology models, in particular, the visco plastic $\mu(I)$ rheology, dense suspension extension by Trulsson et al. [6] and Amarsid et al. [68], the dense extension to Kinetic Theory (KT) by Chialvo and Sundaresan [12] and the non-local granular fluidity theory Zhang and Kamrin [15].

8.2 Conclusions

The main conclusions from this work are:

- From the tests for ergodicity it was found that the bulk velocity is measured consistently over many segments of $15\,\mathrm{min}$ tracking time. However, the solids fraction requires significantly longer tracking time before consistent values are recorded and even after a $3\,\mathrm{h}$ tracking period the region near the Center of Circulation (CoC) remains under sampled. Some aspects of the PEPT technique, such as γ-ray absorption or a sample rate that is less than the Nyquist frequency, were ruled out as possible causes for poor sampling of the tracer's position. Indeed, when the dynamics of the drum charge were analysed using Poincaré maps and the global mixing index, it was found that the dynamics pushes the tracer away from the CoC. This limitation can be overcome to some extent by choosing an averaging volume that is dependent on the average charge speed.

- The lubrication approximation can be successfully used to simulate granular suspensions in rotating drums for fluid viscosity of up to $\eta_f = 0.03\,\mathrm{Pa\,s}$, which in this study, corresponds to a Stokes number $S_t > 10$. However, this method does not produce results comparable to PEPT experiments for $\eta_f = 0.22\,\mathrm{Pa\,s}$ (or $S_t < 10$).

- Rheological models compared to the DEM data showed good agreement for the $\mu(I)$ rheology, the dense suspension rheology from Trulsson et al. [6] and Amarsid et al. [68] and the extension to KT (Chialvo and Sundaresan [12]). A wide range of flow regimes are spanned in the dense flowing regime, which can be quantified by the range of inertial numbers observed in the drum, compared to results from configurations in other studies. Some scatter exists in the results which might be alleviated if simulations are run for longer, however

this could also be attributed to the chaotic nature of flows in rotating drums. The model from Zhang and Kamrin [15] could not be satisfactorily tested because of compounding effects of uncertainties when calculating the granular temperature, but results do show some qualitative agreement.

8.3 Future work

Future work may include:

- Poincaré maps can be useful to investigate mixing and segregation phenomena in rotating drums.
- Techniques to correct the solids fraction could be designed to compensate for over and under sampled regions in the mill, however this would require a better understanding of the axial dynamics of the tracer particle.
- Applications of the lubrication approximation could be improved by implementing particle-wall interactions. Additional forces like drag forces could also be applied. Both of these additions may extend this numerical approach to lower Stokes regimes.
- The lubrication approximation can be used to investigate application of rotating drums in industrial settings, such as tumbling mills.

References

[1] H. M. Jaeger, S. R. Nagel, and R. P. Behringer, "Granular solids, liquids, and gases", Reviews of Modern Physics **68**, 1259–1273 (1996) (cit. on pp. 1, 6).

[2] GDR MiDi, "On dense granular flows." The European physical journal. E, Soft matter **14**, 341–365 (2004) (cit. on pp. 1, 2, 9, 11, 15, 22, 23, 90).

[3] F. Da Cruz, S. Emam, M. Prochnow, J.-N. Roux, and F. Chevoir, "Rheophysics of dense granular materials : Discrete simulation of plane shear flows", Physical Review E **72**, 021309 (2005) (cit. on pp. 1, 6, 10, 13, 83–85, 90).

[4] P. Jop, Y. Forterre, and O. Pouliquen, "A constitutive law for dense granular flows", Nature **441**, 727–730 (2006) (cit. on pp. 1, 11, 84, 85).

[5] F. Boyer, É. Guazzelli, and O. Pouliquen, "Unifying suspension and granular rheology." Physical review letters **107**, 188301 (2011) (cit. on pp. 1, 3, 12, 13, 22, 83, 85, 86, 90).

[6] M. Trulsson, B. Andreotti, and P. Claudin, "Transition from the viscous to inertial regime in dense suspensions." Physical review letters **109**, 118305 (2012) (cit. on pp. 1–3, 13, 21, 23, 49, 85, 87, 89, 90, 94).

[7] S. Courrech du Pont, P. Gondret, B. Perrin, and M. Rabaud, "Granular Avalanches in Fluids", Physical Review Letters **90**, 044301 (2003) (cit. on pp. 1, 12, 22, 81).

[8] C. K. Lun, S. B. Savage, D. J. Jeffrey, and N. Chepurniy, "Kinetic theories for granular flow: Inelastic particles in Couette flow and slightly inelastic particles in a general flowfield", Journal of Fluid Mechanics **140**, 223–256 (1984) (cit. on pp. 1, 13).

[9] J. T. Jenkins and S. B. Savage, "A theory for the rapid flow of identical, smooth, nearly elastic, spherical particles", English, Journal of Fluid Mechanics **130**, 187–202 (1983) (cit. on pp. 1, 13).

[10] J. T. Jenkins and M. W. Richman, "Kinetic theory for plane flows of a dense gas of identical, rough, inelastic, circular disks", Physics of Fluids **28**, 3485 (1985) (cit. on pp. 1, 13).

[11] V. Garzó and J. W. Dufty, "Dense fluid transport for inelastic hard spheres", Physical Review E **59**, 5895–5911 (1999) (cit. on pp. 1, 13, 14, 85).

[12] S. Chialvo and S. Sundaresan, "A modified kinetic theory for frictional granular flows in dense and dilute regimes", Physics of Fluids **25**, 070603 (2013) (cit. on pp. 1, 3, 14, 85, 89, 90, 94).

[13] K. Kamrin and G. Koval, "Nonlocal Constitutive Relation for Steady Granular Flow", Physical Review Letters **108**, 178301 (2012) (cit. on pp. 1, 3, 15).

[14] D. L. Henann and K. Kamrin, "A predictive, size-dependent continuum model for dense granular flows." Proceedings of the National Academy of Sciences of the United States of America **110**, 6730–5 (2013) (cit. on pp. 1, 3, 15).

[15] Q. Zhang and K. Kamrin, "A Microscopic Description of the Granular Fluidity Field in Nonlocal Flow Modeling", Physical Review Letters **118**, 058001 (2016) (cit. on pp. 1, 3, 15, 16, 88, 91, 94, 95).

[16] M. Bouzid, M. Trulsson, P. Claudin, E. Clément, and B. Andreotti, "Nonlocal Rheology of Granular Flows across Yield Conditions", Physical Review Letters **111**, 238301 (2013) (cit. on pp. 1, 15).

[17] M. Bouzid, A. Izzet, M. Trulsson, et al., "Non-local rheology in dense granular flows", The European Physical Journal E **38**, 125 (2015) (cit. on pp. 1, 15).

[18] M. Powell and A. McBride, "A three-dimensional analysis of media motion and grinding regions in mills", Minerals Engineering **17**, 1099–1109 (2004) (cit. on p. 2).

[19] A. Morrison, I. Govender, A. Mainza, and D. Parker, "The shape and behaviour of a granular bed in a rotating drum using Eulerian flow fields obtained from PEPT", Chemical Engineering Science **152**, 186–198 (2016) (cit. on pp. 2, 19).

[20] I Govender and T Pathmathas, "A positron emission particle tracking investigation of the flow regimes in tumbling mills", Journal of Physics D: Applied Physics **50**, 35601 (2017) (cit. on pp. 2, 19).

[21] J Rajchenbach, "Flow in Powders: From Discrete Avalanches to Continuous Regime", Physical Review Letters **65**, 2221–2225 (1990) (cit. on p. 2).

[22] O Zik, D Levine, S. G. Lipson, S Shtrikman, and J Stavans, "Rotational Induced Segregation of Granular Materials", Physical Review Letters **73**, 644–649 (1994) (cit. on p. 2).

[23] A. Orpe and D. Khakhar, "Scaling relations for granular flow in quasi-two-dimensional rotating cylinders", Physical Review E **64**, 1–13 (2001) (cit. on pp. 2, 7, 11, 16, 23).

[24] N. Taberlet, P. Richard, and E. John Hinch, "The S Shape of a granular pile in a rotating drum", Physical Review E **73**, 050301 (2006) (cit. on pp. 2, 7).

[25] H.-T. Chou and C.-F. Lee, "Cross-sectional and axial flow characteristics of dry granular material in rotating drums", Granular Matter **11**, 13–32 (2009) (cit. on pp. 2, 11, 16, 23).

[26] F. Pignatel, C. Asselin, L. Krieger, et al., "Parameters and scalings for dry and immersed granular flowing layers in rotating tumblers", Physical Review E **86**, 011304 (2012) (cit. on pp. 2, 11, 23).

[27] I. Govender, M. C. Richter, A. N. Mainza, and D. N. De Klerk, "A positron emission particle tracking investigation of the scaling law governing free surface flows in tumbling mills", AIChE Journal **63**, 903–913 (2017) (cit. on pp. 2, 11, 19, 27, 51, 62).

[28] P.-P. Cortet, D. Bonamy, F. Daviaud, et al., "Relevance of visco-plastic theory in a multi-directional inhomogeneous granular flow", EPL (Europhysics Letters) **88**, 14001 (2009) (cit. on pp. 2, 11, 38).

[29] M. Hawkesworth, M. O'Dwyer, J. Walker, et al., "A positron camera for industrial application", Nuclear Instruments and Methods in Physics Research Section A: Accelerators, Spectrometers, Detectors and Associated Equipment **253**, 145–157 (1986) (cit. on pp. 2, 16).

[30] C. Bemrose, P. Fowles, M. Hawkesworth, and M. O'Dwyer, "Application of positron emission tomography to particulate flow measurement in chemical engineering processes", Nuclear Instruments and Methods in Physics Research Section A: Accelerators, Spectrometers, Detectors and Associated Equipment **273**, 874–880 (1988) (cit. on pp. 2, 16).

[31] D. Parker, C. Broadbent, P. Fowles, M. Hawkesworth, and P. McNeil, "Positron emission particle tracking - a technique for studying flow within engineering equipment", Nuclear Instruments and Methods in Physics Research Section A: Accelerators, Spectrometers, Detectors and Associated Equipment **326**, 592–607 (1993) (cit. on pp. 2, 16, 52, 53).

[32] R. D. Wildmann, J. M. Huntley, J.-P. Hansen, D. J. Parker, and D. A. Allen, "Single-particle motion in three dimensional vibrofluidised beds", Phys. Rev. E **62**, 3826–3835 (2000) (cit. on pp. 2, 3, 18, 43, 63, 67).

[33] P. Jop, Y. Forterre, and O. Pouliquen, "Crucial role of sidewalls in granular surface flows: consequences for the rheology", English, Journal of Fluid Mechanics **541**, 167 (2005) (cit. on pp. 2, 10, 80, 83, 90).

[34] P. A. Cundall and O. D. L. Strack, "A discreate numerical model for granular assemblies", Geotechnique **29**, 47–65 (1979) (cit. on pp. 2, 20, 23).

[35] R. Sun and H. Xiao, "SediFoam: A general-purpose, open-source CFD–DEM solver for particle-laden flow with emphasis on sediment transport", Computers & Geosciences **89**, 207–219 (2016) (cit. on pp. 2, 20, 21).

[36] M. Malahe, "A one-way coupled DEM-CFD scheme to mode free-surface flows in tumbling mills", Masters Thesis (University of Cape Town, 2012) (cit. on pp. 2, 20).

[37] H. Xiao and J. Sun, “Algorithms in a Robust Hybrid CFD-DEM Solver for Particle-Laden Flows”, Communications in Computational Physics **9**, 297–323 (2011) (cit. on pp. 2, 20).

[38] C. Kloss, C. Goniva, A. Hager, S. Amberger, and S. Pirker, “Models, algorithms and validation for opensource DEM and CFD-DEM”, Progress in Computational Fluid Dynamics, An International Journal **12**, 140 (2012) (cit. on pp. 2, 20, 23).

[39] H. H. Hu, D. D. Joseph, and M. J. Crochet, “Direct simulation of fluid particle motions”, Theoretical and Computational Fluid Dynamics **3**, 285–306 (1992) (cit. on pp. 2, 20).

[40] P. W. Cleary, R. D. Morrison, and G. W. Delaney, “Incremental damage and particle size reduction in a pilot SAG mill: DEM breakage method extension and validation”, Minerals Engineering **128**, 56–68 (2018) (cit. on pp. 2, 21).

[41] P. W. Cleary, G. W. Delaney, M. D. Sinnott, and R. D. Morrison, “Inclusion of incremental damage breakage of particles and slurry rheology into a particle scale multiphase model of a SAG mill”, Minerals Engineering **128**, 92–105 (2018) (cit. on pp. 2, 21).

[42] R. Cox, “The motion of suspended particles almost in contact”, International Journal of Multiphase Flow **1**, 343–371 (1974) (cit. on pp. 2, 21, 26).

[43] S. Kim and S. J. Karrila, “Microhydrodynamics” (Butterworth-Heinemann, 1991) (cit. on pp. 2, 21).

[44] R. C. Ball and J. R. Melrose, “A simulation technique for many spheres in quasi-static motion under frame-invariant pair drag and Brownian forces”, Physica A: Statistical Mechanics and its Applications **347**, 444–472 (1997) (cit. on pp. 2, 21, 26).

[45] R. Seto, R. Mari, J. F. Morris, and M. M. Denn, “Discontinuous shear thickening of frictional hard-sphere suspensions.” Physical review letters **111**, 218301 (2013) (cit. on pp. 2, 3, 21, 23, 49).

[46] C. Ness and J. Sun, “Flow regime transitions in dense non-Brownian suspensions: Rheology, microstructural characterization, and constitutive modeling”, Physical Review E **91**, 12201 (2015) (cit. on pp. 2, 3, 13, 21, 23, 26, 41, 49).

[47] C. Ness and J. Sun, “Shear thickening regimes of dense non-Brownian suspensions”, Soft Matter **12**, 914–924 (2016) (cit. on pp. 2, 13, 21, 23).

[48] T. S. Majmudar and R. P. Behringer, “Contact force measurements and stress-induced anisotropy in granular materials”, Nature **435**, 1079–1082 (2005) (cit. on p. 5).

[49] J. Geng, D. Howell, E. Longhi, et al., "Footprints in Sand: The Response of a Granular Material to Local Perturbations", Physical Review Letters **87**, 035506 (2001) (cit. on p. 5).

[50] C. H. Rycroft, K. Kamrin, and M. Z. Bazant, "Assessing continuum postulates in simulations of granular flow", Journal of the Mechanics and Physics of Solids **57**, 828–839 (2009) (cit. on pp. 5, 6, 11, 41).

[51] C. Goldenberg and I. Goldhirsch, "Friction enhances elasticity in granular solids", Nature **435**, 188–191 (2005) (cit. on pp. 5, 22).

[52] B. J. Glasser and I Goldhirsch, "Scale dependence, correlations, and fluctuations of ststress in rapid granular flows", Physics of Fluids **13**, 407–420 (2001) (cit. on pp. 5, 6, 33, 93).

[53] M. Babic, "Average balance equations for granular materials", International Journal of Engineering Science **35**, 523–548 (1997) (cit. on pp. 5, 6, 22, 33, 34, 93).

[54] R. Artoni and P. Richard, "Average balance equations, scale dependence, and energy cascade for granular materials", Physical Review E **91**, 032202 (2015) (cit. on pp. 5, 6, 20, 22, 33, 35, 93).

[55] H Henein, J. K. Brimacombe, and A. P. Watkinson, "Experimental Studies of Transverse Bed Motion in Rotary Kilns", Metallurgical Transactions B **14**, 191–205 (1983) (cit. on pp. 6, 8).

[56] J Mellmann, "The transverse motion of solids in rotating cylinders-forms of motion and transition behavior", Powder Technology **118**, 251–270 (2001) (cit. on pp. 6, 8, 23).

[57] G. I. Barenblatt, "Scaling" (Cambridge University Press, Cambridge, 2003) (cit. on p. 7).

[58] R. A. Bagnold, "Experiments on a Gravity-Free Dispersion of Large Solid Spheres in a Newtonian Fluid under Shear", Proceedings of the Royal Society A: Mathematical, Physical and Engineering Sciences **225**, 49–63 (1954) (cit. on p. 8).

[59] R. A. Bagnold, "The Flow of Cohesionless Grains in Fluids", Philosophical Transactions of the Royal Society A: Mathematical, Physical and Engineering Sciences **249**, 235–297 (1956) (cit. on p. 8).

[60] C. S. Campbell, "Rapid Granular Flows", Annual Review of Fluid Mechanics **22**, 57–90 (1990) (cit. on p. 9).

[61] M. L. Hunt, R. Zenit, C. S. Campbell, and C. E. Brennen, "Revisiting the 1954 suspension experiments of R. A. Bagnold", Journal of Fluid Mechanics **452**, 1–24 (2002) (cit. on p. 9).

[62] V. Kumaran, "Kinetic theory for sheared granular flows", Comptes Rendus Physique **16**, 51–61 (2015) (cit. on pp. 9, 14).

[63] O. Pouliquen, “Scaling laws in granular flows down rough inclined planes”, Physics of Fluids **11**, 542 (1999) (cit. on p. 10).

[64] Y. Forterre and O. Pouliquen, “Flows of Dense Granular Media”, Annual Review of Fluid Mechanics **40**, 1–24 (2008) (cit. on p. 10).

[65] B. Andreotti, Y. Forterre, and O. Pouliquen, “Granular Media” (Cambridge University Press, 2013) (cit. on pp. 10, 75).

[66] L. Lacaze and R. R. Kerswell, “Axisymmetric granular collapse : a transient 3D flow test of visco-plasticity”, Phys. Rev. Lett. **102**, 108305 (2009) (cit. on p. 11).

[67] C. Cassar, M. Nicolas, and O. Pouliquen, “Submarine granular flows down inclined planes”, Physics of Fluids **17**, 103301 (2005) (cit. on p. 12).

[68] L. Amarsid, J.-Y. Delenne, P. Mutabaruka, et al., “Viscoinertial regime of immersed granular flows”, Physical Review E **96**, 012901 (2017) (cit. on pp. 12, 13, 85, 90, 94).

[69] J. J. Stickel and R. L. Powell, “Fluid Mechanics and Rheology of Dense Suspensions”, Annual Review of Fluid Mechanics **37**, 129–149 (2005) (cit. on p. 12).

[70] A Lemaitre, J Roux, and F Chevoir, “What do dry granular flows tell us about dense non-{B}rownian suspension Rheology”, Rheologica Acta **48 (8)**, 925–942 (2009) (cit. on p. 13).

[71] M. Houssais, C. P. Ortiz, D. J. Durian, and D. J. Jerolmack, “Onset of sediment transport is a continuous transition driven by fluid shear and granular creep”, Nature Communications **6**, 6527 (2015) (cit. on p. 13).

[72] M. Houssais, C. P. Ortiz, D. J. Durian, and D. J. Jerolmack, “Rheology of sediment transported by a laminar flow”, Physical Review E **94**, 062609 (2016) (cit. on p. 13).

[73] M. Houssais and D. J. Jerolmack, “Toward a unifying constitutive relation for sediment transport across environments”, Geomorphology **277**, 251–264 (2017) (cit. on p. 13).

[74] R. Maurin, J. Chauchat, and P. Frey, “Dense granular flow rheology in turbulent bedload transport”, Journal of Fluid Mechanics **804**, 490–512 (2016) (cit. on p. 13).

[75] V. Kumaran, “The constitutive relation for the granular flow of rough particles, and its application to the flow down an inclined plane”, Journal of Fluid Mechanics **561**, 1 (2006) (cit. on p. 14).

[76] C. K. K. Lun, “Kinetic theory for granular flow of dense, slightly inelastic, slightly rough spheres”, Journal of Fluid Mechanics **233**, 539 (1991) (cit. on p. 14).

[77] J. T. Jenkins and C. Zhang, "Kinetic theory for identical, frictional, nearly elastic spheres", Physics of Fluids **14**, 1228–1235 (2002) (cit. on p. 14).

[78] V. Garzó, S. Tenneti, S. Subramaniam, and C. M. Hrenya, "Enskog kinetic theory for monodisperse gas-solid flows", Journal of Fluid Mechanics **712**, 129–168 (2012) (cit. on p. 14).

[79] M. G. Chamorro, F. V. Reyes, and V. Garzó, "Non-Newtonian hydrodynamics for a dilute granular suspension under uniform shear flow", Physical Review E **92**, 052205 (2015) (cit. on p. 14).

[80] S. Saha and M. Alam, "Revisiting ignited-quenched transition and the non-Newtonian rheology of a sheared dilute gas-solid suspension", Journal of Fluid Mechanics **833**, 206–246 (2017) (cit. on p. 14).

[81] J. T. Jenkins and D. Berzi, "Dense inclined flows of inelastic spheres: tests of an extension of kinetic theory", Granular Matter **12**, 151–158 (2010) (cit. on p. 14).

[82] J. T. Jenkins, "Dense inclined flows of inelastic spheres", Granular Matter **10**, 47–52 (2007) (cit. on p. 14).

[83] J. T. Jenkins, "Dense shearing flows of inelastic disks", Physics of Fluids **18**, 103307 (2006) (cit. on p. 14).

[84] D. Berzi and D. Vescovi, "Different singularities in the functions of extended kinetic theory at the origin of the yield stress in granular flows", Physics of Fluids **27**, 013302 (2015) (cit. on p. 14).

[85] D. Vescovi, D. Berzi, P. Richard, and N. Brodu, "Plane shear flows of frictionless spheres: Kinetic theory and 3D soft-sphere discrete element method simulations", Physics of Fluids **26**, 053305 (2014) (cit. on p. 14).

[86] L. E. Silbert, J. W. Landry, and G. S. Grest, "Granular flow down a rough inclined plane: Transition between thin and thick piles", Physics of Fluids **15**, 1–10 (2003) (cit. on p. 15).

[87] F. Da Cruz, F. Chevoir, D. Bonn, and P. Coussot, "Viscosity bifurcation in granular materials, foams, and emulsions", Physical Review E **66**, 051305 (2002) (cit. on p. 15).

[88] G. Koval, J.-N. Roux, A. Corfdir, and F. Chevoir, "Annular shear of cohesionless granular materials: From the inertial to quasistatic regime", Physical Review E **79**, 021306 (2009) (cit. on p. 15).

[89] K. a. Reddy, Y. Forterre, and O. Pouliquen, "Evidence of Mechanically Activated Processes in Slow Granular Flows", Physical Review Letters **106**, 108301 (2011) (cit. on p. 15).

[90] K. Nichol, A. Zanin, R. Bastien, E. Wandersman, and M. V. Hecke, "Flow-Induced Agitations Create a Granular Fluid", **078302**, 48–51 (2010) (cit. on p. 15).

[91] J. Goyon, A. Colin, G. Ovarlez, A. Ajdari, and L. Bocquet, "Spatial cooperativity in soft glassy flows", Nature **454**, 84–87 (2008) (cit. on p. 15).

[92] L. Bocquet, A. Colin, and A. Ajdari, "Kinetic Theory of Plastic Flow in Soft Glassy Materials", Physical Review Letters **103**, 036001 (2009) (cit. on p. 15).

[93] A. Bhateja and D. V. Khakhar, "Rheology of dense granular flows in two dimensions: Comparison of fully two-dimensional flows to unidirectional shear flow", Physical Review Fluids **3**, 062301 (2018) (cit. on p. 16).

[94] S Morrell, "The Prediction of Power Draw in Wet Tumbling Mills", Doctoral Thesis (University of Queensland, 1993) (cit. on p. 16).

[95] A. C. Santomaso, Y. L. Ding, J. R. Lickiss, and D. W. York, "Investigation of the granular behaviour in a rotating drum operated over a wide range of rotational speed", Transactions of the Institute of Chemical Engineers **81**, 936–945 (2003) (cit. on p. 16).

[96] A. V. Orpe and D. V. Khakhar, "Rheology of surface granular flows", Journal of Fluid Mechanics **571**, 1 (2007) (cit. on p. 16).

[97] N. Jain, J. M. Ottino, and R. M. Lueptow, "An experimental study of the flowing granular layer in a rotating tumbler", Physics of Fluids **14**, 572 (2002) (cit. on p. 16).

[98] N. Jain, J. M. Ottino, and R. M. Lueptow, "Effect of interstitial fluid on a granular flowing layer", Journal of Fluid Mechanics **508**, 23–44 (2004) (cit. on p. 16).

[99] M Nakagawa, S. A. Altobelli, A Caprihan, E Fukushima, and E. K. Jeong, "Non-invasive Measurements of Granular Flows by Magnetic Resonance Imaging", Experiments in Fluids **16**, 54–60 (1993) (cit. on p. 16).

[100] T. Volkwyn, A. Buffler, I. Govender, et al., "Studies of the effect of tracer activity on time-averaged positron emission particle tracking measurements on tumbling mills at PEPT Cape Town", Minerals Engineering **24**, 261–266 (2011) (cit. on pp. 17, 53).

[101] D. Parker, A. Dijkstra, T. Martin, and J. Seville, "Positron emission particle tracking studies of spherical particle motion in rotating drums", Chemical Engineering Science **52**, 2011–2022 (1997) (cit. on pp. 17, 19).

[102] D. Blakemore, "Multiple Particle Tracking in PEPT using Voronoi Tessellations", Masters Thesis (University of Cape Town, 2016) (cit. on p. 17).

[103] M. Bickell, A. Buffler, I. Govender, and D. J. Parker, "A new line density tracking algorithm for PEPT and its application to multiple tracers", Nuclear Instruments and Methods in Physics Research, Section A: Accelerators, Spectrometers, Detectors and Associated Equipment **682**, 36–41 (2012) (cit. on p. 17).

[104] Z. Yang, P. J. Fryer, S. Bakalis, et al., "An improved algorithm for tracking multiple, freely moving particles in a Positron Emission Particle Tracking system", Nuclear Instruments and Methods in Physics Research, Section A: Accelerators, Spectrometers, Detectors and Associated Equipment **577**, 585–594 (2007) (cit. on p. 17).

[105] O. Gundogdu, "Positron Emission Tomography Particle tracking using cluster analysis", Nuclear Instruments and Methods in Physics Research Section A: Accelerators, Spectrometers, Detectors and Associated Equipment **534**, 562–576 (2004) (cit. on p. 17).

[106] J. Eckmann and D. Ruelle, "Ergodic theory of chaos and strange attractors", Reviews of Modern Physics **57**, 617–656 (1985) (cit. on p. 18).

[107] K. M. Hill, D. V. Khakhar, J. F. Gilchrist, J. J. McCarthy, and J. M. Ottino, "Segregation-driven organization in chaotic granular flows." Proceedings of the National Academy of Sciences of the United States of America **96**, 11701–6 (1999) (cit. on pp. 18, 67, 71).

[108] J. Doucet, F. Bertrand, and J. Chaouki, "Experimental characterization of the chaotic dynamics of cohesionless particles: application to a V-blender", Granular Matter **10**, 133–138 (2008) (cit. on pp. 19, 67, 71, 73, 94).

[109] J. Doucet, F. Bertrand, and J. Chaouki, "A measure of mixing from Lagrangian tracking and its application to granular and fluid flow systems", Chemical Engineering Research and Design **86**, 1313–1321 (2008) (cit. on pp. 19, 67, 94).

[110] L. Bbosa, I. Govender, and A. Mainza, "Development of a novel methodology to determine mill power draw", International Journal of Mineral Processing **149**, 94–103 (2016) (cit. on p. 19).

[111] L. Bbosa, I. Govender, A. Mainza, and M. Powell, "Power draw estimations in experimental tumbling mills using PEPT", Minerals Engineering **24**, 319–324 (2011) (cit. on p. 19).

[112] K. Sichalwe, I.Govender, and A. Mainza, "Characterising porosity of multi-component mixtures in rotary mills", Minerals Engineering **24**, 276–281 (2011) (cit. on p. 19).

[113] E. Alizadeh, O. Dubé, F. Bertrand, and J. Chaouki, "Characterization of Mixing and Size Segregation in a Rotating Drum by a Particle Tracking Method", AIChE Journal **59**, 1894–1905 (2013) (cit. on p. 19).

[114] Y. Ding, R. Forster, J. Seville, and D. Parker, "Segregation of granular flow in the transverse plane of a rolling mode rotating drum", International Journal of Multiphase Flow **28**, 635–663 (2002) (cit. on p. 19).

[115] D. Kallon, I. Govender, and A. Mainza, “Circulation rate modelling of mill charge using position emission particle tracking”, Minerals Engineering **24**, 282–289 (2011) (cit. on p. 19).

[116] G. Tupper, I. Govender, and A. Mainza, “Predicting flows from the Dynamic Ergun Equation”, Minerals Engineering **103-104**, 11–13 (2017) (cit. on p. 19).

[117] G. B. Tupper, I. Govender, D. N. De Klerk, M. C. Richter, and A. N. Mainza, “Testing of a new dynamic Ergun equation for transport with positron emission particle tracking”, AIChE Journal **62**, 939–946 (2016) (cit. on p. 19).

[118] G. Tupper, I. Govender, A. Mainza, and N. Plint, “A mechanistic model for slurry transport in tumbling mills”, Minerals Engineering **43-44**, 102–104 (2013) (cit. on p. 19).

[119] I. Govender, G. Tupper, and A. Mainza, “Towards a mechanistic model for slurry transport in tumbling mills”, Minerals Engineering **24**, 230–235 (2011) (cit. on p. 19).

[120] F. Radjai and V. Richefeu, “Contact dynamics as a nonsmooth discrete element method”, Mechanics of Materials **41**, 715–728 (2009) (cit. on p. 20).

[121] S Hedman, “Smooth and non-smooth approaches to simulation of granular matter”, Masters Thesis (Umeå University, 2011) (cit. on p. 20).

[122] G. R. Liu and M. B. Liu, “Smoothed Particle Hydrodynamics: A Meshfree Particle Method” (World Scientific Publishing Company, 2003) (cit. on p. 21).

[123] A. V. Potapov, M. L. Hunt, and C. S. Campbell, “Liquid–solid flows using smoothed particle hydrodynamics and the discrete element method”, Powder Technology **116**, 204–213 (2001) (cit. on p. 21).

[124] P. W. Cleary, M. Sinnott, and R. Morrison, “Prediction of slurry transport in SAG mills using SPH fluid flow in a dynamic DEM based porous media”, Minerals Engineering **19**, 1517–1527 (2006) (cit. on p. 21).

[125] I. Govender, P. Cleary, and A. Mainza, “Comparisons of PEPT derived charge features in wet milling environments with a friction-adjusted DEM model”, Chemical Engineering Science **97**, 162–175 (2013) (cit. on p. 21).

[126] A. Di Renzo and F. P. Di Maio, “Comparison of contact-force models for the simulation of collisions in DEM-based granular flow codes”, Chemical Engineering Science **59**, 525–541 (2004) (cit. on p. 24).

[127] A. Di Renzo and F. P. Di Maio, “An improved integral non-linear model for the contact of particles in distinct element simulations”, Chemical Engineering Science **60**, 1303–1312 (2005) (cit. on p. 24).

[128] M. Lätzel, S. Luding, and H. J. Herrmann, “Macroscopic material properties from quasi-static, microscopic simulations of a two-dimensional shear-cell”, Granular Matter **2**, 123–135 (2000) (cit. on p. 41).

[129] N.-S. Cheng, “Formula for the Viscosity of a Glycerol-Water Mixture”, Industrial & Engineering Chemistry Research **47**, 3285–3288 (2008) (cit. on pp. 51, 52, 60–62, 93).

[130] J Bridgwater, S Forrest, and D. J. Parker, “PEPT for Agglomeration?”, Powder Technology **140**, 187–193 (2004) (cit. on p. 53).

[131] X. Fan, D. Parker, and M. Smith, “Labelling a Single Particle for Positron Emission Particle Tracking Using Direct Activation and Ion-Exchange Techniques”, Nuclear Instruments and Methods in Physics Research A **562**, 345–350 (2006) (cit. on p. 53).

[132] R. Chartrand, “Numerical Differentiation of Noisy, Nonsmooth Data”, ISRN Applied Mathematics **2011**, 1–11 (2011) (cit. on p. 56).

[133] J. Chaouki, F. Larachi, and M. P. Duduković, “Noninvasive Tomographic and Velocimetric Monitoring of Multiphase Flows”, Ind. Eng. Chem. Res. **36**, 4476–4503 (1997) (cit. on p. 63).

[134] C. Manzo and M. F. Garcia-Parajo, “A review of progress in single particle tracking: from methods to biophysical insights”, Reports on Progress in Physics **78**, 124601 (2015) (cit. on p. 63).

[135] R. D. Badawi, “Aspects of Optimisation and Quantification in Three-Dimensional Positron Emission Tomography”, Doctoral Dissertation (King’s College London (University of London), 1998) (cit. on p. 64).

[136] R. D. Evans, “The Atomic Nucleus” (McGraw-Hill Book Company Inc., New York, 1955) (cit. on p. 64).